Topology optimization of radio frequency and microwave structures

Aage, Niels

Publication date:
2011

Document Version
Publisher's PDF, also known as Version of record

Topology optimization of radio frequency and microwave structures

PhD Thesis

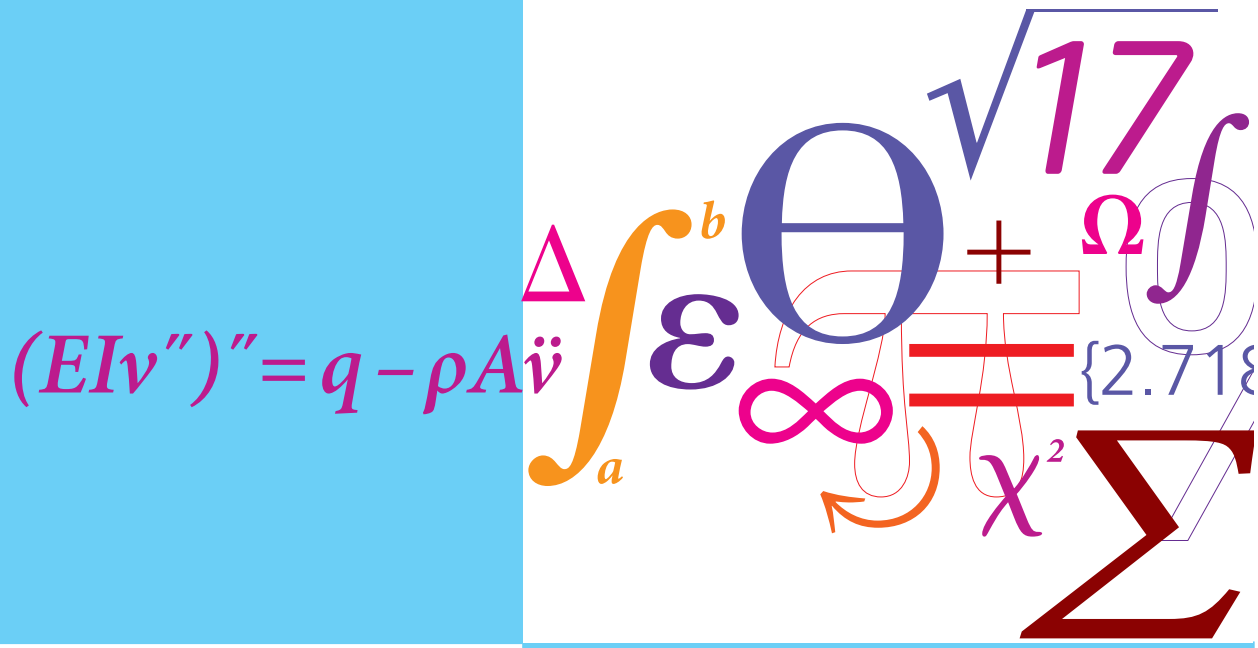

Niels Aage
DCAMM Special Report No. S129
April 2011

DTU Mechanical Engineering
Department of Mechanical Engineering

Topology optimization of radio frequency and microwave structures

by

Niels Aage

DEPT. OF MECHANICAL ENGINEERING
Solid Mechanics

TECHNICAL UNIVERSITY OF DENMARK

Title of the thesis:
Topology optimization of radio frequency and microwave structures

Ph.D. student:
Niels Aage
E-mail: naa@mek.dtu.dk

Supervisors:
Ole Sigmund
E-mail: sigmund@mek.dtu.dk

Niels Asger Mortensen
E-mail: namo@fotonik.dtu.dk

Olav Breinbjerg
E-mail: ob@elektro.dtu.dk

Address:
Department of Mechanical Engineering, Solid Mechanics
Technical University of Denmark
Nils Koppels Allé, Building 404, 2800 Kgs. Lyngby, Denmark

Preface

This thesis is submitted in partial fulfillment of the requirements for obtaining the degree of Ph.D. in mechanical engineering at the Technical University of Denmark (DTU). The Ph.D. project was funded by DTU and carried out at the Department of Mechanical Engineering, Solid Mechanics and the Department of Photonics Engineering, at DTU in the period January 1st 2008 - April 8th 2011. Supervisors on the project were Professor Dr.techn. Ole Sigmund (DTU Mechanical Engineering), Associate Professor Dr.techn. Niels Asger Mortensen (DTU Fotonik) and Professor Ph.D. Olav Breinbjerg (DTU Electrical Engineering).

I am very grateful to my three supervisors for their inspiring support, and for always taking their time to discuss the work and the results during the project.

I would also like to express my gratitude to the partners from the joint research group *Wireless coupling in small autonomous devices* funded by the Danish National Advanced Technology Foundation (HTF grant #004-2007-1), for the successful collaboration and for the help to understand the experimental and commercial aspects related to my theoretical work. The support from the Danish Center for Scientific Computing is also gratefully acknowledged.

Part of this work was carried out during a 4 month visit to Associate Professor Kurt Maute and his research group at the Department of Aerospace Engineering Sciences, University of Colorado at Boulder, USA, in the spring of 2010. I am grateful to Associate Professor Kurt Maute for making the stay possible and to his research group for creating a friendly and welcoming atmosphere.

In particular, I thank Boyan S. Lazarov at the Department of Mechanical Engineering, Solid Mechanics, DTU, for his collaboration on the implementation of the large scale C++ optimization framework developed as part of this project, as well as his many invaluable inputs regarding the project in general.

Finally, I would like to thank my colleagues in the TopOpt Group and in particular the other Ph.D.-students for creating a cheerful and inspiring working environment.

Thanks to my family and friends for their support. Special thanks to my wife Vigdis Mjanger and my daughter Frida Aage for their love, support and encouragement during this work.

Kgs. Lyngby, April 8th 2011.

Niels Aage

Resumé (in Danish)

Denne afhandling beskriver en topologioptimeringsmetode, som er udviklet til at designe og optimere elektromagnetiske konstruktioner. Fokus er lagt på metalliske strukturer, der opererer indenfor radio- og mikrobølgeområdet. Forskningen er motiveret af, at der er et stadigt stigende brug af små håndholdte, og autonome, elektriske apparater, hvilket har ført til en række nye udfordringer for udformningen af f.eks. elektrisk-små antenner og dertil hørende strømforsyninger.

En del af projektets formål har været at implementere den udviklede topologioptimeringsmetode dels i Matlab og dels en paralleliseret C++ kode, der effektivt kan løse både 2D og 3D designproblemer.

Først anvendes optimeringsproceduren til at designe anordninger til energifokusering. De første eksempler viser optimering af 2D og 3D resonatorer, der kan opfattes som forenklede systemer til energihøstning. Efterfølgende præsenteres et mere praktisk anvendeligt designproblem, hvor Fresnel plade-zone-linser optimeres. Det bliver vist, at energifokuseringseffekten kan øges med mere end 30 % i forhold til konventionelle designs.

Det efterfølgende optimeringsproblem vedrører udformningen af elektrisk små antenner. En to-trins optimeringsprocedure introduceres, således at afhængigheden af gode start gæt kan elimineres. Resultatet er en metode, der kan benyttes til systematisk design af antenneanordninger. Metodens fremgangsmåde demonstreres ved et eksempel, hvori en halvkugleformet elektrisk lille antenne bliver optimeret. Det vises, at den optimerede antenne udstråler mere end 99 % af indgangseffekten.

Det tredje og sidste designproblem vedrører optimering af anordninger til trådløs energioverførsel, hvor princippet bygger på koblingen mellem magnetiske resonatorer gennem deres nærfelt. Et enkelt optimeringsproblem præsenteres og benyttes til at verificere formuleringens gyldighed. Den optimerede struktur illustrerer optimeringsmetodens muligheder, men afslører også den nuværende implementerings numeriske begrænsninger.

Abstract

This thesis focuses on topology optimization of conductor-based microwave and radio frequency electromagnetic devices. The research is motivated by the ever increasing usage of small hand-held, or autonomous, electric devices, which have lead to a series of new challenges for the design of efficient antennas and power supplies.

A topology optimization methodology is proposed based on a design parameterization which incorporates the skin effect. The numerical optimization procedure is implemented in Matlab, for 2D problems, and in a parallel C++ optimization framework, for 3D design problems.

The optimization procedure is first applied to the design of energy focusing devices. The examples cover 2D and 3D resonators, which can be thought of as simplified energy harvesting systems. This is followed by a more practical example, in which the design and optimization of Fresnel plate zone lenses are investigated. It is shown that the performance can be increased with more than 30 % compared to a conventional design.

The second optimization problem investigated concerns the design of sub-wavelength antennas. In order to alleviate dependence on the initial design and to obtain a generally applicable design formalism, a two step optimization procedure is presented. This scheme is applied to the design and optimization of a hemispherical sub-wavelength antenna. The optimized antenna configuration displayed a ratio of radiated power to input power in excess of 99 %.

The third, and last, design problem considered in this thesis, concerns the optimization of devices for wireless energy transfer via strongly coupled magnetic resonators. A single design problem is considered to demonstrate proof of concept. The resulting design illustrates the possibilities of the optimization method, but also reveals its numerical limitations with respect to the resolution of the different length-scales involved.

Publications

The following publications are part of the thesis

[P1] N. Aage, N.A. Mortensen, and O. Sigmund, "Topology optimization of metallic devices for microwave applications", *Int. J. Num. Meth. Eng.*, vol. 83, no. 2, pp.228-248, Mar. 2010.

[P2] N. Aage and B.S. Lazarov, "Parallel multiphyscics topology optimization using the method of moving asymptotes", Submitted April 2011.

[P3] N. Aage and O. Sigmund, "Topology optimization of radio frequency and microwave antennas by free distribution of conducting material". To be submitted.

[P4] N. Aage, N.A. Mortensen, and O. Sigmund, "Topology optimization of devices for wireless energy transfer: The design parametrization". proceedings of WCSMO-8, 8th World Congress on Structural and Multidisciplinary Optimization, LNEC, Lisbon, Portugal, June 1-5, 2009.

Contents

Chapter 1
Introduction

1.1 Motivation and goal for this thesis

The use of small hand-held, or autonomous, electrical devices has increased dramatically during the past two decades. Common for such devices is the need for wireless communication, and as the devices become ever smaller and packed with more and more functionality, the traditional antenna system designs are in many cases inadequate and therefore the development of new conformal antenna designs are needed (Mittra, 2007). Examples of such devices include hearing aids, medical implants, cellular phones, sensing devices, etc. The list is seemingly endless and is continuously extended. Another aspect of the increasing complexity of small electrical devices is the growth in power consumption. This has lead to the reinvention of old theories on wireless energy transfer using magnetically resonant-coupled copper coils (Kurs et al., 2007). Comparing the design tasks of antenna systems and devices for wireless energy transfer reveal that they consist of the same main task. Namely the distribution of a conducting material, e.g. a metal such as copper, within the design space available for a given device.

The aim of this thesis is to apply gradient based topology optimization to systematically design electrically small devices by distributing conducting material. Topology optimization, also known as the material distribution method, is a numerical optimization technique tailored for optimization problems in which the material layout is unknown. The method has already demonstrated its efficiency on a variety of academic and industrial design problems, especially within the field of solid mechanics. The main goal of this thesis is to develop an efficient and robust extension to the topology optimization method for microwave and radio frequency design problems. This includes the development of efficient numerical tools for the solution of the partial differential equations governing the physics of electromagnetic wave propagation.

1.2 Structure of thesis

This thesis is a summary of the work done during the Ph.D. study. It provides an overview of the publications in [P1]-[P4] complemented by a few additional design problems and the results of these investigations.

Chapter 2 introduces the electromagnetic wave problem and highlights the physical aspects of importance to this work. The finite element solution to the time-harmonic vector wave equation is discussed.

The topology optimization method is presented in chapter 3 with emphasis on wave propagation problems. In this thesis, the topology optimization method is extended to problems involving the design of volumetric conductor-based radio frequency and microwave structures. The main result of [P1] is stated in the form of a design parameterization that resolves numerical issues regarding the rapid decay of electromagnetic fields within a conductor, i.e. the skin effect.

The parallel C++ framework used to solve the three-dimensional optimization problems is introduced in chapter 4 along with performance results from [P2]. This includes parallel scalability and convergence characteristics of the optimization algorithm.

The optimization of energy focusing devices is described in chapter 5 and results from [P1,P3,P4] are presented. The chapter is concluded with the presentation of additional optimized designs based on Fresnel plate zone lenses.

In chapter 6 topology optimization of antennas is investigated. A two phase optimization method is proposed to alleviate issues arising from the lack of a proper starting guesses. Phase I consists of determining a useful initial design for phase II which consists of solving the actual antenna optimization problem. The method is demonstrated on a design problem from [P3].

The final design problem concerns the optimization of devices for wireless energy transfer. Proof of concept is demonstrated on a design problem for which experimental data is available. However, the optimization of devices for wireless energy transfer is complicated by the lengthscales involved, which leads to huge finite element models that cannot be handled by current solvers implemented in the parallel framework.

Finally, the findings are summarized into a common conclusion and ideas for future work are presented.

Chapter 2
Maxwell's equations on time-harmonic form

In this chapter electromagnetic waves are introduced along with the equations governing their propagation, i.e. Maxwell's equations. It is shown how Maxwell's equations can be cast on time-harmonic form and converted into a single second order partial differential equation (PDE) and how this equation can be solved by the finite element method (FEM).

2.1 Electromagnetic waves

Electromagnetic waves are behind many types of cutting-edge and everyday technologies covering applications such as radio transmission, X-ray machines and optical circuits. In this work the electromagnetic spectrum of interest is that of the radio frequency (RF) and microwave region, which is here defined to cover the spectrum from 3MHz to 300GHz. As other types of wave phenomena, electromagnetic waves consist of disturbances in both space and time. Electromagnetic waves differ from other types of wave phenomena, since they are capable of propagating in both media as well as vacuum (Balanis, 2005). The theory on electromagnetic waves was first described by J.C. Maxwell in the mid 19th century (Maxwell, 1865), where he combined the laws of Faraday, Ampére and Gauss into a single set of coupled equations, now known as Maxwell's equations. Electromagnetic waves are caused by the interaction of a time varying electric field and a time varying magnetic field. The magnetic and electric fields of an electromagnetic wave oscillates perpendicular to each other and to the direction of energy propagation (Balanis, 1989). Maxwell's equations fully describe the propagation of general elliptic polarized electromagnetic waves.

Electromagnetic waves have been studied thoroughly the past 150 years and have lead to a true technological revolution in both science and everyday life. To name just a few applications that fall into the electromagnetic spectrum of interest, one could think of radar, radio and television transmission, cellular phones, GPS antennas, sensing devices and microwave ovens.

2.2 Maxwell's equations

In this section Maxwell's equations for a linear, isotropic material with no free charges are presented on differential form. Letting $\boldsymbol{x}$ be the spatial coordinates, t the time and applying the aforementioned assumptions, Maxwell's equations can be

stated as

$$\nabla \times \boldsymbol{E} = -\mu \frac{\partial \boldsymbol{H}}{\partial t} \qquad \text{Faraday's law} \tag{2.1}$$

$$\nabla \times \boldsymbol{H} = \sigma \boldsymbol{E} + \epsilon \frac{\partial \boldsymbol{E}}{\partial t} \qquad \text{Ampére's law} \tag{2.2}$$

$$\nabla \cdot \epsilon \boldsymbol{E} = 0 \qquad \text{Gauss' law} \tag{2.3}$$

$$\nabla \cdot \mu \boldsymbol{H} = 0 \qquad \text{Gauss' law} \tag{2.4}$$

where $\boldsymbol{E} = \boldsymbol{E}(\boldsymbol{x}, t)$ and $\boldsymbol{H} = \boldsymbol{H}(\boldsymbol{x}, t)$ denotes the electric and magnetic fields respectively. The material parameter $\epsilon = \epsilon(\boldsymbol{x})$, termed the electric permittivity, is a measure for a mediums ability to permit an electric field. The magnetic permeability $\mu = \mu(\boldsymbol{x})$ is a measure for a materials ability to support a magnetic field. The conductivity $\sigma = \sigma(\boldsymbol{x})$ describes, in a mathematical sense, the amount of loss experienced by the electric field within a medium, e.g. similar to a damping parameter in elasticity (Thomsen, 2003). In electromagnetic theory it is usually interpreted as a measure for how well a material can conduct an electric current (Balanis, 1989). For a perfect electric conductor (PEC) we have that $\sigma = \infty$, which means that an electromagnetic field cannot penetrate into the PEC, i.e. the current will only flow on the boundary between the dielectric and the conductor. For a good conductor σ is finite, but numerically large i.e. $\sigma = 5.998 \times 10^7$ S/m for copper, and the electric field will rapidly decay within the material. This is known as the skin effect and is characterized by a measure termed the skin depth. The skin depth, δ, is a measure for the distance a traveling plane wave penetrates into a conductor before the amplitude is decreased by a factor of e^{-1} (Balanis, 2005). The skin depth can be computed by the approximate formula

$$\delta = \frac{1}{\sqrt{\pi \sigma \mu f}} \tag{2.5}$$

where f is the frequency of the electromagnetic wave. For microwave and RF applications the skin depth is in the order of micrometers, while the actual structures have dimensions of mm or cm when considering only electrically small structures. Electrically small here refers to those structures where the largest dimension, D, is usually less than $\lambda/10$ where λ is the wavelength (Balanis, 2005). This means that the skin depth is at least three orders of magnitude smaller than the devices. The skin effect must be treated with care when using numerical methods to model the performance of such devices, and will be addressed again in the sections concerning the material interpolation scheme used for the optimization of microwave and RF structures.

2.2.1 The vector wave equation

Maxwell's equations can be solved for either the electric or magnetic field, or for both fields simultaneously. Throughout this work Maxwell's equations are solved

for either the electric or the magnetic field. To accomplish this, the two first order equations given by Faraday's and Ampére's laws are recast into a single second order PDE. For the remainder of this chapter the description is restricted to deal with the electric field formulation, but similar manipulations could just as easily have been applied for the magnetic field. To obtain a single second order PDE for the electric field, equation (2.1) is inserted into (2.2) which readily yields

$$\nabla \times \left(\mu^{-1}\nabla \times \boldsymbol{E}\right) + \sigma\frac{\partial \boldsymbol{E}}{\partial t} + \epsilon\frac{\partial^2 \boldsymbol{E}}{\partial t^2} = 0 \tag{2.6}$$

Equation (2.6) is known as the vector wave equation (Jin, 2002). The equation can be solved by applying appropriate boundary and initial conditions, and should generally be solved in conjunction with Gauss's law for the electric field, i.e. equation (2.3).

2.2.2 Time harmonic wave equation

In many cases of practical interest it is valid to assume that the electromagnetic waves varies harmonically in time with angular frequency ω (Balanis, 2005). This means that the time dependence in Maxwell's equations can be factored out by transforming the equations into the frequency domain. To obtain the time-harmonic form of Maxwell's equations the dependent fields are represented by $\boldsymbol{u}(\boldsymbol{x}, t) = \mathbb{R}\left[\boldsymbol{u}(\boldsymbol{x})e^{j\omega t}\right]$ where j is the imaginary unit, $\mathbb{R}$ the real part and $\boldsymbol{u}(\boldsymbol{x})$ is the complex amplitude. The sign in complex exponential follows the standard engineering convention (Jin and Riley, 2009). Inserting the complex field representation into Maxwell's equations corresponds to substituting the first order time derivatives with $j\omega$ and the second order derivatives with $-\omega$. For the electric field the time harmonic vector wave equation yields

$$\nabla \times \left(\mu_r^{-1}\nabla \times \boldsymbol{E}\right) - k_0^2\epsilon_c\boldsymbol{E} = 0 \tag{2.7}$$

where μ_r is the relative permeability, ϵ_c the relative complex permittivity and $k_0 = \omega\sqrt{\epsilon_0\mu_0}$ is the free space wave number (Balanis, 1989). The two remaining constants are the free space permittivity, $\epsilon_0 \approx 8.8542 \cdot 10^{-12}$ F/m, and free space permeability, $\mu_0 = 4\pi 10^{-7}$ H/m, respectively. The complex permittivity is given by

$$\epsilon_c = \epsilon_r - j\frac{\sigma}{\omega\epsilon_0} \tag{2.8}$$

where ϵ_r is the relative permittivity, also known as the dielectric constant. It is this type of second order PDE which, along with appropriate boundary conditions, constitutes the backbone of the numerical modeling done as part of this thesis.

2.3 Modeling of electromagnetic waves

Modeling of electromagnetic wave problems consists of solving the boundary value problem associated with Maxwell's equations and the boundary conditions specific

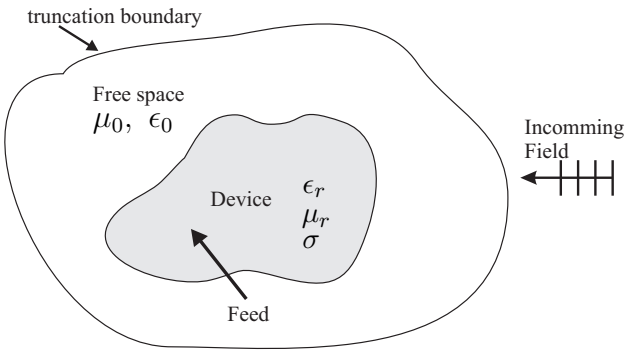

Figure 2.1 General model of an electromagnetic wave propagation problem.

for the given model problem. Since the electromagnetic field can propagate in all media, including vacuum, there is no natural way of terminating the computational domain. Instead the domain is truncated using an approximation to the Sommerfeld condition. The Sommerfeld condition states that an electromagnetic field will not be reflected from infinity when propagating in free space (Balanis, 1989). Several techniques are capable of approximating the Sommerfeld condition, for example absorbing boundary conditions, perfectly matched layers or boundary integral methods (Jin, 2002). They all have their advantages and disadvantages which is discussed in detail in Jin and Riley (2009). The excitation of an electromagnetic device can be performed using e.g. incident waves, voltage gap generators or waveguide feeds such as coaxial cables. A general model sketch for the problems investigated in this thesis can be seen in figure 2.1. Throughout the presented work the computational domain is truncated using a first order absorbing boundary condition (ABC) (Jin and Riley, 2009). This boundary condition can easily be modified to include an incident field such as e.g a plane wave or the modes of a coaxial cable. The boundary condition can be formulated as

$$\boldsymbol{n} \times (\nabla \times \boldsymbol{E}) + jk_0 \boldsymbol{n} \times (\boldsymbol{n} \times \boldsymbol{E}) = -\boldsymbol{n} \times [\boldsymbol{E}_0(\boldsymbol{x}) \times jk_0(\boldsymbol{n} - \boldsymbol{k})]\, e^{-jk_0 \boldsymbol{k}\cdot\boldsymbol{x}} \tag{2.9}$$

where $\boldsymbol{n}$ is an outward normal vector, $\boldsymbol{E}_0(\boldsymbol{x})$ is the profile of the incident wave and $\boldsymbol{k}$ the direction of propagation. In order for this boundary condition to be a proper representation of the Sommerfeld condition, it is required that the scattered field is normal incident on the boundary. This can in most cases be achieved by placing the truncation boundary sufficiently far away from the scatterer. Usually a distance of one wavelength between the scatterer and a spherical truncation boundary will suffice (Jin and Riley, 2009).

Solving Maxwell's equations in the general case where material coefficients are free to vary in space is not possible with analytic methods and therefore numerical methods are often applied (Jin, 2002). In this work the finite element method is used.

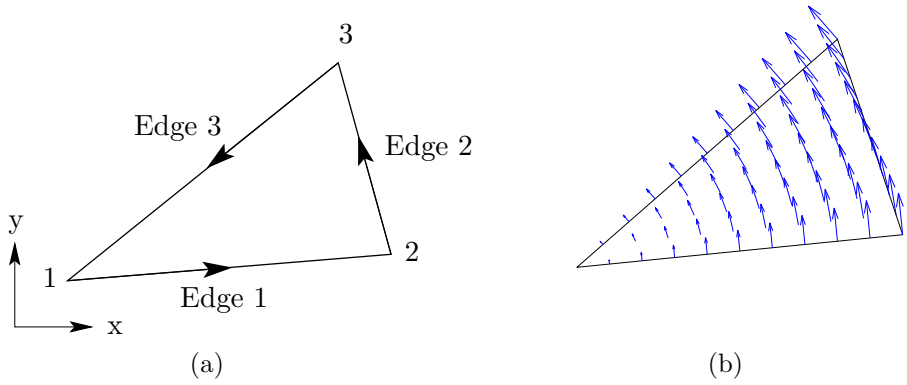

Figure 2.2 Illustration of the dofs for a triangular edge element (a). In (b) the shape-function corresponding to edge 2, i.e $\boldsymbol{N}_2$, is plotted. From this plot it is clear that $\boldsymbol{N}_2$ only has a tangential component at edge 2, while it is zero for edge 1 and 3.

2.3.1 Finite element form of Maxwell's equations

For the general case of three dimensional wave problems, the finite element solution to the vector wave equation suffers from a few, but severe, shortcomings when using standard nodal basis functions. This is due to the following three reasons. First, the electromagnetic fields are, by nature, normal discontinuous and tangential continuous across material interfaces. Secondly, nodal basis functions do not naturally incorporate the enforcement of the divergence condition, i.e. Gauss's law. And third, and probably most problematic, using nodal elements results in singularities at material edges and corners (Zhu and Cangellaris, 2006). Though cures are available for the first two issues, the third problem lacks a general cure (Jin, 2002). Therefore the finite element solution of Maxwell's equations is most naturally performed using vector basis functions. This results in vector finite elements, also known as edge-elements, which are characterized by having their local degrees of freedom (dof) associated with element edges instead of nodes. Edge elements for electromagnetic problems are first suggested in Nedelec (1980). The vector based interpolation can be expressed as

$$\boldsymbol{E}^e = \sum_i^M \boldsymbol{N}_i(\boldsymbol{x}) E_i \tag{2.10}$$

where M is the number of edges and $\boldsymbol{N}_i(\boldsymbol{x})$ are the vector basis functions (Zhu and Cangellaris, 2006). A first order triangular edge element is visualized in figure 2.2. From a practical point of view edge elements differ mainly in the way the dof are numbered for a given mesh, and in the fact that the expansion variables E_i have a direction. The mathematical form of edge elements corresponds to the natural space associated with the curl-operator, i.e. the Sobolev space $V := H(\nabla \times \boldsymbol{v}, \Omega) = \{\boldsymbol{v} \in [L_2(\Omega)]^3 | \nabla \times \boldsymbol{v} \in [L_2(\Omega)]^3\}$ where Ω is a bounded domain (Zaglmayr, 2006). It

is obvious from the construction of edge elements that they only enforce tangential continuity over material interfaces. It can also be shown that edge elements based on triangular, tetrahedral or brick elements fulfils the divergence condition, i.e. Gauss's law.

The weak form of the PDE in equation (2.7) is to find $\boldsymbol{T} \in V$

$$\int_{\Omega} \left[(\nabla \times \boldsymbol{T}) \cdot \mu_r^{-1} \cdot (\nabla \times \boldsymbol{E}) - k_0^2 \boldsymbol{T} \cdot \epsilon_c \cdot \boldsymbol{E} \right] \mathrm{d}\Omega - \int_{\Gamma} \boldsymbol{T} \cdot \left[\boldsymbol{n} \times \left(\mu_r^{-1} \cdot \nabla \times \boldsymbol{E} \right) \right] \mathrm{d}\Gamma = 0 \qquad \forall \boldsymbol{E} \in V \tag{2.11}$$

where $\boldsymbol{T}$ is a vector test function and Γ is the boundary on which Neumann conditions are prescribed. The weak form can be discretized using the standard Galerkin method (Zienkiewicz and Taylor, 2000), i.e. to use the same functions for testing and basis, which leads to a linear system of the form

$$\boldsymbol{S}\tilde{\boldsymbol{E}} = \boldsymbol{b} \tag{2.12}$$

where the actual structure of the system matrix $\boldsymbol{S}$ and load vector $\boldsymbol{b}$ depends on the boundary conditions for the problem in question. The vector $\tilde{\boldsymbol{E}}$ contains expansion coefficients, i.e. the discrete solution. Even without the explicit structure of the linear system having been stated, it is still possible to characterize it with respect to mesh quality and possible solution methods. For wave propagation problems it is imperative that the wavelength is resolved. Using first order edge, or nodal, elements a rule of thumb is to include approximately 20 elements per wavelength. The solution to the linear system in equation (2.12) should take into account that the system matrix is symmetric indefinite. The indefinite characteristic of the resulting linear system limits the choice of linear solvers. That is, it is not possible to use a Cholesky factorization for direct solution or the very attractive Krylov method of conjugate gradients. Instead, a LU factorization can be applied for direct solution or one of many generalized residual methods for the iterative solution (Saad, 2000).

Finally it should be noted that most electromagnetic problems are inherently three dimensional. This means that black box solvers, such as e.g. Comsol Multiphysics by COMSOL AB, are currently not capable of providing the solution to large systems within an acceptable time. The fast solution to the wave problem is imperative since optimization requires hundreds of evaluations. As a final remark it is noted that in the case of 2D problems, the vector wave equation can be reduced to the scalar Helmholtz equation, which can be solved by nodal finite elements and with the use of high-level tools such as Matlab.

Chapter 3
Topology optimization of microwave and RF structures

Topology optimization is a numerical optimization method used to determine an optimized material distribution. The material distribution is optimized with respect to a given objective function and a set of constraints for the physical system. In its standard form, the method consists of representing a predescribed design domain by a number of pixels or voxels, where each discrete element is given a density, or design variable, that can vary between zero and one. The method was originally developed for solid mechanics in which an element with density one is considered to be a solid while a zero density corresponds to void. Using this representation for the design space, the optimization process is not restricted to a predefined set of boundaries, which mean that the topology can change during the optimization process. This feature, besides giving rise to the methods name, also means that the method has a greater freedom compared to other techniques such as size and shape optimization.

The method was developed in the late 1980's by Bendsøe and Kikuchi (1988) based on the homogenization method, while the density interpretation was introduced in Bendsøe (1989). The theory on topology optimization is by now well-established and can be found thoroughly explained in Bendsøe and Sigmund (2004). By the end of the 1990's the method had reached a level of maturity which has changed the way the automotive and aerospace industry conduct their design processes (Thomas et al., 2002). Today several dedicated commercial topology optimization packages such as OptiStruct by Altair and TOSCA by FE-Design are available.

During the last decade the method has been applied to several other branches of physics such as fluid mechanics, heat transfer, elastic wave problems, optics and coupled multiphysic problems. Though the method has shown great success within many of these research areas (Bendsøe and Sigmund, 2004), the development of the method continuous.

3.1 Topology optimization for wave problems

Since the beginning of the new millennium topology optimization has been applied to a series of wave propagation problems covering various physical settings.

The method has been applied to elastic wave propagation problems, namely the design of phononic band-gap structures and materials (Sigmund and Jensen, 2003) as well as periodic plate structures (Halkjær et al., 2006). In Larsen et al. (2009)

topology optimization is applied to minimize the vibrational response of a plate, and to maximize the guided transport of energy. Design problems for elastic rods in which the design can vary in time are presented in Jensen (2009), i.e. both temporal and spatial material distributions are considered.

Within the field of optics the topology optimization method has been shown to yield excellent results. The method has been applied to the design of photonic crystals with maximized band-gaps (Cox and Dobson, 1999) and to the design of waveguide bends and splitters with optimized transmission properties (Jensen and Sigmund, 2004; Borel et al., 2005; Jensen and Sigmund, 2005). In Sigmund and Hougaard (2008) topology optimization was used as a basis for deriving a simple geometric relation capable of predicting the size and location of the band-gaps for general planar photonic crystals. The method has also been applied to the design of other optical circuit elements such as waveguide coupling to microcavities (Matzen et al., 2010), plasmonic grating couplers (Andkjær et al., 2010) and for the robust design, i.e. design including manufacturability uncertainties, of photonic waveguides (Wang et al., 2011). A review of topology optimization in photonics can be found in Jensen and Sigmund (2011).

Acoustic wave problems have also been subject to the topology optimization method. Applications cover problems such as the design of acoustic horns with optimized radiation efficiency (Wadbro and Berggren, 2006), the design of acoustic noise barriers (Dühring et al., 2008) and optimization of acoustic-structure interaction problems (Yoon et al., 2007; Niu et al., 2010).

3.1.1 Optimization of RF and microwave devices

As great as the number of publications is on topology optimization and wave problems in mechanics, optics and acoustics, just as sparse it is for topology optimization of RF and microwave devices. This is especially evident for the distribution of conducting materials (metal), but is also the case for optimization problems considering the distribution of dielectric and magnetic material. However, the research on optimal electromagnetic structures dates back to Maxwell (1873), and since then much effort has been put into optimizing different electromagnetic design problems. Besides the optimization done using analytical methods, which is obviously restricted to problems of simple geometries, most of the effort has been put into evolutionary, or genetic, algorithms. The results based on evolutionary and genetic algorithms can be found summarized in the review papers (Weile and Michielssen, 1997) and (Hoorfar, 2007).

General for most of the research conducted on genetic algorithms and metallic RF and microwave structures, is that they all start from an already good design which they then attempt to improve. In Li et al. (2002) the authors optimize the performance of folded slot antennas while minimizing the reflection in the feed. The genetic approach has also been applied to the optimization of RFID tags and readers (Galehdar et al., 2009). In Lim and Ling (2007) electrically small wire antennas are

optimized based on an initial configuration of an Yagi antenna (Balanis, 2005). Common for all examples is that the design variables are chosen as e.g. height, length and spacing between conducting elements.

Though most of the genetic optimization results found in the literature concern small modifications to an already working antenna design, some effort has been put into topology design by evolutionary methods. Examples of such cover e.g. Altshuler (2002) where a genetic algorithm is used for the design of electrically small wire antennas. The design of planar patch antennas is investigated in Koulouridis et al. (2007) where the authors simultaneously distribute dielectric and conductor to achieve a larger bandwidth. Another evolutionary method that has been used to perform topology optimization is the particle swarm method (Robinson and Rahmat-Samii, 2004). Again the optimization of Yagi type antennas is examined (Bayraktar et al., 2006) as well as the design of GSM antennas for cellular phones (Zaharis, 2008). In Assadihaghi et al. (2008) the authors use a genetic algorithm based on gradient evaluations for the optimization of patch antennas. However, the gradients are merely used as part of a modified genetic algorithm and the design problem remains discrete. This approach is similar to the evolutionary structural optimization method (Xie and Steven, 1993), but is extended to also incorporate the concept of parents and descendants often used in genetic algorithms.

It should be mentioned that pure gradient based methods have been applied in cases of parameter optimization. An example is the determination of the optimal distance between conducting elements in patch antennas (Li et al., 1997).

The main argument for the application of evolutionary methods is that the methods produce better results than the initial setting. Generally, improvements in performance between 5% to 30% are observed (Hoorfar, 2007). However, the application of genetic optimization methods to general problems are limited due to a lack of efficient large scale solvers for the Maxwell problem with spatially varying parameters (Zaglmayr, 2006). That is, the solution of a single state problem can be extremely time-consuming and thus not allowing for thousands of state evaluations. Note that the most popular numerical methods in electromagnetics are the finite difference time domain (FDTD) method and the method of moments (Jin and Riley, 2009). These methods have been used in a pretty much un-altered form for the past 30 to 50 years (Balanis, 1989). However, during the last two decades the FEM is being applied more frequently (Jin, 2002), especially since the introduction of the commercial FEM software package HFSS by Ansoft. Leaving the realm of evolutionary and genetic methods, it is summarized that the most important arguments against using such methods is that they require a high number of state evaluations, and that they are restricted to problems with a small number of design parameters (Sigmund, 2011). As a consequence such methods are surely not applicable to the material distribution problems that can be solved using gradient based topology optimization.

As already mentioned the work on topology optimization for microwave and RF devices is quite sparse, though some work have been presented and published

within the last decade. Research concerning the distribution of dielectric material is addressed in (Kiziltas et al., 2003, 2004), in which topology optimization is used to enhance the performance of antennas by increasing the bandwidth. The design of purely dielectric resonant antennas is investigated in Nomura et al. (2007). In the Ph.D. thesis by Kiziltas (2003), a first approach for optimization of conductor-based microwave structures was demonstrated based on a modified version of the well known solid isotropic material with penalization (SIMP) interpolation scheme (Bendsøe, 1989). This approach was also pursued in Erentok and Sigmund (2011) for the design of electrically small antennas. The method was shown to work for shell problems, but since the FE discretization does not fulfil the energy balance, the optimized designs require much postprocessing to obtain a functional antenna. This is a consequence of not resolving the skin depth. In Diaz and Sigmund (2010) the topology optimization method is used to design conductor-based metamaterials with negative permeability. For this optimization problem the dimensions of the design domain are naturally chosen such that the skin depth is resolved. A similar design problem was solved by a level-set method in Zhou et al. (2010b) and in Zhou et al. (2010a) the same level-set method was applied to the design of planar dipole antennas. A general cure for the skin depth problem was proposed in [P1], which will be presented next.

3.2 Design parameterization [P1]

This section introduces the main ideas concerning the design parameterization presented in [P1].

Following the standard approach for gradient-based topology optimization each finite element within the design domain is associated with a continuous design variable $0 \leq \rho^e \leq 1$. The design variable is used to interpolate between two candidate materials denoted with $(\cdot)^m$ for the conductor and $(\cdot)^d$ for the dielectric.

Before proceeding further with the presentation of the design parameterization, the numerical issue regarding skin depth in conductor based topology optimization is exemplified. As an example let us consider a cubic design domain with side lengths of one cm. Each element can possibly be either dielectric, such as air, or copper which has a conductivity of $\sigma = 5.998 \times 10^7$ S. To resolved the skin depth at 300MHz, where $\delta \approx 3.75 \times 10^{-}6$ m, would require approximately 5000 first order elements in each spatial direction, i.e. a total of $1.25 \cdot 10^{11}$ elements. In the context of topology optimization where hundreds of state problem evaluations are needed, such high element numbers imply that brute force meshing is insufficient for general microwave or RF design problems with a priori unknown geometries.

The idea of the design parameterization presented in [P1] is to wrap each design element in an element impedance condition, which is illustrated in figure 3.1. In electromagnetic analysis the impedance boundary condition is used to model conductors with finite conductivity such that the skin effect is incorporated in the numerical model. This is obtained by removing the conducting material from the modeling

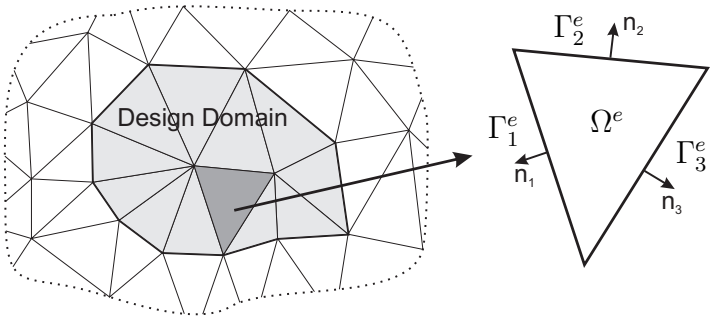

Figure 3.1 Model sketch of a discretized design domain (grey) and a surrounding free space domain (white). Within the design domain each element has the possibility of being either dielectric or conducting material. To remedy the skin depth issue each design element is wrapped in an impedance condition if the element is a conductor. This is illustrated by the highlighted element which shows the edges on which the impedance condition is imposed.

domain and replacing it with a boundary condition. The impedance condition can be cast on a form well-suited for finite elements, c.f. equation (2.11), and can be stated as

$$\boldsymbol{n} \times \left([\mu_r^d]^{-1} \nabla \times \boldsymbol{E}\right) + jk_0 \sqrt{\frac{\epsilon_c^m}{\mu_r^m}} \boldsymbol{n} \times (\boldsymbol{n} \times \boldsymbol{E}) = \boldsymbol{0}, \tag{3.1}$$

$$\boldsymbol{n} \times \left([\epsilon_r^d]^{-1} \nabla \times \boldsymbol{H}\right) + jk_0 \sqrt{\frac{\mu_r^m}{\epsilon_c^m}} \boldsymbol{n} \times (\boldsymbol{n} \times \boldsymbol{H}) = \boldsymbol{0} \tag{3.2}$$

It is especially appealing that the impedance condition have the same general form for both the electric and magnetic fields, which allows for a unified design parameterization. This is in contrast to using the PEC condition which leads to a Dirichlet condition for the electric field and a Neumann condition for the magnetic field. Since the inclusion of the impedance condition is done on element level it is not possible to state the design parameterization in a continuous setting. Thus, the design parameterization is discrete by construction. A field independent formulation of the finite element equation for a single design element can be stated as

$$\left(f_K \boldsymbol{K}^e - f_M \boldsymbol{M}^e - f_B \boldsymbol{B}^e\right) \boldsymbol{u}^e = 0 \tag{3.3}$$

where the $\boldsymbol{u}^e$ refers to either the electric or magnetic field, and the factors f_K, f_M and f_B depends on the design variables as well as the chosen field. The element matrices are computed as

$$\begin{aligned} \boldsymbol{K}^e &= \textstyle\int_{\Omega^e} (\nabla \times \boldsymbol{N}) \cdot (\nabla \times \boldsymbol{N}) \mathrm{d}\Omega \\ \boldsymbol{M}^e &= \textstyle\int_{\Omega^e} k_0^2 \boldsymbol{N} \cdot \boldsymbol{N} \mathrm{d}\Omega \\ \boldsymbol{B}^e &= jk_0 \textstyle\sum_i^N \int_{\Gamma_i^e} (\boldsymbol{n} \times \boldsymbol{N}) \cdot (\boldsymbol{n} \times \boldsymbol{N}) \mathrm{d}\Gamma \end{aligned} \tag{3.4}$$

$\boldsymbol{u}$	f_K	f_M	f_B
$\boldsymbol{E}$	$1/\mu_r^d$	$\epsilon_r^d - j\frac{\sigma(\rho^e)}{\omega\epsilon_0}$	$\rho_e^{13}\sqrt{\left(\epsilon_r^m - j\frac{\sigma^m}{\omega\epsilon_0}\right)/\mu^m}$
$\boldsymbol{H}$	$1/\left(\epsilon_r^d - j\frac{\sigma(\rho^e)}{\omega\epsilon_0}\right)$	μ_r^d	$\rho_e\sqrt{\mu^m/\left(\epsilon_r^m - j\frac{\sigma^m}{\omega\epsilon_0}\right)}$

Table 3.1 The factors used for the design parameterization in equation (3.3). The superscript $(\cdot)^m$ and $(\cdot)^d$ refer to material constants for the conducting and dielectric material respectively. The function $\sigma(\rho) = \sigma^d\left(\frac{\sigma^m}{\sigma^d}\right)^{\rho_e}$ is included because numerical experiments have shown that this leads to better performance of the optimization algorithm.

where Ω^e is the element volume and N is the number of element faces which are denoted with Γ_i^e. The field dependent factors are stated in table 3.1, which contains a simplified version that only includes conductivity design interpolation. For the general formulation the reader is referred to [P1]. The proposed design interpolation suffers from the same issue as some other design parameterizations in topology optimization. That is, the physical interpretation of intermediate densities is uncertain, though one might be able to link them to materials with varying conductivities. However, if the final design has $\rho = 0$ or $\rho = 1$ in all design elements, the physical performance of the optimized design has been analyzed with a correct physical model. This then means that one should ensure that the final design does not contain any intermediate densities. In many other topology optimization problems this is achieved by either a penalization scheme, c.f. SIMP (Bendsøe, 1989), or by the use of density filters in conjunction with a Heaviside projection (Guest et al., 2004; Sigmund, 2007). However, the optimization problems considered in this thesis can be classified as self-penalizing. This is due to the inherent damping nature of the conducting material. This means that regions of intermediate conductivities slowly damp, or absorb, the energy from the electromagnetic fields, whereas a high conductivity means fast spatial decay, which results in less energy dissipation. This makes it favorable for the optimizer to converge to binary solutions.

3.3 Optimization problem

The optimization problems considered in this thesis all have the same general structure and can be posed on a form standard for non-linear mathematical programmes (NLP) (e.g. Andréasson et al., 2005). The objective and constraint functions $f_i(\boldsymbol{u}, \rho)$ for $i = 0, m$ are real valued scalar functions with possibly complex input. The complex input is due to the state field $\boldsymbol{u}$ and is a consequence of the harmonic time dependence and the conductive material and/or the absorbing boundary conditions,

c.f. section 2.2.2. The general optimization problem can be formulated as

$$\begin{aligned} \min_{\rho\in\mathbb{R}^n} \quad & f_0(\boldsymbol{u}(\rho),\rho) && && \text{objective function} \\ \text{subject to} \quad & f_i(\boldsymbol{u}(\rho),\rho)\leq 0, && i=1,m && \text{constraint functions} \\ & \boldsymbol{S}(\rho)\boldsymbol{u}-\boldsymbol{b}=0 && && \text{state equation} \\ & 0\leq\rho^e\leq 1, && e=1,n && \text{design variable bounds} \end{aligned} \tag{3.5}$$

where n is the number of design variables and m is the number of inequality constraints. In topology optimization it is common practice to use a so-called nested formulation, where the state equation is excluded from the optimization problem by making the solution to the state problem part of the objective and constraint evaluation (Bendsøe and Sigmund, 2004).

The topology optimization problems considered in this work are smooth but non-convex optimization problems. This means that global optimality cannot be guarantied, and that the result of the optimization in most cases will correspond to a local minimum.

The NLP in equation (3.5) can be solved for local optimality using a gradient based optimizer such as the Method of Moving Asymptotes (MMA) by Svanberg (1987). In order to apply a gradient-based optimizer the evaluation of sensitivities is required.

3.3.1 Sensitivities analysis

The sensitivities of a real function with complex input with respect to to the design variable, i.e. $\mathrm{d}f/\mathrm{d}\rho^e$, can be evaluating using the adjoint method (Michaleris et al., 1994; Jensen and Sigmund, 2005). for which the basic idea and main result is outlined in this section.

The idea is to formulate the input to the real valued function in terms of real and imaginary parts, i.e. $\boldsymbol{u}=\boldsymbol{u}_R+j\boldsymbol{u}_I$. The function and the state problem residual may then be written as

$$\begin{aligned} f &= f(\rho,\boldsymbol{u}_R,\boldsymbol{u}_I) \\ \boldsymbol{R} &= \boldsymbol{S}(\rho)\boldsymbol{u}-\boldsymbol{b}\ (=0) \end{aligned}$$

where $\boldsymbol{S}(\rho)$, $\boldsymbol{u}$ and $\boldsymbol{b}$ are complex quantities. The adjoint sensitivity analysis then follows by adding the residual multiplied by a Lagrange multiplier to the objective, i.e. adding a zero. Due to the complex problem both the residual and its complex transpose are added to form the following augmented Lagrangian

$$L=f+\boldsymbol{\lambda}_1^T(\boldsymbol{S}\boldsymbol{u}-\boldsymbol{b})+\boldsymbol{\lambda}_2^T(\bar{\boldsymbol{S}}\bar{\boldsymbol{u}}-\bar{\boldsymbol{b}}) \tag{3.6}$$

where $\bar{(\cdot)}$ refers to complex conjugate, $(\cdot)^T$ to the real transpose and $\boldsymbol{\lambda}_1$ and $\boldsymbol{\lambda}_2$ are Lagrange multipliers. The mechanics of the adjoint method consists of a series

of manipulations and a full derivation is given in appendix A. The outline of the analysis is to apply the chainrule to equation (3.6) which is necessary since $\boldsymbol{u}_R$ and $\boldsymbol{u}_I$ are implicit functions of ρ. Based on the same reasoning the terms involving $\partial \boldsymbol{u}_R / \partial \rho^e$ and $\partial \boldsymbol{u}_I / \partial \rho^e$ are equated to zero. Finally, it can be shown that $\boldsymbol{\lambda} = \boldsymbol{\lambda}_1 = \bar{\boldsymbol{\lambda}}_2$ and the sensitivity can be expressed as

$$\frac{\mathrm{d}f}{\mathrm{d}\rho^e} = \frac{\mathrm{d}L}{\mathrm{d}\rho^e} = \frac{\partial f}{\partial \rho^e} + 2\mathbb{R}\left(\boldsymbol{\lambda}^T \left[\frac{\partial \boldsymbol{S}}{\partial \rho^e}\boldsymbol{u} - \frac{\partial \boldsymbol{b}}{\partial \rho^e}\right]\right) \tag{3.7}$$

where $\boldsymbol{\lambda}$ is the solution to the adjoint problem

$$\boldsymbol{S}^T\boldsymbol{\lambda} = -\frac{1}{2}\left(\frac{\partial f}{\partial \boldsymbol{u}_R} - j\frac{\partial f}{\partial \boldsymbol{u}_I}\right)^T \tag{3.8}$$

Thus, in order to compute the sensitivities for the function f, only the derivatives $\partial f / \partial \boldsymbol{u}_R$ and $\partial f / \partial \boldsymbol{u}_I$ need to be evaluated while the system matrix can be reused for solving the adjoint problem. In fact, if $\boldsymbol{S}$ is symmetric and a direct solver is used, the factorization can be reused and thus lead to great savings in computational time.

3.3.2 Density filtering

To prevent optimized designs that contain isolated elements with $\rho = 1$, i.e. scattered metallic grains or small features, density filtering is used to impose a minimum length scale on the design. In this work two filtering methods are employed. These are the standard density filter (Bruns and Tortorelli, 2001; Bourdin, 2001) and the PDE filter (Lazarov and Sigmund, 2010; Kawamoto et al., 2010), respectively. The reason for including the two density filters, is that the standard filter becomes too memory consuming for 3D problems with large filter radius. This problem is remedied by the PDE filter, which in turn requires that the filter radius for the PDE problem is resolved by the FE mesh. This can pose a potential problem for small filter radii when using first order elements for the solution to PDE. Thus, the two filters are great compliments to each other.

The standard density filter can be stated as

$$\tilde{\rho}_e = \frac{\sum_{j \in N_e} w(\boldsymbol{x}_j) V_j \rho_j}{\sum_{j \in N_e} w(\boldsymbol{x}_j) V_j} \tag{3.9}$$

where $\tilde{\rho}_e$ is the filtered density, $\boldsymbol{x}_j$ is the coordinates of element j and V_j its volume. N_e is the neighborhood of element e with filter radius $R_{\min}$ specified by

$$N_e = \{j \mid \parallel \boldsymbol{x}_e - \boldsymbol{x}_j \parallel < R_{\min}\} \tag{3.10}$$

and the weight is given by $w(\boldsymbol{x}_j) = R_{\min} - \parallel \boldsymbol{x}_e - \boldsymbol{x}_j \parallel$.

Since the PDE filter is based on solving a PDE, it requires a continuous design field to be introduced. The extra field is only necessary when both the filtered field

$\tilde{\rho}$ and design field ρ are discontinuous, e.g. element wise constant. This is the case for the results presented in this thesis. The filter PDE can then be discretized using scalar nodal finite elements which yields the following linear system

$$\boldsymbol{K}_f \tilde{\tilde{\boldsymbol{\rho}}} = \boldsymbol{p} \tag{3.11}$$

where $\tilde{\tilde{\boldsymbol{\rho}}}$ is a vector of nodal design variables and the linear system is assembled from

$$\boldsymbol{K}_{f,e} = \int_V r \nabla \boldsymbol{N}_f \cdot \nabla \boldsymbol{N}_f + \boldsymbol{N}_f \cdot \boldsymbol{N}_f \mathrm{d}V \tag{3.12}$$

$$\boldsymbol{p}_{f,e} = \rho_e \int_V \boldsymbol{N}_f \mathrm{d}V \tag{3.13}$$

where $\boldsymbol{N}_f$ is a vector of nodal shape functions and $r = R_{\min}/2\sqrt{3}$ is the filter radius correction required for the PDE filter (Lazarov and Sigmund, 2010). The boundary conditions for the filter PDE should generally be chosen as Neumann conditions. The linear system in equation (3.11) is positive definite and can efficiently be solved using a Jacobi preconditioned conjugate gradient method (Saad, 2000). The filtered field is now obtained through the element wise operation

$$\tilde{\rho}_e = \frac{\int_V \boldsymbol{N}_f^T \tilde{\tilde{\boldsymbol{\rho}}}_e \mathrm{d}V}{\int_V \boldsymbol{N}_f^T \boldsymbol{N}_f \mathrm{d}V} \tag{3.14}$$

where $\tilde{\tilde{\boldsymbol{\rho}}}_e$ is the nodal design variables associated for element e.

For both filter types the sensitivities must be updated with respect to the filtered field. This is accomplished by application of the chain-rule and yields for the standard filter

$$\frac{\partial f}{\partial \rho_e} = \sum_{j \in N_e} \frac{\partial f}{\partial \tilde{\rho}_j} \frac{w(\boldsymbol{x}_e) V_e}{\sum_{i \in N_j} w(\boldsymbol{x}_i) V_i} \tag{3.15}$$

In case of the PDE filter one simply repeats the filtering process with the design variables, ρ_e, exchanged with $\frac{\partial f}{\partial \tilde{\rho}_e}$ and the filtered field, $\tilde{\rho}_e$, with $\frac{\partial f}{\partial \rho_e}$ in equation (3.13) and (3.14) respectively.

The use of a density filter will by construction introduce grey scale in the optimized design. This is of course undesirable and can be remedied in several ways. One method is to apply a Heaviside projection to the filtered field, and another method could be to reduce the filter radius using a continuation scheme. The latter cannot guaranty a minimum length, which the Heaviside projection method can. The final, and most crude, method for removing the intermediate densities is to simply threshold the filtered design field at a specified cutoff value upon convergence of the optimization process, and then perform post analysis.

3.3.3 The topology optimization flowchart

The iterative optimization procedure that constitutes the topology optimization approach can be seen in figure 3.2. The flowchart is divided into three separate

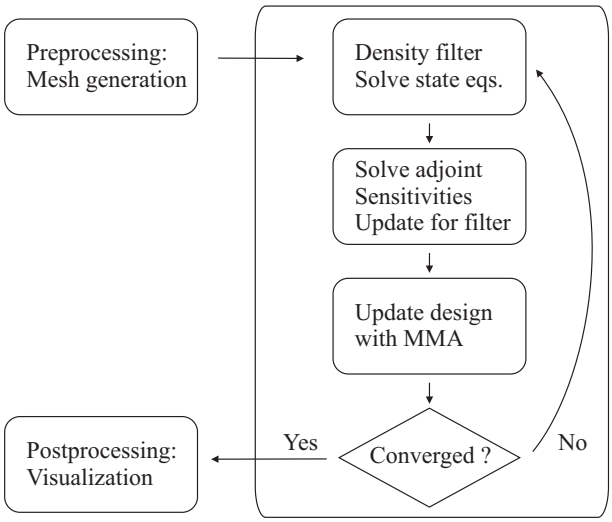

Figure 3.2 Flowchart for the topology optimization procedure.

sections. First the preprocessing, where meshing and problem data is initialized. This is followed by the iterative optimization process, which consists of repeatedly performing the filter operation, solving Maxwell's equation, computing the sensitivities and updating the design with MMA. Upon convergence the design and physical quantities are postprocessed and visualized. However, several user-defined parameters play a crucial role in the success of the optimization procedure. Since the problems investigated are non-convex the optimized designs are very likely to be local minima. Therefore several starting guesses, and thus several optimization runs, should be performed to ensure the best possible optimized design is obtained. The same reasoning applies to the filtering for which different filter radii should be used to ensure that a too large filter radius does not prevent the optimizer from reaching a significantly better local minimum.

Chapter 4
Implementation and the parallel optimization framework [P2]

The optimization problems investigated in this thesis cover both 2D and 3D electromagnetic wave problems. Though mathematically similar the problems in two and three dimensions require completely different numerical approaches to obtain an efficient solver that is fast enough to facilitate the optimization.

For 2D problems a finite element code is written in Matlab capable of solving the 2D Helmholtz problem using first order triangular nodal and edge elements. Furthermore an axi-symmetric formulation is implemented based on nodal elements. The resulting sparse linear system is solved using LU factorization and the design update is obtained using a Matlab implementation of MMA courtesy of K. Svanberg. The Matlab environment is however not suited for large 3D problems. This is mainly due to memory usage and lack of parallel subroutines. Therefore a 3D finite element code, based on first order edge elements, is implemented in a parallelized C++ framework. The C++ framework is based on the work of Lazarov and Augarde (2005), which has been extended during the work of this thesis to include complex numbers, complex linear solvers and a general non-linear constrained optimization algorithm, i.e. MMA. The 3D Maxwell solver is based on first order tetrahedral edge elements. The implementations in both Matlab and C++ are verified and tested by comparing the numerical results with analytical results as well as results obtained using Comsol Multiphysics.

The upcoming sections address the general structure and parallel scalability of the C++ framework and the parallel MMA implementation.

4.1 General structure of the parallel C++ framework

The parallel framework used for solving the 3D Maxwell problem is written in C++ and parallelized using OpenMPI (Gabriel et al., 2004). The reason for choosing the C++ programming language is to obtain an easily extendable, maintainable and versatile code. This can be achieved using concepts from object oriented (OO) programming. The OO approach allows for a clear communication interface between different objects within the framework. An example is the interface between an element object and a sparse matrix object, i.e. the assembly process. To perform an assembly the user does not need to know the global numbering of the dofs in the matrix nor the sparsity pattern, but only the local dofs and their respective values. The global indexing and parallel communication pattern is completely handled within the matrix object and can therefore be considered as hidden from the user.

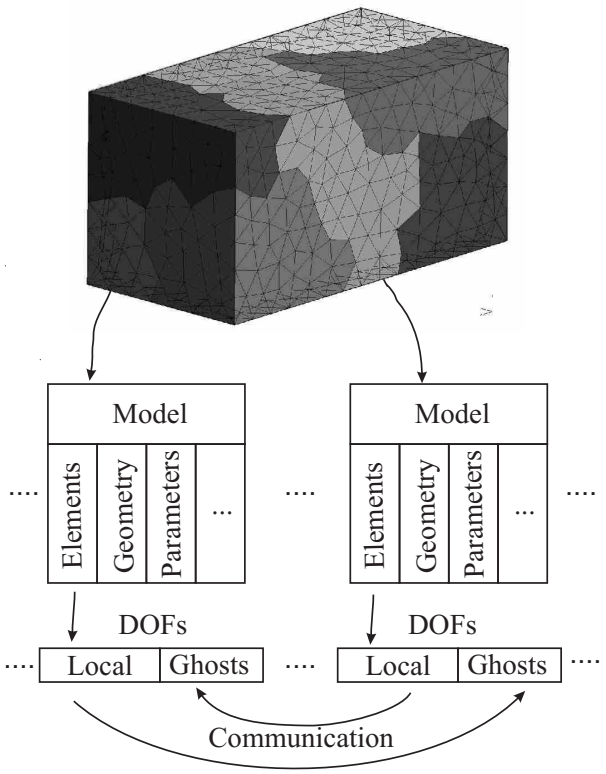

Figure 4.1 Outline of the parallel framework applied to the assembly of a distributed vector. Each shade of gray in the rectangular box corresponds to data which is local to a single core.

More details on the C++ framework are explained in [P2], while the key aspects and results of the implemented C++ framework are presented next.

The main advantage of the OO approach, and the justification for its use, is that implementing a general PDE constrained optimization problem only requires programming of the element objects required for the PDE problem and a driver program. The element object has clearly defined interfaces for dof assignment, matrix and vector assemblies, objective and constraint evaluations, sensitivities, etc., while the driver simply follows the standard topology optimization flowchart shown in section 3.3.3. The user is therefore *not* responsible for the bookkeeping and parallel communications that constitutes the majority of development time for any given parallel, or sequential, FE based optimization implementation.

In order to minimize the amount of communication required for parallel simulations the computational domain is decomposed using METIS (Karypis and Kumar, 1999). The resulting partitions are used as a basis for generating the input files which are read and parsed independently of each other within the C++ framework. The original mesh can be generated with any mesh tool capable of performing the tasks relevant for the given problem. In the work presented here both GMSH (Geuzaine and Remacle, 2009) and Cubit (Sandia Cooperation) are used for mesh generation

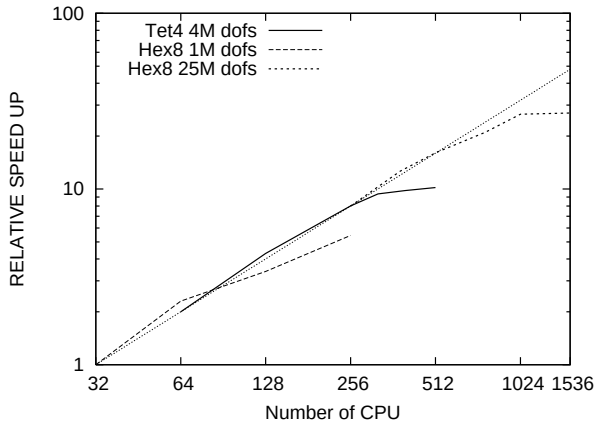

Figure 4.2 Parallel scalability of the C++ framework exemplified on a minimum compliance problem (Bendsøe and Sigmund, 2004) solved using a FSAI preconditioned conjugate gradient method. The scalability is shown in terms of relative speed up. With respect to time consumption it was found that the problem with 25 million dofs takes one minute per design cycle. The scaling study is performed on a Cray XT4/XT5 supercomputer.

while Matlab and the open-source program Paraview (`www.paraview.org`) are used for postprocessing the results. A schematic of the parallel framework is shown in figure 4.1, illustrating the assembly of a distributed vector. In figure 4.2 the parallel scalability of the framework is shown which clearly shows that the framework is capable of solving problems involving millions of dofs while maintaining good parallel performance.

Solving the 3D Maxwell problem is throughout the presented work done using the parallel LU factorization package MUMPS (Amestoy et al., 2000). The reason why an iterative solver has not been applied is due to the lack of an efficient preconditioner. The author has tried using preconditioners such as factorized sparse approximate inverse (FSAI) and incomplete LU combined with solvers such as GMRES, BiCGSTAB, BiCGSTAB-L and L-GMRES, but without success. To the best of my understanding the failure of these solvers is due to firstly, the ill-conditioning of the linear system due to large material contrasts often seen in topology optimization, and secondly, to the fact that edge based FE leads to extremely sparse linear systems (Zaglmayr, 2006) which prohibits, or slows down, the propagation of information within the iterative solvers. Note that good convergence is obtained for other high-contrast topology optimization problems, c.f. the design problems solved in [P2]. A possible cure for the lack of efficient preconditioners for curl-curl problem could be to use a multigrid method as preconditioner. This has been shown to work well for large problems with large variation in parameters, c.f. (Zaglmayr, 2006). Unfortunately, the time available has not allowed for a realization of this within the parallel framework. The consequence of using the direct solver is that scalability cannot be preserved, that memory usage is high and thus that the problem sizes are restricted to a few million complex dofs.

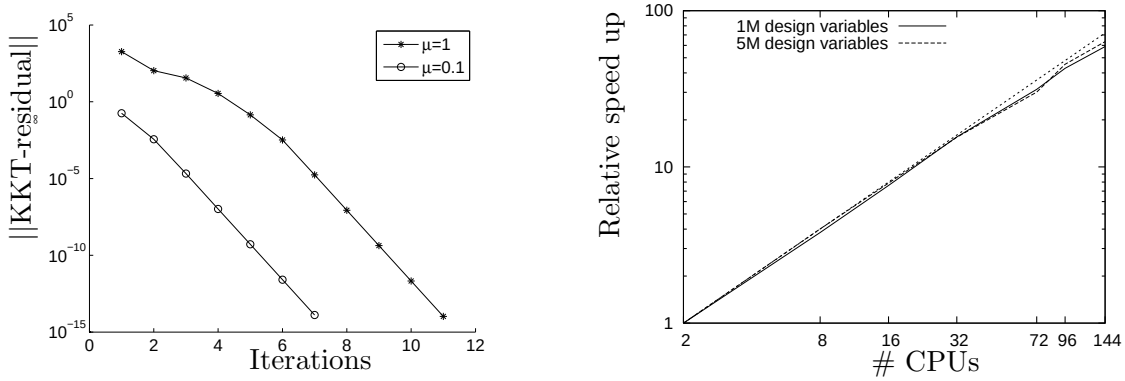

Figure 4.3 (a) second order convergence of the Newton solver used to solve the dual of the MMA subproblem for fixed barrier parameter μ. (b) parallel scalability of the MMA implementation as a function of the relative speed up.

4.2 Parallelized method of moving asymptotes

In order to make the parallel C++ framework capable of handling largescale optimization problems while maintaining scalability, the optimization algorithm must also be parallelized. This is necessary even though the amount of time spent within the optimizer usually is measured in term of tenths, or hundreds, of percents of the total computational time. The necessity for this can be exemplified by use of Amdahl's law (Amdahl, 1967), which states the relation between the possible parallel speed up, S, the number of CPUs, N, and percentage, P, of a program that is parallelized.

$$S = \frac{1}{1 - P + \frac{P}{N}} \tag{4.1}$$

As an example consider the case in which the optimizer uses 0.05% of the total computational time. In this case using 600 CPUs will only lead to a speed up of 400. Therefore the optimizer implemented within the C++ framework has been fully parallelized.

The optimizer implemented in the parallel framework is MMA, which is chosen due to the wide range of problems for which it has demonstrated very good results. MMA is also very attractive with respect to parallel computations. The good parallel characteristics of MMA are associated with the separability of the of approximations. This feature makes it possible to keep much of the work local to each processor and to collect all communications inside matrix-matrix and matrix-vector operations. Such operations have a good ratio of local data manipulations to communications and should thus ensure an efficient parallel implementation. In [P2] a detailed description of the implemented interior point dual solver is given. The main results of [P2] can be seen in figure 4.3, which shows the convergence of the Newton method to be second order and that the implementation has very good parallel performance.

Chapter 5
Energy focusing devices

The first type of optimization problems considered in this thesis, is that of energy focusing devices. For these problems the goal is to distribute conducting material such that the electric or magnetic energy is maximized within a specified objective domain. The results presented in this chapter consist of examples and findings from [P1], [P3] and [P4] as well as additional results based on the design of Fresnel zone plate lenses. The optimization problem can be formulated as

$$\begin{aligned} \max_{\rho\in\mathbb{R}^n} \quad & f_0 = \log_{10}\left(\textstyle\int_{\Omega_{\text{obj}}} |\alpha \boldsymbol{u}|^2 \mathrm{d}\Omega\right) \\ \text{subject to} \quad & \tfrac{\sum_e^n \rho_e V_e}{V f^*} - 1 \leq 0 \\ & \boldsymbol{S}(\rho)\boldsymbol{u} - \boldsymbol{b} = 0 \\ & 0 \leq \rho^e \leq 1, \quad e = 1, n \end{aligned} \tag{5.1}$$

where the objective, f_0, is based on either the time averaged magnetic energy, $\frac{1}{4}\left|\mu_r \boldsymbol{H}\right|^2$, or the time averaged electric energy, $\frac{1}{4}\left|\epsilon_r \boldsymbol{E}\right|^2$ (Balanis, 1989). A volume constraint is added, since such a constraint in some cases has been observed to speed up convergence. The logarithm is applied to scale the objective since numerical experiments have shown that this leads to better performance of the optimizer. To maintain consistency with respect to units when applying the logarithm, the energy is first scaled by some reference energy to obtain a non-dimensional energy measure.

Focusing of electromagnetic energy is an essential component in many technologies covering most of the electromagnetic spectrum. As examples one may consider energy focusing devices used for energy harvesting from RF and microwave ambient electromagnetic fields, or focusing devices for antennas used to enhance the electromagnetic field in the antenna aperture and thus improve the reception or transmission.

5.1 2D magnetic resonator [P1,P4]

The first optimization problem investigated is the design of a magnetic resonator, which can be regarded as the design of a simplified energy harvesting device. The physics is modeled in 2D assuming transverse electric (TE) polarization, i.e.

$$\begin{aligned} \boldsymbol{H} &= H_z(x,y)\boldsymbol{e}_z \\ \boldsymbol{E} &= E_x(x,y)\boldsymbol{e}_x + E_y(x,y)\boldsymbol{e}_y \end{aligned} \tag{5.2}$$

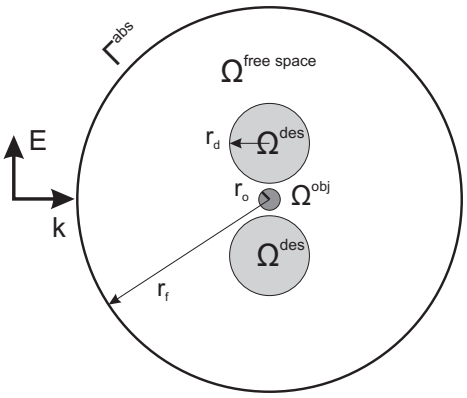

Figure 5.1 Sketch of design problem with $r_d = 0.65\ m$, $r_o = 0.08\ m$ and $r_f = 3.0\ m$. The target frequency is 115 MHz and the materials are a good conductor e.g. copper and air. No explicit symmetry is enforced on the two design domains.

The system is excited by an incident plane wave at 115 MHz and a sketch of the design problem can be seen in figure 5.1. The outer boundary is truncated using a first order absorbing boundary condition. This problem can be solved either for the scalar magnetic field or the vector electric field. If solved for the magnetic field the vector wave equation is reduced to the scalar Helmholtz equation, and if solved for the electric field the wave equation is reduced to a curl-curl vector problem in the plane. In [P1] both solution strategies are demonstrated, while only the results obtained using the scalar formulation is presented here. The objective function is a non-dimensional magnetic energy measure, i.e.

$$f_0(H_z(\rho)) = \log_{10}\left(\frac{1}{\phi_0}\int_{\Omega_{\text{obj}}} |\mu H_z|^2 \,\mathrm{d}\Omega\right) \tag{5.3}$$

where $\phi_0 = 4\pi 10^{-7}$ J. In order to evaluate the performance of the optimized design a reference energy is computed based on the configuration shown in figure 5.1 with all design elements having $\rho = 1$, i.e. conducting material. The reference objective function was found to be $f_0^{\text{ref.}} = -0.68$. The design problem is solved using an allowed volume fraction of 30%, a radius of $R_{\min} = 0.1$ m using the standard density filter and a uniform initial distribution of $\rho_{\text{init}} = 0.3$. The optimization process is terminated when $||\rho^k - \rho^{k-1}||_\infty < 3\%$ is fulfilled.

The optimized design in figure 5.2(a) is obtained using a total of 20000 design elements, without any requirement of symmetry on the two design cylinders. A close inspection of the optimized design reveals that the two design domains are not exact mirrored copies of each other, though they appear, quantitatively, to be symmetric about the x-axis. The lack of symmetry is contributed to the fact that the mesh itself is not symmetric. Upon convergence the volume constraint is active, i.e. all available material has been utilized by the optimizer. In order to obtain a design that is not contaminated with grey design elements, the problem is run using a continuation

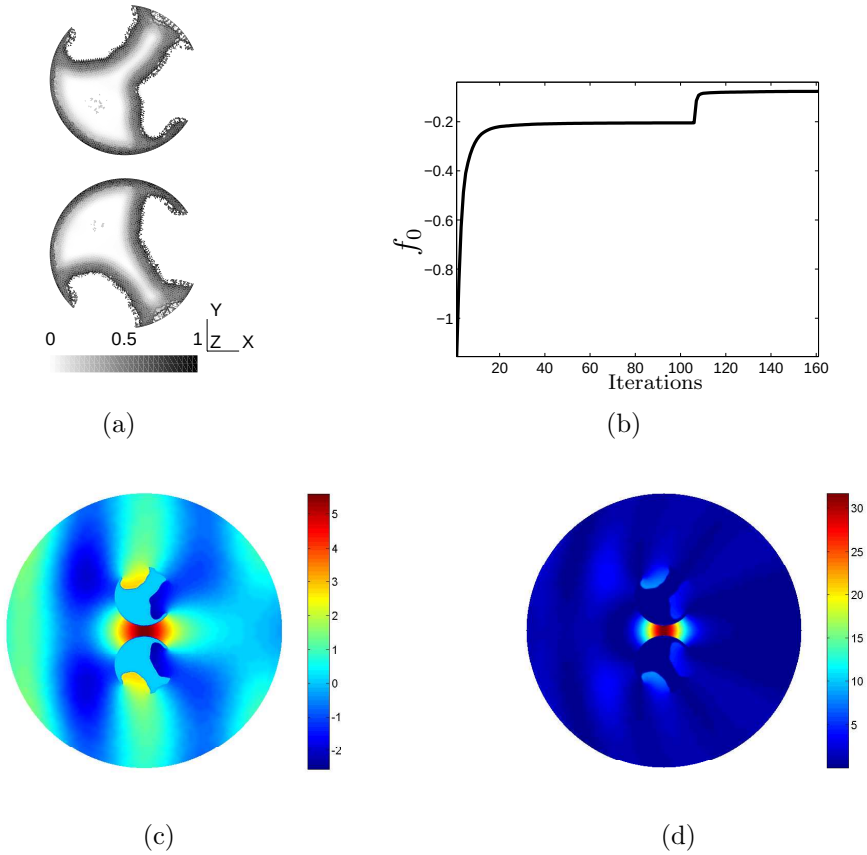

Figure 5.2 Optimized design (a) for the design problem in figure 5.1. The number of design elements are 20000 nodal elements. The optimized design performs approximately 400 % better than the reference design. The jump in the convergence history (b) is due to the continuation approach applied for the filter radius. Figure (c) and (d) shows the magnetic field and energy, respectively, and clearly indicates that the design parameterization behaves as expected.

approach for the filter radius. That is, the optimization is first performed using a fixed filter radius and upon convergence the filter turned off and the optimization is continued until convergence. This gives rise to a jump in the objective function which is also seen in the convergence history shown in figure 5.2(b). The optimized design has an objective of $f_0 = -0.076$ which is a 400% improvement in magnetic energy compared to $f_0^{\text{ref.}}$. Even though the continuation approach is used for the filter, there are still grey elements in the final design. However, the intermediate design variables are primarily located within the optimized structure. From the field and energy plots of figure 5.2(c) and (d) it is clear that this region does not affect the performance of the device, since the magnetic energy is (numerically) zero on the interior of the design.

The optimized design is validated by postprocessing the design into a pure 0-1 design. The truncation is performed such that all $\rho \geq 0.5$ is set to one and all

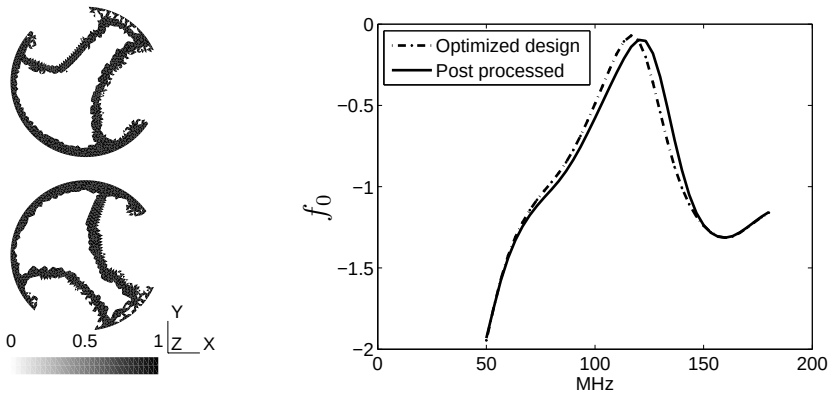

(a) (b)

Figure 5.3 Post processing results based on the optimized design in figure 5.2. The threshold for the design field is chosen such that $\rho^e > 0.5 \rightarrow 1$ and zero for all other elements. The design is shown in (a). In (b) a frequency sweep of the objective function, shows that the post processed design has maximum at 120 MHz with $f_0 = -0.076$, while the optimized design has $f_0 = -0.07$ at 116MHz.

other to zero. The postprocessed design is then analyzed with PEC conditions on all boundaries. The resulting 0-1 design and the corresponding frequency sweep can be seen in figure 5.3. From the frequency sweep it is seen that the objective value of the postprocessed design and the optimized design are in good agreement. However, the postprocessed design displays a 4% increase in resonant frequency. A shift in resonant frequency was also observed in Diaz and Sigmund (2010), where postprocessed designs showed a general tendency to have an increase in resonant frequency compared to that of the optimized designs containing grey elements. For the optimized designs presented in [P1] not all postprocessed designs gave rise to an increase in resonant frequency. In fact, for the electric resonator in [P1-fig.11] a small decrease was observed. It should therefore be emphasized that while the proposed interpolation functions of course have clear interpretations in the limits of either $\rho = 0$ or $\rho = 1$, the functions are merely an optimization instrument in the intermediate regime. As a consequence of this, small discrepancies are to be expected when performing analysis on optimized design which are rendered completely 0-1.

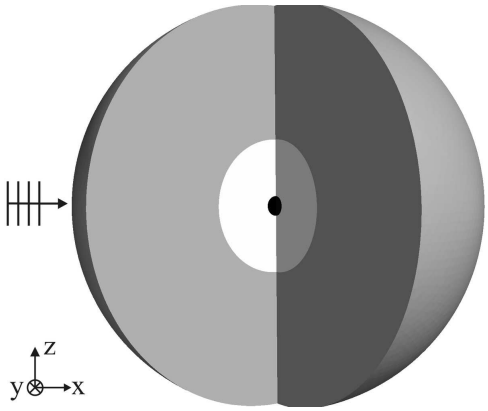

Figure 5.4 Illustration of the design problem for the 3D electric resonator problem. The white sphere with $r = 1$ m corresponds to the design domain, the black sphere with $r = 0.08$ m to the objective and the grey sphere with $r = 3$ m to free space. The target frequency is 120 MHz and $\sigma^m = 10^7$ S/m and $\sigma^d = 10^{-4}$ S/m. The design domain is illuminated by a plane wave with unit amplitude traveling along the x-axis (left to right) with polarization in the z-direction.

5.2 3D electric resonator [P3]

The second optimization problem to be investigated is the design of a 3D electric energy focusing device. The design problem can be seen in figure 5.4 and the objective is to maximize the electric energy in a sphere with radius $r = 0.08$ m situated in the center of a spherical design domain with radius $r = 1$ m. The freespace domain has radius $r = 3$ m and the target frequency is 120 MHz. The objective is in this case based on the electric energy, which leads to the following expression

$$f_0(\boldsymbol{E}(\rho)) = \log_{10}\left(\frac{1}{\phi_0}\int_{\Omega_{\text{obj}}} |\epsilon \boldsymbol{E}|^2 \,\mathrm{d}\Omega\right) \tag{5.4}$$

where $\phi_0 = 4\epsilon_0$ J is used to scale, and non-dimensionalize the electric energy.

The discretized problem has approximately 10^6 complex state dofs and a total of $3.8 \cdot 10^5$ design variables. The mesh is partitioned into 72 parts and each design cycle takes approximately 3 minutes.

The optimization problem is solved using an allowed volume fraction of 60%, a filter radius of $R_{\min} = 0.08$ m for the PDE filter and a uniform initial distribution of $\rho_{\text{init}} = 0.3$. The optimization process is terminated when $||\rho^k - \rho^{k-1}||_\infty < 1\%$ is fulfilled. In order to have a frame of reference to which the performance of the optimized design can be compared, the electric energy is computed for the case where all $\rho = 0$. The reference objective is found to be $f_0^{\text{ref.}} = -1.88$. Using these settings the optimization process converged in 201 iterations having used 35% of the available material, i.e. the volume constraint was inactive, with a final objective of $f_0 = 0.98$. This corresponds to a 723 fold improvement to the reference energy.

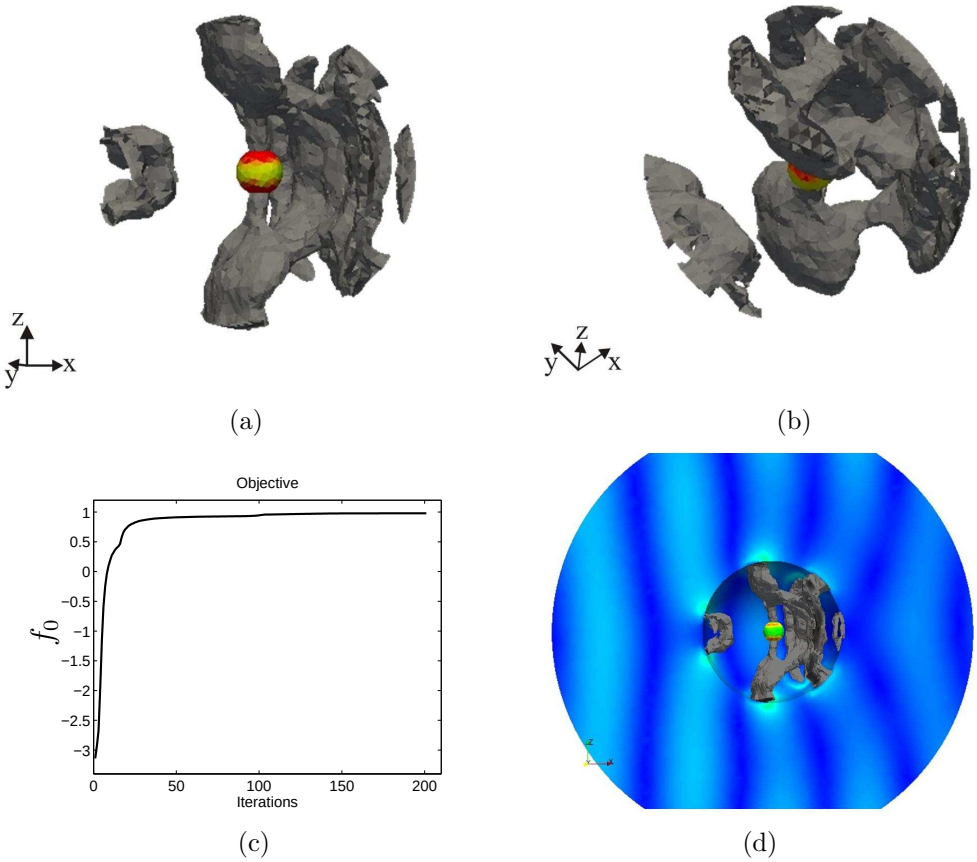

Figure 5.5 Optimized design for the problem in figure 5.4 at 120 MHz. Isosurface plots of the design are seen in (a) and (b), where $\rho > 0.5$ is used as cut off. In figure (c) the convergence is shown and in (d) the electric field and the design is shown together. The incident plane way travels along the positive x-axis (from left to right) and is polarized in the z-direction.

The optimized design can be seen as isosurface plots in figure 5.5(a) and (b). The convergence history in figure 5.5(c) is seen to be smooth and in figure 5.5(d) the design is shown together with a slice of the electric field. The optimized design has the overall shape of a parabola with a reflector centered in front of it. Also it is seen that two arms touch the objective domain. This design makes intuitive sense, since such a structure will first reflect the incident wave towards the small reflector, which will then reflect the wave back into the objective domain. The two arms that are in contact with the objective domain allow the electric field to flow from one arm to the other, similar to how charge build-up in a capacitor.

This optimization result exemplifies the advantage of using topology optimization, since the optimized design consists of two separated volumes of conducting material, i.e. the topology has changed. Based on the findings of [P1,P4] and the example shown above from [P3] it is concluded that the proposed design parameterization makes it possible to apply topology optimization for the distribution of

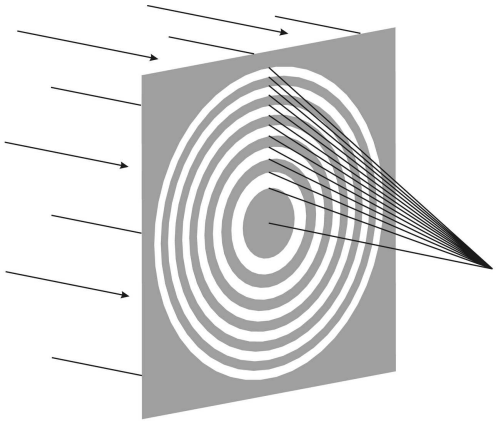

Figure 5.6 Schematic of a Fresnel plate zone lens. The grey regions corresponds to a transparent medium (air) and the white regions to an opaque material (a good conductor). The figure illustrates how the Fresnel plate zone lens, by diffraction, is capable of focusing the electromagnetic field in a point at a distance F from the lens.

conductive material without the need for the finite element mesh to resolve the skin depth.

5.3 Fresnel plate zone lens

The last design problem concerning energy focusing devices is based on Fresnel plate zone lenses (Minin and Minin, 2004). The Fresnel zone lens was originally invented by A.J Fresnel. The Fresnel zone lens was successful because it made it possible to construct efficient lenses with large apertures compared to the focal length, while using much less material than conventional lenses. A planar variant of the Fresnel lens, known as the Fresnel plate zone lens, is investigated in this section with respect to optimization. A schematic of a Fresnel plate zone lens can be seen in figure 5.6. The Fresnel plate zone lens consists of alternating rings of opaque and transparent material, with ring sizes that are comparable to the wavelength of the electromagnetic wave. In the RF and microwave regime the materials could be e.g. a conducting material and air. Unlike conventional lenses, the Fresnel zone plate lens use diffraction instead of refraction to focus the electromagnetic wave. It should also be noted that the standard layout of Fresnel plate zone lenses assumes that the incident field is normal to the aperture, but has no restriction on the polarization of the incident electromagnetic field. The radii of the different rings can be computed using the following analytic formula (Thompson and Vaughan, 2009)

$$r_n = \sqrt{n\lambda F + \left(\frac{n\lambda}{2}\right)^2} \tag{5.5}$$

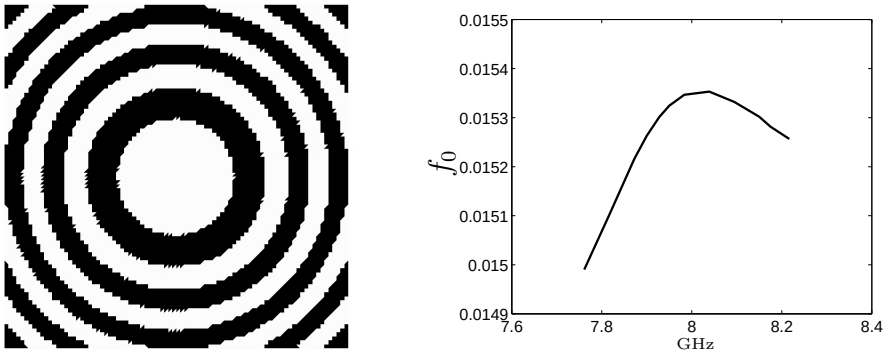

(a) (b)

Figure 5.7 Reference design of a Fresnel plate zone lens at 8 GHz with three full rings and a focal length of 15 cm (a). The frequency sweep in (b) shows that the electric energy has a maximum of 0.01535 J at 8.05 GHz.

where r_n is the radius of the nth ring, λ the wavelength and F the focal length, i.e. the distance from the lens to where the energy should be focused. A microwave application for the Fresnel plate zone lens is e.g. to use the device in front of antennas, e.g. a horn antenna, to focus the electromagnetic wave and thereby enhance the transmission and reception (Hristov and Herben, 1995).

In order to evaluate the performance of the optimized designs presented next, a reference example based on the analytic result in equation (5.5) is analyzed. The frequency is chosen to be 8 GHz, i.e. a wavelength of $\lambda = 3.75$ cm, and the focal length to $F = 15$ cm. The reference example consists of three full Fresnel zones in a design domain with dimensions $0.001 \times 0.43 \times 0.43$ m. The electric energy is evaluated in a sphere of radius 0.005 m centered a distance F from the design domain. The reference design can be seen in figure 5.7 along with a frequency sweep. The frequency sweep shows a maximum energy of 0.01535 J at 8.05 GHz. The mesh used for the analysis yields a total of $2.53 \cdot 10^6$ dofs and $4.5 \cdot 10^4$ design variables. The mesh is partitioned into 144 parts and the analysis is performed on an Infiniband connected cluster consisting of 55 nodes with each 2 Intel Xeon quad core L5520 processors working at 2.27 GHz with 24 GB memory. Each linear system requires approximately five minutes of wall-clock time to be solved.

The first optimization problem investigates the outcome when restricting the plate zone lens to be optimized for only a single polarization. The initial design is a uniform distribution of $\rho = 0.3$ and a standard density filter with radius $R_{\min} = 0.01$ m is used. The optimization process is terminated when $||\rho^k - \rho^{k-1}||_\infty < 1\%$ is fulfilled or when the iterations exceed 300 design cycles. The optimized design is rendered 0-1 by setting all $\rho > 0.5$ to one and all others to zero. Based on the 0-1 design a single post processing analysis is performed at 8 GHz. The optimized design can be seen in figure 5.8 and was found to have an electric energy of 0.0176 J. This corresponds to a 14.3 % better performance than that of the reference design.

(a) (b)

Figure 5.8 Optimized design at 8 GHz with a focal length of 15 cm using only a z-polarized incident field. The electric energy for the optimized design is 0.0176 J. (a) the optimized design seen in the yz-plane and (b) a slice of the electric energy seen in the xz-plane. High energy corresponds to white areas and black areas to low energy.

Inspection of the optimized design in figure 5.8(a) reveals a high level of similarity to the reference plate zone lens in figure 5.7(a). That is, the rings constituting the Fresnel zones are clearly present with average sizes comparable to those of the reference design. However, the optimized design does not consist of smooth circular rings, but rather circles with shark tooth like structures in either vertical or horizontal directions. It is also seen that a vertical bar has appeared in the center of the inner transparent zone. These artifacts are all contributed to the z-polarized incident field. From the energy plot in figure 5.8(b) it is seen that there is a high energy intensity to the right of the computational domain, which coincides with the objective domain.

The second optimization problem is an extension of the previous problem to include all polarizations in the yz-plane. Due to the principle of superposition this can be achieved by solving the Maxwell problem for two right hand sides, or load cases. The only requirement is that the two load cases should be orthogonal with respect to each other. So, if the first incident wave travels along the positive x-axis with the electric field oscillating in the z-direction, the second incident wave should be polarized in e.g. the positive y-direction. Since both incident waves oscillate at the same frequency, the system matrices for the two problems are identical, and as a consequence only a single factorization is needed. This means that the numerical cost of the modified problem is very low. The resulting optimization problem is naturally formulated as a max-min problem, i.e.

$$\max_{\rho \in \mathbb{R}^n} \quad \min_{k \in \{1,2\}} \quad f_k(\boldsymbol{u}_k, \rho) \tag{5.6}$$

where k refers to the index of the two loads. When the magnitude of the incident fields are chosen to be equal, the max-min formulation should ensure that the optimized design performs equally well for both polarizations. However, the max-min

(a) (b)

Figure 5.9 Optimized design at 8 GHz with a focal length of 15 cm using both a z- and a y-polarized incident field. The electric energy for the optimized design is 0.0159 J for both polarizations. (a) the optimized design seen in the yz-plane and (b) a slice of the electric energy seen in the xz-plane.

formulation is non-smooth and can therefore not readily be solved using a gradient based optimizer. To circumvent this limitation a common trick is to recast the optimization problem on an equivalent smooth form, i.e.

$$\begin{aligned} \max_{\rho\in\mathbb{R}^n,\beta\in\mathbb{R}} \quad & \beta \\ \text{subject to} \quad & \beta - f_k(\boldsymbol{u}_k,\rho) \leq 0 \quad k=1,2 \\ & \frac{\sum_e^n \rho_e V_e}{Vf*} - 1 \leq 0 \\ & \boldsymbol{S}(\rho)\boldsymbol{u}_k - \boldsymbol{b}_k = 0 \quad k=1,2 \\ & 0 \leq \rho^e \leq 1, \qquad e=1,n \end{aligned} \tag{5.7}$$

where an extra design variable, β, has been introduced to yield a smooth formulation. This problem can readily be solved by MMA.

The mesh, initial design, filtering radius and stopping criteria is chosen equal to that of the single polarization example. The optimized design can be seen in figure 5.9(a) and was found to have an electric energy of 0.0159 J for both polarizations which is 3.8% better than the reference. The energy plot in figure 5.9(b) shows how the energy is focused in the area which corresponds to the objective domain. Comparing the optimized design with the reference design in figure 5.7 the similarities are striking. Though the designs are similar, i.e. the same number of rings, the optimized design is seen to consist of rings that are less smooth than those in the reference design. This is especially evident for the inner ring. If this difference is a numerical artifact due to the coarse mesh used for the design domain, or if it indicates that the optimizer can benefit from creating uneven ring surfaces is not known. It could therefore be interesting to heavily refine the design domain mesh

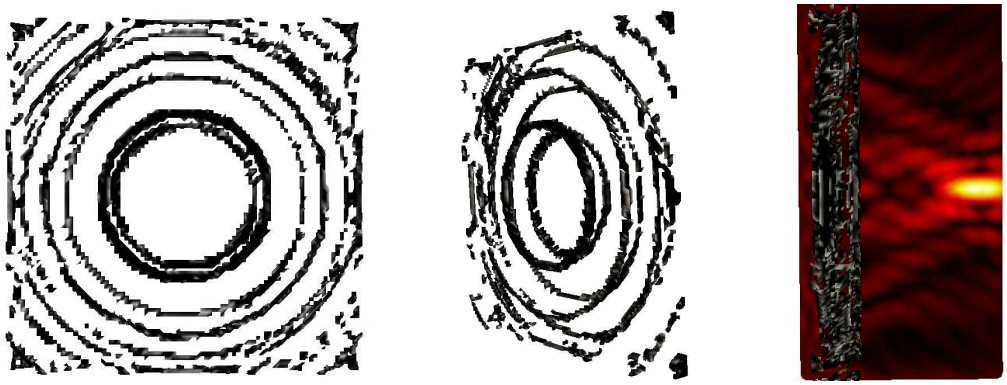

(a) (b) (c)

Figure 5.10 Optimized design at 8 GHz with a focal length of 15 cm using both a z- and a y-polarized incident field. The design domain has dimensions $0.05 \times 0.43 \times 0.43$ m . The electric energies for the optimized design is 0.0204 J and 0.0205 J for the two polarizations respectively. (a) and (b) optimized design seen from the front and side, respectively, and (b) a slice of the electric energy in the xz-plane.

and rerun the optimization. Unfortunately, this is not possible due to the limitations on problem size which can be solved using MUMPS and the available hardware.

For the third and final optimization problem the design domain is extended to be volumetric instead of planar. The new dimensions for the design domain are $0.05 \times 0.43 \times 0.43$ m. The focal length is still $F = 0.15$ m and is measured as the distance from the left wall of the design domain, to the center of the sphere in which the energy is evaluated. The design domain is meshed into $4.6 \cdot 10^5$ elements and the total number of dofs for the computational domain is $2.35 \cdot 10^6$. Note that though the design domain contains ten times as many elements as the planar design problem, the thickness is increased 50 times. Thus, the design representation is in fact 5 times coarser than for the planar design problems. The remaining optimization settings are identical to those used in the two previous problems, with the only change being that the PDE filter is used instead of the standard density filter.

The optimized design can be seen from two different angles in figure 5.10(a) and (b). The electric energy was found to be 0.0204 J and 0.0205 J for the respective polarizations which is approximately a 33% improvement in performance compared to the reference example. As was the case for the planar designs, the optimized design resembles the analytic Fresnel plate zone lens and the slice-plot in figure 5.10(c) shows that the energy is focused in the objective domain. However, the opaque zones are in this case much narrower than the analytical prediction. This could very well be a result of the coarse mesh used for the design domain. That is, each element layer in the design domain is approximately 0.005 m wide in the direction of the propagating wave. It is also interesting that the optimized design consists mainly of two layers of Fresnel zones, each situated at opposite walls of the design domain. This is likely related to the fact that the distance between the

layers are approximately 4 cm, which is close to the wavelength at 8 GHz. Also the Neumann boundary conditions for the PDE filter could be responsible for placing the material near the design domain surfaces. This is because the Neumann conditions is a symmetry condition, and the filter, and thus the optimizer, assumes that the the design is mirrored in the design domain boundaries. This certainly affects the optimized design and it would therefore be interesting to investigate the effect of using different types of Dirichlet conditions for the PDE filter.

For all of the three presented optimized designs in this section, it would be very interesting to apply a continuation approach for the filter radius, or a Heaviside projection, in order to render the optimized design completely 0-1, as opposed to the brute force postprocessing applied here.

Chapter 6
Antenna design [P3]

The design of sub-wavelength antennas, i.e. antennas with dimensions much smaller than the wavelength, has received much attention in the past two decades. This is a direct consequence of the ever increasing use of small hand-held electrical devices, e.g. cellular phones and GPS units, as well as small autonomous devices such as wireless sensors, hearing aids and medical implants. For many of these devices standard antenna configurations are found to be inadequate and the electrical engineers are therefore confronted with new design challenges. In this section a design formalism applicable to the systematic design of sub-wavelength antennas for wireless communication is presented. The results are examples of the findings given in [P3].

6.1 Antenna optimization

The layout of an antenna is determined subject to one of several possible main objectives depending on the specific application. The objective could be to design an antenna that works at a single operational frequency, several operational frequencies or for a large range of frequencies. A common goal, for all antenna design problems, is to ensure that the radiated power is as large as possible. That is, if 1 W is fed into the antenna it should, if possible, radiate 1 W of power at the operational frequency. The radiation efficiency can thus be defined as the ratio of power radiated to the power accepted by the antenna (Balanis, 2005). In addition to these main objectives, requirements on the directivity could also be imposed. In some cases a single direction is adequate, e.g. satellite communication, and in other applications an omni-directional antenna is desirable, e.g. cellular phones.

In this work the focus is on the design of a single frequency sub-wavelength antenna with high efficiency. A good choice of objective function in this case is the power flow. This can be computed based on the time-averaged Poynting vector (Balanis, 1989) and can be stated as

$$f(\boldsymbol{E}(\rho)) = \int_{\Gamma} \boldsymbol{n} \cdot \left(\frac{1}{2} \mathbb{R} \left[\boldsymbol{E} \times \bar{\boldsymbol{H}} \right] \right) \mathrm{d}\Gamma \tag{6.1}$$

where $\bar{(\cdot)}$ refers to the complex conjugate, Γ is a surface enclosing the antenna, i.e. a (hemi-)sphere, and $\boldsymbol{n}$ refers to an outward unit normal to this surface. Another useful parameter relevant for determining the characteristics of an antenna is the reflection coefficient, also called the S_{11} parameter, which can be expressed as

$$S_{11} = \frac{\int_{\Gamma} (\boldsymbol{E} - \boldsymbol{E}_0) \cdot \bar{\boldsymbol{E}}_0 \mathrm{d}\Gamma}{\int_{\Gamma} |\boldsymbol{E}_0|^2 \mathrm{d}\Gamma} \tag{6.2}$$

where $\boldsymbol{E}_0$ refers to the mode(s) of the signal fed to the antenna, and the integration is performed on the surface that terminates the feed line. In many practical cases the antenna is fed by a coaxial cable and in this setting $\boldsymbol{E}_0$ would refer to its fundamental Transverse Electric and Magnetic (TEM) mode, see e.g. Balanis (1989) for details. Based on the reflection coefficient it is possible to compute the operational bandwidth of the optimized antenna.

6.2 The two phase procedure

The motivation for introducing a two step optimization procedure is rooted in the way an antenna is fed. That is, an antenna works by coupling the signal from the feed into the antenna structure. The signal will then flow along the surface of the antenna structure and, if the antenna is designed properly, radiate into space (Balanis, 2005). This means, in the absence of an already functioning antenna structure, that the field intensity will be localized at the feed line termination and (numerically) zero elsewhere in the design domain. From the sensitivity expression in equation (3.7), it is evident that a zero electric field will result in zero sensitivities in cases where the load is design independent and the objective has no explicit design dependence. This means that the optimizer will have to evolve the antenna structure as a front originating at the feed point. From numerical experiments it was observed that this approach, in virtually all cases, converged to a local minima, for which the radiation efficiency was too low to yield a functional antenna, i.e. a maximum radiation efficiency of 10 %.

In order to remedy this limitation, and make the optimization approach applicable to design problems in which an initial design is not available a two phase optimization procedure is used. The main idea of the phase I design problem is to invert the antenna optimization task. Instead of feeding the system through the coaxial cable and maximizing the power flow over the truncation boundary, the system is fed by a number of incident waves, prescribed on the truncation boundary, and the power flow is maximized at the coaxial port. This should, based on the findings from the energy focusing examples, result in a design problem for which the sensitivities are not localized. Note that it is generally not possible to determine a correct and proper excitation in order to obtain a true inverse design problem. However, since the goal of the inverse design problem is not to design the actual antenna, but merely to obtain a design adequate for use as an initial guess, the number of incident waves can be kept finite and in practise quite low. Following the same line of arguments it is also not necessary to let the phase I problem converge. Instead a heuristic stopping criteria of 30 design cycles is used, since experience shows that after this number of iterations most topology optimization problems only displays little change in the objective function. The objective function for the

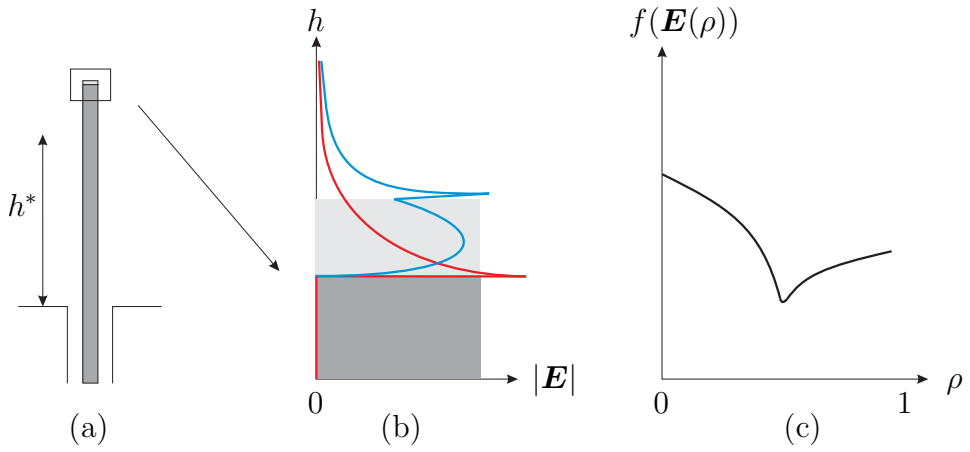

Figure 6.1 Illustration of how sharp material interfaces affects the optimization process. (a) a coaxially fed monopole antenna with $h > h^*$, where h^* refers to the optimal height. (b) field intensity at the tip of the monopole for two different design variable distributions. In both cases dark gray corresponds to $\rho = 1$ and white to $\rho = 0$. For case one, the light grey refers to $\rho = 0$ and gives rise to the red field intensity curve. For case two, $\rho = 0.5$ in the light gray region, which corresponds to the field intensity shown as the blue curve. (c) illustration of how different values of ρ in the light gray region affects the radiated power.

phase I problem can formally be stated as

$$\max_{\rho \in \mathbb{R}^n} \quad \frac{1}{q} \sum_{k=1}^{q} \log_{10} \left(\frac{1}{\phi_{\text{ref}}} f_k(\boldsymbol{E}_k(\rho)) \right) \tag{6.3}$$

where $\phi_{\text{ref}} = 1$ W is used to non-dimensionalize the argument for the logarithm and $f_k(\boldsymbol{E}_k(\rho))$ refers to the power flow, equation (6.1), evaluated at the coaxial port for each of the q incident waves. As was the case for the max-min problems solved for the focusing devices in chapter 5, the frequency is fixed for all incident waves. This means that the increase in number of load cases comes at a very low numerical cost.

The phase II problem consists of solving the original antenna optimization problem to achieve the best possible radiation efficiency.

6.3 The influence of sharp material interfaces

The concentration of the electric field intensity along the surface of the antenna structure complicates the optimization process by the introduction of artificial local minima. The artificial minima are caused by sharp material interfaces, and can be exemplified by a simple sizing problem, in which the height, h, of a monopole antenna is to be optimized. This problem has an analytical solution with $h^* = 0.21\lambda$ (Balanis, 2005). The monopole sizing problem is illustrated in figure 6.1(a) for the case where $h > h^*$. Figure 6.1(b) shows a zoom-in of two different density distributions. For both cases the dark grey region correspond to $\rho = 1$ and white

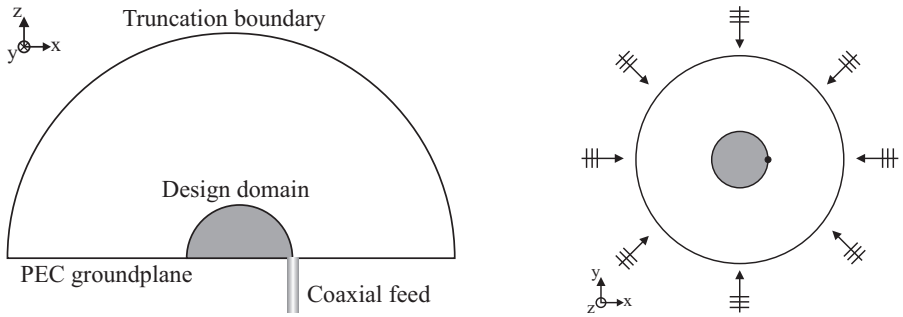

Figure 6.2 Sketch of the modeling domain for the optimization of an 3D sub-wavelength antenna. (a) slice of the modeling domain in the xz-plane and (b) top view including the direction of the incident waves for the phase I problem. Both freespace and design domains are hemispheres with radii of $r = 1$ m and $r = 0.08$ m, respectively. The free space domain is truncated by a first order ABC and the target frequency is 300 MHz. The design domain is connected by a 50 Ohm coaxial cable with an inner conductor radius of $r = 2$ mm. The inner conductor of the coaxial cable is extended 1 cm into the design domain in order to properly connect the feed line with the design. The length of the coaxial cable is $l = 0.12$ m.

to $\rho = 0$. In case one, the light grey region corresponds to $\rho = 0$, which results in a field intensity as illustrated by the red curve. This curve shows that energy is zero within the conductor and that it attains its maximum at the interface between $\rho = 1$ and $\rho = 0$, after which it decays monotonically. In case two, the light grey region corresponds to $\rho = 0.5$ which gives rise to a field intensity as shown by the blue curve. The blue curve display two peaks in the field intensity, i.e. one for the interface between $\rho = 1$ and $\rho = 0.5$, and one for the interface between $\rho = 0.5$ and $\rho = 0$. The consequence of these extra peaks in energy can be seen in figure 6.1(c). This figure illustrates how different values of ρ in the light gray region affects the radiated power. As expected, the figure shows that the objective is larger for $\rho = 0$ than for $\rho = 1$, i.e. the antenna performance is increased when h is reduced. However, the objective function attains its minimum for an intermediate density value. This means that the optimizer has no chance of reducing the height of the monopole, due to the change of sign in the sensitivities. However, the problem can be remedied by applying a density filter. The filter smears out the sharp interfaces and as a result eliminates the existence of multiple intensity peaks. This leads to a smooth and monotonically varying system response as a function of the densities, i.e. the artificial minimum in figure 6.1(c) vanishes.

6.4 Sub-wavelength antenna design

The antenna design problem considered here consists of a hemispherical design domain with radius 0.08 m placed on an PEC groundplane. The target frequency is

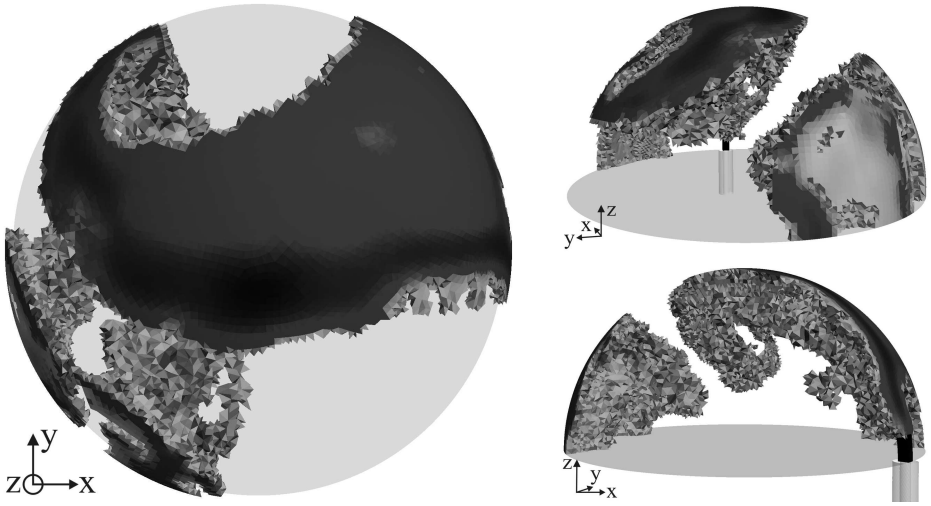

(a) (b)

Figure 6.3 Optimized phase I design visualized such that only elements with $\rho > 0.5$ are shown.

300 MHz and the feed, for the phase II problem, is done using the fundamental TEM mode for a 50 Ohm coaxial cable, see e.g. (Balanis, 2005). The coaxial feed is placed at the outer surface of the spherical design domain. The inner radius of the coaxial cable is $r = 2$ mm and it supplies 1 W of input power. To ensure a good connection between the coaxial feed and the design domain, the inner conductor is extended 1 cm into the design domain. The phase II antenna problem is illustrated in figure 6.2(a). Figure 6.2(b) displays the load cases for the phase I problem, i.e. the directions of the incident waves. The incident waves are all chosen to propagate in the xy-plane plane, since this will minimize the effect of reflections from the PEC groundplane. The choice of design domain dimensions and target frequency leads to a sub-wavelength antenna design problem, i.e. $D/\lambda = 0.16$ where $D = 0.16$ m is the overall length of the design domain and $\lambda \approx 1$ m is the wavelength. The problem is discretized and partioned into 88 parts. This leads to a total of $1.2 \cdot 10^6$ state dofs and $7.2 \cdot 10^5$ design variables for the hemispherical design domain. Each design cycle takes approximately 2.5 minutes.

The phase I problem is solved based on a uniform initial distribution, i.e. $\rho_{\text{init}} = 0.3$, a filter radius of $R_{\min} = 0.01$ m, a volume constraint allowing 60% material and a conductivity of $\sigma^m = 10^6$ S/m. The optimized phase I design after 30 iterations is shown in figure 6.3, and is seen to consist of two large regions of conducting material of which one is completely disconnected from the coaxial cable. A simulation of the phase I optimized design with respect to its radiation efficiency reveals that 0.17 W, i.e. 17 % of the input power, is radiated. Though this is a poorly performing antenna, it does display a small radiation efficiency and should therefore be a good starting point for phase II.

The phase II problem is subject to the same volume constraint as used in phase I, but employs $||\rho^k - \rho^{k-1}||_\infty < 1\%$ as a stopping criteria. The density filter is, however, applied using a continuation approach. The continuation scheme consists of starting the optimization with $R_{\min} = 0.02$ m and then after 50 iterations, or if the optimization converges, to reduce the filter radius according to $R_{\min} = R_{\min}/2$. This is repeated until $R_{\min} < 10^{-3}$ m. At this point the filter radius is kept fixed and the conductivity is increased to $\sigma^m = 5.98 \cdot 10^7$ S/m. The optimization is then continued until the stopping criteria is met. The reason for employing this seemingly complicated continuation scheme for both the density filter and the conductivity, is that numerical experiments have shown that it is hard for the optimizer to determine a design which is resonant at the target frequency. Without the continuation strategy, the deviation between actual resonant frequency for the optimized antenna and the target frequency is seen to be up to 10 %. Note that the filtering is initialized with a radius twice that of the phase I problem. This is done to ensure that the phase I design does not lead directly into a local minimum for the antenna optimization. The phase II optimized design, together with convergence history and its antenna performance, is shown in figure 6.4. The objective at the target frequency, i.e. 300 MHz, is found to be 0.84 W. The convergence plot in figure 6.4(c) shows the effect of the continuation strategy. That is, it shows how each decrease in filter size, or increase in conductivity, leads to a better antenna performance. In [P3] it is shown that the small reductions in objective function at iteration 200 and 250 corresponds to upward shifts in resonant frequency.

The frequency sweep of the optimized design in figure 6.4(d) shows that the resonance peak is located at 308 MHz, for which the radiated power is 0.93 W. The frequency sweep is also performed for a post processed design in which all elements with $\rho > 0.5$ is set to one and all other to zero. The resonance for the post processed design is at 309 MHz with a radiated power in excess of 0.99 W. The 3 % shift in resonant frequency compared to the target frequency is primarily contributed to the size of the design domain. That is, the dimension of the design domain is too small to contain an antenna resonant at 300 MHz. This assumption is confirmed by optimization results based on the same design configuration, but optimized for 280 MHz and 330 MHz, respectively. These optimization problems showed that the 280 MHz example has a deviation of approximately 10 % from the target frequency, while the deviation for the 330 MHz example is less than 0.5 %. It therefore seems as if a small shift in resonance is unavoidable. A similar behavior is observed for the optimized matematerial designs in Diaz and Sigmund (2010).

The optimized design in figure 6.4(a-b) is seen to have a shape similar to that of an planar inverted F-antenna (PIFA), i.e. a shorting strip situated close to the feed point, connected to a larger top-plate (Balanis, 2005). It is also noted that the large disconnected region seen in the phase I design is completely removed by the optimizer. The fractional bandwidth, which is a measure for the operational frequency band for the antenna, is computed to be $FBW_{-10dB} = (318\text{MHz} - 300\text{MHz})/309\text{MHz} = 5.83$ %, which is acceptable for a sub-wavelength antenna.

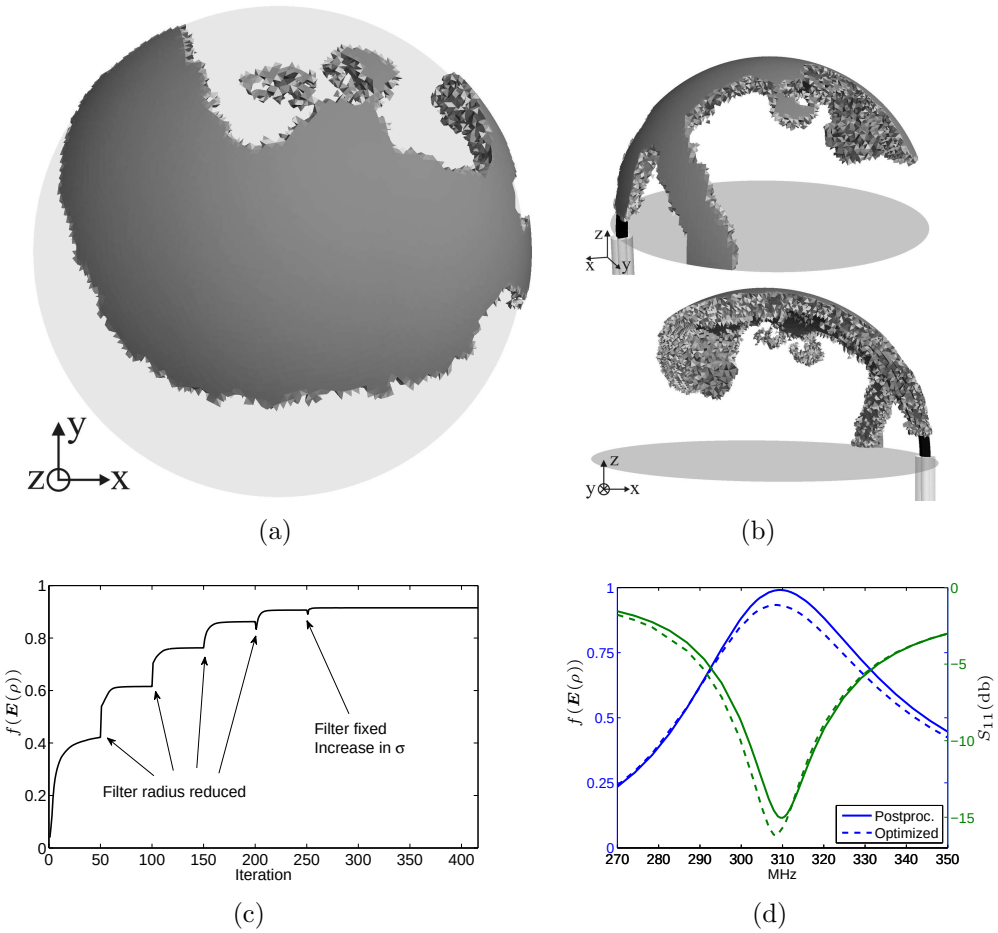

Figure 6.4 (a) and (b) the phase II optimized design visualized using a threshold such that all elements with $\rho > 0.5$ are shown. (a) design seen from the top, and (b) side and front view of the design. (c) the convergence history for the objective function. (d) frequency sweeps of both the optimized design, including intermediate design variables, and a postprocessed design in which all $\rho > 0.5$ are set to 1 and all other to zero. For the optimized design the maximum radiated power is 0.93 W at 308 MHz, and for the post processed design the radiated power is approximately 0.99 W at 309 MHz.

In [P3] the design problem is also solved for the case where the design domain is restricted to the outermost 4 mm of the hemisphere. In this case the objective function is 0.98 W at 305 MHz, i.e. a frequency shift of 1.7 %. That is, the radiated power is lower than for the design in figure 6.4(a-b), while the discrepancy between target and resonant frequency is smaller. It was expected that the full hemispherical design domain would outperform the shell problem, since the shell design domain provides less freedom for the optimizer. This counter-intuitive result is possibly explained by the different surface representation for the two design problems. That is, the shell problem has the possibility to obtain smooth material interfaces at both the outer and inner surfaces of the design domain, while only the outer surface is

smooth for the optimized design in figure 6.4. To investigate if this is the case, a new mesh should be generated for which neither of the two design domains contains smooth surfaces.

The proposed antenna design formalism should also be applied to other antenna design problems to verify that it is generally applicable. Especially conformal design problems are interesting, e.g. antennas mounted on hearing aid casings. To further minimize the observed frequency shift an eigenvalue solver could be applied. The optimization task should be to minimize the difference between the resonant and target frequency, i.e. min $|\omega - \omega^*|$. This, however, requires the implementation of an efficient eigenvalue solver within the parallel framework.

Chapter 7
Wireless energy transfer devices

Wireless transfer of energy over mid- and long-range distances using electromagnetic fields has attracted substantial attention in the recent years (Kurs et al., 2007; Karalis et al., 2008; Peng et al., 2010). Applications where wireless energy transfer could be used to improve the power-supply cover medical implants, hearing aids, smart phones, wireless sensors and other small autonomous electrical devices.

Several methods to transfer energy without a carrier medium have been investigated. One approach is to utilize radiative electromagnetic fields from e.g. an omnidirectional RF antenna. However, such systems display a very low transfer efficiency and can therefore not be used in practise (Liu and Su, 2008). A way to obtain high transfer efficiency over large distances is to use directional antennas or laser systems. Unfortunately these devices require an uninterrupted line-of-sight between transmitter and receiver, which limits their practical use. In Kurs et al. (2007) the authors propose a method for non-radiative efficient mid-range wireless energy transfer based on magnetic induction. The idea is to place two identical magnetic resonators close enough for the near-fields to couple, and thus allow for energy to oscillate back and forth between the resonators. This coupling can be described mathematically by coupled mode theory based on LC circuits (Haus, 1984) if the resonant frequency, losses and coupling coefficient for a single resonator are known. In (Kurs et al., 2007) the method is demonstrated by theory and experiments on two coaxially aligned copper coils for which efficiencies of up to 40% are achieved for $D/l = 0.3$, where D is the coil diameter and l is the distance between transmitter and receiver. Following this publication much effort has been devoted to the practical realization of wireless energy transfer devices. An example is the design by the Intel Cooperation (2008) in which the identical copper coils have been replaced by two complex wire structures with different layout and size for the transmitter and receiver.

In this section an optimization formulation for the design of a receiver for wireless energy transfer is presented. The example problem is based on a simple design presented in Peng et al. (2010) which is used to demonstrate proof of concept.

7.1 The example problem

The design is based on a system of two 6 turn copper coils, each with a of diameter 30 cm and a height of 1 cm. The copper wire has radius 0.5 mm and each of the two coils are connected to a 50 Ohm coaxial cable. The coils are coaxially aligned and separated by a distance of 20 cm. This problem setup is shown in figure 7.1.

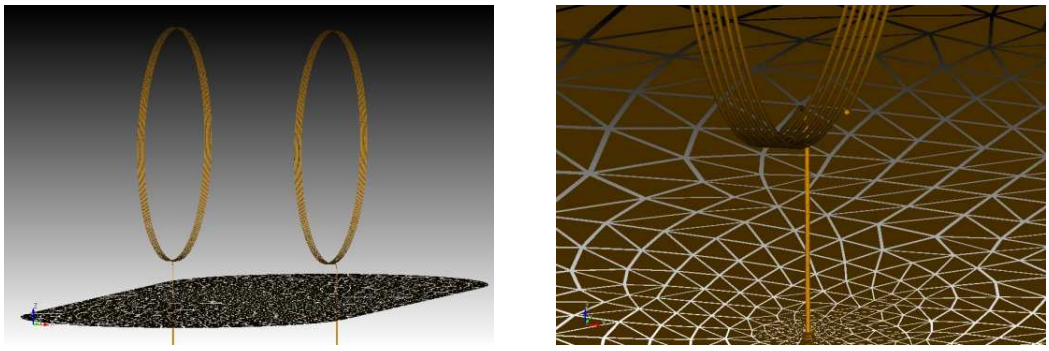

(a) (b)

Figure 7.1 The reference model for wireless energy transfer using resonant copper coils. Each of the two coils consist of 6 turns, a coil diameter of 30 cm, a height of 1 cm. The coils are connected to a 50 Ohm coaxial cable and are coaxially aligned, separated by a distance of 20 cm. (a) both coils and their coaxial ports. (b) zoom of a single coil and its coaxial feed.

To measure the energy transfer efficiency of the problem setup, the ratio between the power transmitted to coil 2 and the power accepted at coil 1 is used. This can be expressed as

$$\eta = \frac{|S_{21}|^2}{1 - |S_{11}|^2} \tag{7.1}$$

where S_{11} is the reflection coefficient for coil 1 and S_{21} is the transmission at coil 2 given by

$$S_{21} = \frac{\int_A \boldsymbol{E} \cdot \bar{\boldsymbol{E}}_0 \mathrm{d}A}{\int_A |\boldsymbol{E}_0|^2 \mathrm{d}A} \tag{7.2}$$

where the integration is performed on the surface that terminates the coaxial cable.

For a single coil the expected resonance can be computed as $\omega = \frac{1}{\sqrt{LC}}$, where L is the self-inductance and and C is the self-capacitance. Using the approximate formulas of Wheeler and Medhurst for the inductance and capacitance, respectively (Balanis, 2005), the expected resonant frequency is found to be $f_0 = 8.5 \pm 0.4$ MHz.

For the model problem, shown in figure 7.1, the copper wire is cut out of the computational domain and replaced by an impedance boundary condition with $\sigma = 5.98 \cdot 10^7$ S/m. The domain is truncated by a first order ABC, which is placed a mere 20 cm from each of the coils. The explanation why this can be done, when the wavelength is 35 m, is that the mode of interest is non-radiative, which means that only the near-field is present and needs to be absorbed. The sufficiency of the truncation model is furthermore verified by numerical experiments. The resulting finite element mesh is partitioned into 144 parts and has a total of 2.7 million edge dofs. A frequency sweep of the reflection, transmission and efficiency for the reference design is shown in figure 7.2. It is seen that two peaks appear in the sweep plots, indicating that the single resonance has been split into two new and slightly shifted resonances. This is exactly as predicted by the coupled mode theory

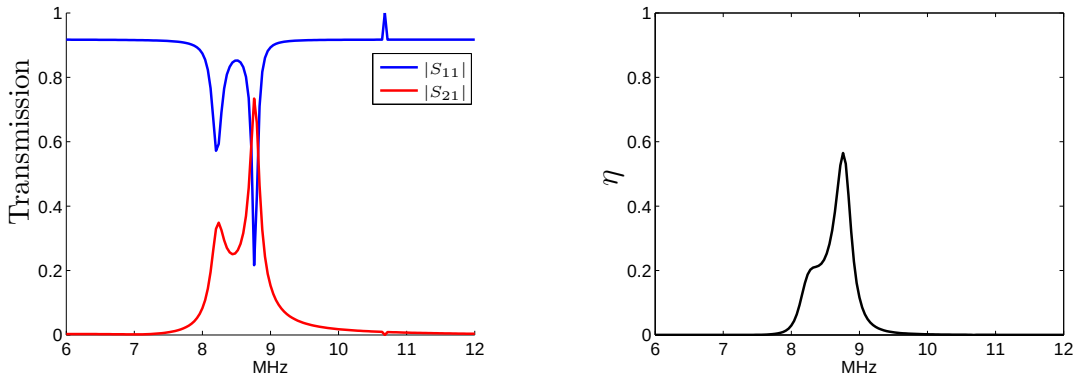

(a) (b)

Figure 7.2 Frequency sweep of the reference design from figure 7.1. (a) the reflection and transmission coefficients, and in (b) the transfer efficiency.

used in Karalis et al. (2008) (see appendix B). Furthermore, it is observed that the resonance is in good agreement with the experimental results from (Peng et al., 2010). On this background is it concluded that the modeling of wireless energy transfer can be adequately performed using the implementation presented here.

7.2 Preliminary optimization results

The optimization problem consists of a simple modification to the wireless energy transfer model from the previous section. The goal is to design the receiver and therefore the receiver coil is cut from the modeling domain and replaced by a design domain with dimensions $2 \times 32 \times 32$ cm, connected to a 50 Ohm coaxial cable. The design problem can be seen in figure 7.3. The number of design variables is $8.6 \cdot 10^5$ and the mesh is again partitioned into 144 parts. The objective is to maximize the power flow at the coaxial port of the receiver, but could just as well be to maximize the S_{21} parameter. The optimization is initialized with $\rho_{\text{init}} = 0.3$ and uses the PDE filter with $R_{\text{min}} = 0.01$ m. Each design cycle requires approximately five minutes to complete.

The optimization process was stopped at iteration 200 with a design change of 5%, i.e. the problem did not converge. The transfer efficiency at this point is 4%, and thus much lower than that of the reference design. However, the poor performance is to be expected due to the coarse mesh used for the optimization. That is, the design domain mesh is far from capable of resolving the coil from the reference design. In fact, resolving the coil would require a fifty-fold refinement in each spatial direction, which is not possible with the current implementation and hardware available. As was observed for e.g. the antenna design problem it could also be that the resonance of the optimized design is shifted away from the target frequency. However, experience has shown that the shift in frequency is small and

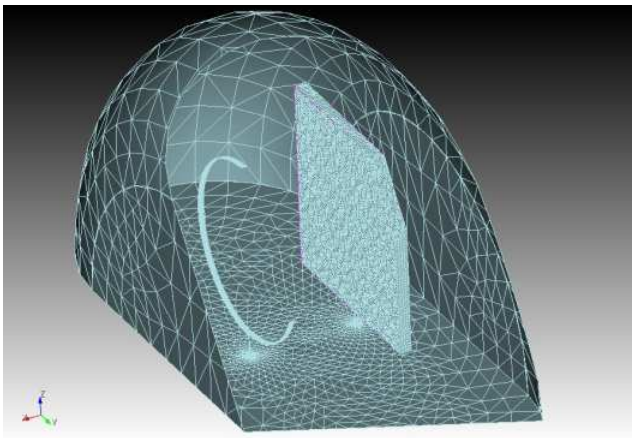

Figure 7.3 Plot of the optimization setup. The design domain can be seen as the rectangular box to the right and has dimension $2 \times 32 \times 32$ cm. The design domain is connected to a 50 Ohm coaxial cable for which the inner conductor is extended 4 cm into the design domain. The objective is to maximize the power flow measured at this coaxial port.

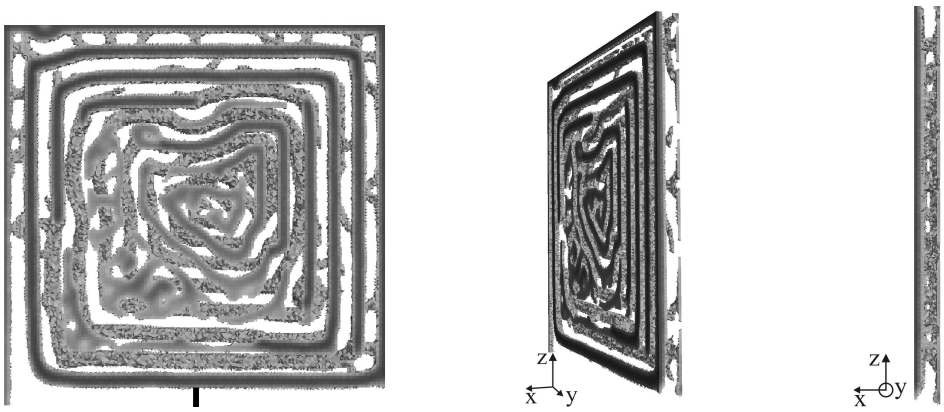

(a) (b) (c)

Figure 7.4 Threshold plots of the optimized design at iteration 200. The threshold is done such that all elements with $\rho > 0.2$ are shown. (a) the front view of the optimized design, (b) tilted side-view and (c) side view.

likewise for the difference in objective. The optimized design can be seen in figure 7.4 and 7.5, and though the performance is not very good, it does reveal several interesting features. From figure 7.4(a), (b) and (c) it is seen that the optimized design consists of two spiral-like structures. This is even more evident from figure 7.5, where the optimized design has been cut into two pieces. It is seen that neither the front, or the back part of the optimized design form complete spirals. However, from a rigorous inspection of figure 7.5(b), in which the blue coloring shows the vias that connect the front and back structures, it is clear that the design is indeed fully connected, i.e. there are no free regions of material floating in air.

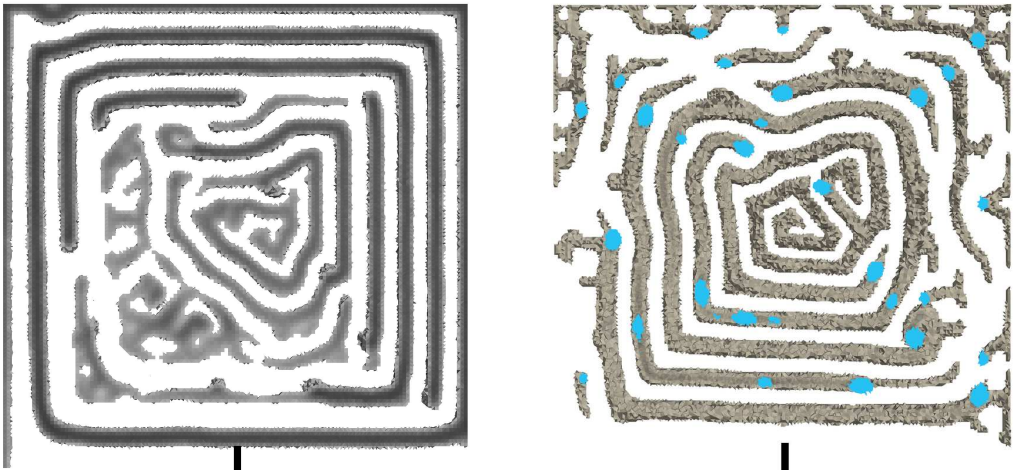

(a) (b)

Figure 7.5 Threshold plots of the optimized design at iteration 200. The threshold is done such that all elements with $\rho > 0.2$ are shown. (a) the front layer of the optimized design is shown and (b) the back layer. The blue color represents vias that connect the front and back structures of the optimized design.

Future work should be directed towards finding a design problem with much smaller dimensions. This would result in a design domain mesh that could be heavily refined, while still allowing for the problem to be solved using the current implementation. A possible test problem is to reduce the diameter of the coils significantly and to add more turns. This problem setting should ensure a good transfer efficiency, and furthermore allow for a fair comparison between reference and optimized design.

Also the design of a transmitter should be investigated. This design problem resembles the antenna design task from the previous chapter, but should also incorporate a requirement for a high quality factor, i.e. that the resonance is underdamped (Karalis et al., 2008). One way to achieve this could be to implement Padé approximations (Jin, 2002), which allow for a numerically efficient way to compute a frequency sweep. Based on this frequency sweep the objective would be to maximize the ratio between the magnitude at the target frequency and e.g. the half-power bandwidth.

Another direction for future work is motivated by the frequency splitting observed when coupling two identical resonators by their near fields. For the problem considered here, both the layout of the transmitter and the target frequency is fixed. From coupled mode theory it is evident that changes in the resonance of the receiver will affect the resonances of the coupled system. Therefore a design scheme could be to keep the layout of the transmitter fixed, while allowing the target frequency to change during the optimization process based on the results of a frequency sweep.

Chapter 8
Concluding remarks

The work presented in this Ph.D. thesis is an extension of the topology optimization method to several new electromagnetic wave problems concerning the free distribution of conducting material.

A design parameterization is proposed which incorporates the skin effect and thus allows the optimization to be performed on finite element meshes that do not resolve skin depth. This is accomplished by the imposition of an impedance boundary condition on element level.

The design formalism and the finite element representation of the wave problem is implemented in Matlab for 2D problems, and a parallel C++ framework for 3D problems. The C++ framework also includes a parallelized implementation of the popular MMA algorithm.

The optimization setting is first used to design electric and magnetic focusing devices, including Fresnel plate zone lenses. It is found that the optimized designs guides and focuses the electromagnetic energy into the desired objective regions.

The second type of optimization problem investigated concerns antenna design. To obtain a design methodology that is independent of the choice of initial design, a two phase optimization procedure is proposed. Phase I consists of solving an incomplete inverse antenna problem and phase II is the actually antenna optimization problem. It is shown by numerical experiments that this optimization procedure can be used to design highly efficient sub-wavelength antennas. However, for both the energy focusing devices and the antenna problem it is seen that the optimized design is not always resonant exactly at the target frequency. This is even more evident when performing a post analysis on designs that are rendered completely binary. In this case the shift can partly be explained by the intermediate design variables, which add more damping to the system and thus results in a lower resonant frequency than for the post processed design.

The last optimization problem considered is the design of a receiver for wireless energy transfer. It was first demonstrated that the current 3D implementation is capable of modeling the physics of wireless energy transfer, but it also revealed its limitation with respect to problem size. Though the reference design was not outperformed, the example still showed the potential of topology optimization applied to wireless energy transfer problems.

8.1 Future work

The list of interesting ideas for future work is seemingly endless. The list below contains the most important directions in which any future research should be directed

towards:

- The development of an efficient iterative solver such that problems with 100 million of dofs can be optimized. Ideas for such solvers include:
  a. Multigrid preconditioned GMRES/BiCGSTAB-L.
  b. Higher order edge elements and Least-Square FEM.
  c. FETI approach to decoupling of the partitions.
- Extend the MMA implementation to also cover the globally convergent version.
- Apply the antenna optimization formalism to new design problems such as patch antennas, microstrip filters and conformal antennas for e.g. hearing aids or cellular phones.
- Extend the implementation to include Padé approximation such that the devices can be optimized over large frequency ranges.
- Examine other wireless energy transfer problems with small overall dimensions to allow for fine meshing of the design domain.
- Further investigations into the frequency shift observed in many of the presented optimization results.
- Implement shape optimization and apply it to the topology optimized designs.

References

Altshuler, E. (2002). Electrically small self-resonant wire antennas optimized using a genetic algorithm. *IEEE Transactions on Antennas and Propagation*, 50(3):297–300.

Amdahl, G. (1967). Validity of the single processor approach to achieving large-scale computing capabilities. In *AFIPS Conference Proceedings*, volume 30, pages 483–485.

Amestoy, P. R., Duff, I. S., and L'Excellent, J. Y. (2000). Multifrontal parallel distributed symmetric and unsymmetric solvers. *Computer Methods in Applied Mechanics and Engineering*, 184(2-4):501–520.

Andkjær, J., Nishiwaki, S., Nomura, T., and Sigmund, O. (2010). Topology optimization of grating couplers for the efficient excitation of surface plasmons. *J. Opt. Soc. Am. B*, 27(9):1828–1832.

Andréasson, N., Evgrafov, A., and Patriksson, M. (2005). *An Introduction to Continuous Optimization*. Studentlitteratur, Lund, Sweden.

Assadihaghi, A., Bila, S., Baillargeat, D., Aubourg, M., Verdeyme, S., Boichon, C., Puech, J., and Lapierre, L. (2008). Optimization of microwave devices combining topology gradient and genetic algorithm. *Int J RF and Microwave Comp Aid Eng*, 18(5):454–463.

Balanis, C. (1989). *Advanced Engineering Electromagnetics*. John Wiley & Sons Inc., 1st edition.

Balanis, C. (2005). *Antenna Theory: Analysis and Design*. Wiley-Interscience, 3rd edition.

Bayraktar, Z., Werner, P., and Werner, D. (2006). The design of miniature three-element stochastic yagi-uda arrays using particle swarm optimization. *IEEE Antennas and Wireless Propagation Letters*, 5(1):22–26.

Bendsøe, M. (1989). Optimal shape design as a material distribution problem. *Structural Optimization*, 1:193–202.

Bendsøe, M. and Kikuchi, N. (1988). Generating optimal topologies in structural design using a homogenization method. *Computer Methods in Applied Mechanics and Engineering*, 71:197–224.

Bendsøe, M. and Sigmund, O. (2004). *Topology Optimization; Theory, Methods and Applications*. Springer Verlag Berlin Heidelberg New York, 2nd edition.

Borel, P. I., Frandsen, L. H., Harpoth, A., Kristensen, M., Jensen, J. S., and Sigmund, O. (2005). Topology optimised broadband photonic crystal y-splitter. *Electronics Letters*, 41(2):69–71.

Bourdin, B. (2001). Filters in topology optimization. *Int. J. Numer. Meth. Engng.*, 50(9):2143–2158.

Bruns, T. E. and Tortorelli, D. A. (2001). Topology optimization of non-linear elastic structures and compliant mechanisms. *Computer Methods in Applied Mechanics and Engineering*, 190(26-27):3443–3459.

Cox, S. J. and Dobson, D. C. (1999). Maximizing band gaps in two-dimensional photonic crystals. *Siam Journal On Applied Mathematics*, 59(6):2108–2120.

Dühring, M. B., Jensen, J. S., and Sigmund, O. (2008). Acoustic design by topology optimization. *Journal of Sound and Vibration*, 317(3-5):557 – 575.

Diaz, A. and Sigmund, O. (2010). A topology optimization method for design of negative permeability metamaterials. *Structural and Multidisciplinary Optimization*, 41:163–177.

Erentok, A. and Sigmund, O. (2011). Topology optimization of sub-wavelength antennas. *IEEE Transactions on Antennas and Propagation*, 59(1):58–69.

Gabriel, E., Fagg, G. E., Bosilca, G., Angskun, T., Dongarra, J. J., Squyres, J. M., Sahay, V., Kambadur, P., Barrett, B., Lumsdaine, A., Castain, R. H., Daniel, D. J., Graham, R. L., and Woodall, T. S. (2004). Open MPI: Goals, concept, and design of a next generation MPI implementation. In *Proceedings, 11th European PVM/MPI Users' Group Meeting*, pages 97–104, Budapest, Hungary.

Galehdar, A., Thiel, D., and O'Keefe, S. (2009). Design methods for 3d rfid antennas located on a conducting ground plane. *IEEE Transactions on Antennas and Propagation*, 57(2):339–346.

Geuzaine, C. and Remacle, J.-F. (2009). *International Journal for Numerical Methods in Engineering*, 79:1309–1331.

Guest, J. K., Prevost, J. H., and Belytschko, T. (2004). Achieving minimum length scale in topology optimization using nodal design variables and projection functions. *International Journal For Numerical Methods In Engineering*, 61(2):238–254.

Halkjær, S., Sigmund, O., and Jensen, J. (2006). Maximizing band gaps in plate structures. *Structural and Multidisciplinary Optimization*, 32:263–275.

Haus, H. A. (1984). *Waves and fields in optoelectronics*. Prentice-Hall.

Hoorfar, A. (2007). Evolutionary programming in electromagnetic optimization: A review. *IEEE Transactions on Antennas and Propagation*, 55(3):523–537.

Hristov, H. and Herben, M. (1995). Millimeter-wave fresnel-zone plate lens and antenna. *IEEE Transactions on Microwave Theory and Techniques*, 43(12):2779–2785.

Intel Cooperation (2008). Wireless energy transfer. Available from `http://dvice.com/archives/2008/08/intel_wireless.php`.

Jensen, J. and Sigmund, O. (2011). Topology optimization for nano-photonics. *Laser & Photon. Rev.*, 5(2):308–321.

Jensen, J. S. (2009). Space-time topology optimization for one-dimensional wave propagation. *Computer Methods in Applied Mechanics and Engineering*, 198(5-8):705 – 715.

Jensen, J. S. and Sigmund, O. (2004). Systematic design of photonic crystal structures using topology optimization: Low-loss waveguide bends. *Applied Physics Letters*, 84(12):2022–2024.

Jensen, J. S. and Sigmund, O. (2005). Topology optimization of photonic crystal structures: a high-bandwidth low-loss t-junction waveguide. *Journal Of The Optical Society Of America B-Optical Physics*, 22(6):1191–1198.

Jin, J. (2002). *The Finite Element Method in Electromagnetics*. John Wiley & Sons, second edition.

Jin, J. and Riley, D. (2009). *Finite Element Analysis of Antennas and Arrays*. John Wiley & Sons, first edition.

Karalis, A., Joannopoulos, J., and Soljacic, M. (2008). Efficient wireless non-radiative mid-range energy transfer. *Annals of Physics*, 323(1):34–48.

Karypis, G. and Kumar, V. (1999). A fast and high quality multilevel scheme for partitioning irregular graphs. *SIAM Journal on Scientific Computing*, 20(1):359 – 392.

Kawamoto, A., Matsumori, T., Yamasaki, S., Nomura, T., Kondoh, T., and Nishiwaki, S. (2010). Heaviside projection based topology optimization by a pde-filtered scalar function. *Structural and Multidisciplinary Optimization*, pages 1–6.

Kiziltas, G. (2003). *Dielectric material optimization of filters and antennas using SIMP*. PhD thesis, Dept. Mech. Eng. Univ. Michigan Ann Arbor.

Kiziltas, G., Kikuchi, N., Volakis, J. L., and Halloran, J. (2004). Topology optimization of dielectric substrates for filters and antennas using simp. *Archives Of Computational Methods In Engineering*, 11(4):355–388.

Kiziltas, G., Psychoudakis, D., Volakis, J. L., and Kikuchi, N. (2003). Topology design optimization of dielectric substrates for bandwidth improvement of a patch antenna. *IEEE Transactions On Antennas And Propagation*, 51(10):2732–2743.

Koulouridis, S., Psychoudakis, D., and Volakis, J. L. (2007). Multiobjective optimal antenna design based on volumetric material optimization. *IEEE Transactions On Antennas And Propagation*, 55(3):594–603.

Kurs, A., Karalis, A., Moffatt, R., Joannopoulos, J. D., Fisher, P., and Soljacic, M. (2007). Wireless power transfer via strongly coupled magnetic resonances. *Science*, 317(5834):83–86.

Larsen, A., Laksafoss, B., Jensen, J., and Sigmund, O. (2009). Topological material layout in plates for vibration suppression and wave propagation control. *Structural and Multidisciplinary Optimization*, 37:585–594.

Lazarov, B. and Augarde, C. (2005). Object oriented design of parallel and sequential finite element codes. In *Proceedings of 25 the 13th ACME Conference*.

Lazarov, B. S. and Sigmund, O. (2010). Filters in topology optimization based on helmholtz-type differential equations. *Int. J. Numer. Meth. Engng.*

Li, Z., Erdemli, Y., Volakis, J., and Papalambros, P. (2002). Design optimization of conformal antennas by integrating stochastic algorithms with the hybrid finite-element method. *IEEE Transactions on Antennas and Propagation*, 50(5):676–684.

Li, Z., Papalambros, P., and Volakis, J. (1997). Designing broad-band patch antennas using the sequential quadratic programming method. *IEEE Transactions on Antennas and Propagation*, 45(11):1689–1692.

Lim, S. and Ling, H. (2007). Design of electrically small yagi antenna. *Electronics Letters*, 43(5):3–4.

Liu, Y. and Su, C. (2008). Wideband omnidirectional operation monopole antenna. *Progress in Electromagnetic Research Leetter*, 1:255–261.

Matzen, R., Jensen, J. S., and Sigmund, O. (2010). Topology optimization for transient response of photonic crystal structures. *J. Opt. Soc. Am. B*, 27:2040–2050.

Maxwell, J. C. (1865). A dynamical theory of the electromagnetic field. *Philisophical Transactions of the Royal Society of London*, 155:459–512.

Maxwell, J. C. (1873). *A treatise on Electricity and Magnetism*. Oxford: Clarendon Press.

Michaleris, P., Tortorelli, D. A., and Vidal, C. A. (1994). Tangent operators and design sensitivity formulations for transient non-linear coupled problems with applications to elastoplasticity. *Int. J. Numer. Meth. Engng.*, 37(14):2471–2499.

Minin, O. V. and Minin, I. V. (2004). *Diffractional optics of millimetre waves*. Institute of Physics Publishing Bristol and Philadelphia.

Mittra, R. (2007). Challenges in antenna designs and some novel techniques for meeting them. In *Antennas and Propagation Conference, 2007. LAPC 2007. Loughborough*, pages 1–4.

Nedelec, J. C. (1980). Mixed finite elements in $\mathbb{R}^3$. *Numerische Mathematik*, 35:315–341.

Niu, B., Olhoff, N., Lund, E., and Cheng, G. D. (2010). Discrete material optimization of vibrating laminated composite plates for minimum sound radiation. *International Journal Of Solids And Structures*, 47(16):2097–2114.

Nomura, T., Sato, K., Taguchi, K., Kashiwa, T., and Nishiwaki, S. (2007). Structural topology optimization for the design of broadband dielectric resonator antennas using the finite difference time domain technique. *Int. J. Numer. Meth. Engng.*, 71(11):1261–1296.

Peng, L., Breinbjerg, O., and Mortensen, N. (2010). Wireless energy transfer through non-resonant magnetic coupling. *Journal of Electromagnetic Waves and Applications*, 24:1587–1598(12).

Robinson, J. and Rahmat-Samii, Y. (2004). Particle swarm optimization in electromagnetics. *IEEE Transactions on Antennas and Propagation*, 52(2):397–407.

Saad, Y. (2000). *Iterative methods for sparse linear systems*. SIAM, 2nd edition.

Sigmund, O. (2007). Morphology-based black and white filters for topology optimization. *Structural And Multidisciplinary Optimization*, 33(4-5):401–424.

Sigmund, O. (2011). On the usefulness of non-gradient approaches in topology optimization. *Structural and Multidisciplinary Optimization*. Published online: 31 March 2011.

Sigmund, O. and Hougaard, K. (2008). Geometric properties of optimal photonic crystals. *Physical Review Letters*, 100(15):1–4.

Sigmund, O. and Jensen, J. (2003). Systematic design of phononic band-gap materials and structures using topology optimization. *Phil. Trans. R. Soc. London*, 361:1001–1019.

Svanberg, K. (1987). The method of moving asymptotes - a new method for structural optimization. *International Journal for Numerical Methods in Engineering*, 25.

Thomas, H., Zhou, M., and Schramm, U. (2002). Issues of commercial optimization software development. *Structural and Multidisciplinary Optimization*, 23:97–110.

Thompson, A. and Vaughan, D. (2009). X-ray data booklet. Online: Lawrence Berkeley National Laboratory.

Thomsen, J. J. (2003). *Vibrations and Stability: Advanced theory, analysis and tools*. Springer Verlag Berlin Heidelberg, 2nd edition.

Wadbro, E. and Berggren, M. (2006). Topology optimization of an acoustic horn. *Computer Methods in Applied Mechanics and Engineering*, 196(1-3):420 – 436.

Wang, F., Jensen, J. S., and Sigmund, O. (2011). Robust topology optimization of photonic crystal waveguides with tailored dispersion properties. *J. Opt. Soc. Am. B*, 28:387–397.

Weile, D. and Michielssen, E. (1997). Genetic algorithm optimization applied to electromagnetics: a review. *IEEE Transactions on Antennas and Propagation*, 45(3):343–353.

Xie, Y. and Steven, G. (1993). A simple evolutionary procedure for structural optimization. *Computers & Structures*, 49(5):885–896.

Yoon, G. H., Jensen, J. S., and Sigmund, O. (2007). Topology optimization of acoustic-structure interaction problems using a mixed finite element formulation. *International Journal For Numerical Methods In Engineering*, 70(9):1049–1075.

Zaglmayr, S. (2006). *High Order Finite Element Methods for Electromagnetic Field Computation*. PhD thesis, Johannes Keppler University (Austria).

Zaharis, Z. D. (2008). Boolean particle swarm optimization of 3-branch gsm/dcs/umts current dividers by using artificial immune system. *IEICE Electron. Express*, 5:41–47.

Zhou, S., Li, W., and Li, Q. (2010a). Level-set based topology optimization for electromagnetic dipole antenna design. *Journal of Computational Physics*, 229(19):6915–6930.

Zhou, S., Li, W., Sun, G., and Li, Q. (2010b). A level-set procedure for the design of electromagnetic metamaterials. *Opt. Express*, 18:6693–6702.

Zhu, Y. and Cangellaris, A. (2006). *Multigrid Finite Element Methods for Electromagnetic Field Modeling*. John Wiley & Sons, first edition.

Zienkiewicz, O. C. and Taylor, R. L. (2000). *Finite Element Method: (parts 1-3)*. Butterworth-Heinemann, fifth edition.

Appendix A
Sensitivity derivation

This appendix contains the derivation of the adjoint sensitivity method for complex function with real input. The idea is to formulate the input to the real valued function in terms real and imaginary parts, i.e. $\boldsymbol{u} = \boldsymbol{u}_R + j\boldsymbol{u}_I$. The function and the state problem residual may then be written as

$$\begin{aligned} f &= f(\rho, \boldsymbol{u}_R, \boldsymbol{u}_I) \\ \boldsymbol{R} &= \boldsymbol{S}(\rho)\boldsymbol{u} - \boldsymbol{b}\ (= 0) \end{aligned}$$

where $\boldsymbol{S}(\rho)$, $\boldsymbol{u}$ and $\boldsymbol{b}$ are complex quantities. The adjoint sensitivity analysis then follows by adding the residual, i.e. zero, to the objective and by the introduction of a Lagrange multiplier. Due to the complex problem both the residual and its complex transpose is added to form the following augmented Lagrangian

$$L = f + \boldsymbol{\lambda}_1^T(\boldsymbol{S}\boldsymbol{u} - \boldsymbol{b}) + \boldsymbol{\lambda}_2^T(\bar{\boldsymbol{S}}\bar{\boldsymbol{u}} - \bar{\boldsymbol{b}}) \tag{A.1}$$

where $\bar{(\cdot)}$ refers to complex conjugate, $(\cdot)^T$ to the real transpose and $\boldsymbol{\lambda}_1$ and $\boldsymbol{\lambda}_2$ are Lagrange multipliers. Using the chain-rule the derivative with respect to ρ^e becomes

$$\begin{aligned} \frac{\mathrm{d}L}{\mathrm{d}\rho^e} = &\frac{\partial f}{\partial \rho^e} + \frac{\partial f}{\partial \boldsymbol{u}_R}\frac{\partial \boldsymbol{u}_R}{\partial \rho^e} + \frac{\partial f}{\partial \boldsymbol{u}_I}\frac{\partial \boldsymbol{u}_I}{\partial \rho^e} \\ &+ \boldsymbol{\lambda}_1^T\left(\frac{\partial \boldsymbol{S}}{\partial \rho^e}\boldsymbol{u}_R + \boldsymbol{S}\frac{\partial \boldsymbol{u}_R}{\partial \rho^e} + j\frac{\partial \boldsymbol{S}}{\partial \rho^e}\boldsymbol{u}_I + j\boldsymbol{S}\frac{\partial \boldsymbol{u}_I}{\partial \rho^e} - \frac{\partial \boldsymbol{f}}{\partial \rho^e}\right) \\ &+ \boldsymbol{\lambda}_2^T\left(\frac{\partial \bar{\boldsymbol{S}}}{\partial \rho^e}\boldsymbol{u}_R + \bar{\boldsymbol{S}}\frac{\partial \boldsymbol{u}_R}{\partial \rho^e} - j\frac{\partial \bar{\boldsymbol{S}}}{\partial \rho^e}\boldsymbol{u}_I - j\bar{\boldsymbol{S}}\frac{\partial \boldsymbol{u}_I}{\partial \rho^e} - \frac{\partial \bar{\boldsymbol{b}}}{\partial \rho^e}\right) \end{aligned}$$

where j is the imaginary unit. Rearranging this equation lead to the following result

$$\begin{aligned} \frac{\mathrm{d}L}{\mathrm{d}\rho^e} = &\frac{\partial f}{\partial \rho^e} + \boldsymbol{\lambda}_1^T\left(\frac{\partial \boldsymbol{S}}{\partial \rho^e}\boldsymbol{u} - \frac{\partial \boldsymbol{b}}{\partial \rho^e}\right) + \boldsymbol{\lambda}_2^T\left(\frac{\partial \bar{\boldsymbol{S}}}{\partial \rho^e}\boldsymbol{u} - \frac{\partial \bar{\boldsymbol{b}}}{\partial \rho^e}\right) \\ &+ \left(\frac{\partial f}{\partial \boldsymbol{u}_R} + \boldsymbol{\lambda}_2^T\boldsymbol{S} + \boldsymbol{\lambda}_1^T\bar{\boldsymbol{S}}\right)\frac{\partial \boldsymbol{u}_R}{\partial \rho^e} + \left(\frac{\partial f}{\partial \boldsymbol{u}_I} + j\boldsymbol{\lambda}_1^T\boldsymbol{S} - j\boldsymbol{\lambda}_2^T\bar{\boldsymbol{S}}\right)\frac{\partial \boldsymbol{u}_I}{\partial \rho^e} \end{aligned}$$

In order to get rid of the terms involving $\frac{\partial \boldsymbol{u}_R}{\partial \rho^e}$ and $\frac{\partial \boldsymbol{u}_I}{\partial \rho^e}$, the following equations must hold

$$\boldsymbol{\lambda}_1^T\boldsymbol{S} + \boldsymbol{\lambda}_2^T\bar{\boldsymbol{S}} = -\frac{\partial f}{\partial \boldsymbol{u}_R} \tag{A.2}$$

$$j\boldsymbol{\lambda}_1^T\boldsymbol{S} - j\boldsymbol{\lambda}_2^T\bar{\boldsymbol{S}} = -\frac{\partial f}{\partial \boldsymbol{u}_I} \tag{A.3}$$

Multiplying eq. (A.3) by j and subtracting it from (A.2) yields

$$2\boldsymbol{\lambda}_1^T \boldsymbol{S} = -\frac{\partial f}{\partial \boldsymbol{u}_R} + j\frac{\partial f}{\partial \boldsymbol{u}_I} \tag{A.4}$$

and by transposing the former equation one obtains

$$\boldsymbol{S}^T \boldsymbol{\lambda}_1 = -\frac{1}{2}\left(\frac{\partial f}{\partial \boldsymbol{u}_R} - j\frac{\partial f}{\partial \boldsymbol{u}_I}\right)^T \tag{A.5}$$

If instead eq. (A.3) is multiplied by j and added to eq. (A.2) one obtains

$$2\boldsymbol{\lambda}_2^T \bar{\boldsymbol{S}} = -\frac{\partial f}{\partial \boldsymbol{u}_R} - j\frac{\partial f}{\partial \boldsymbol{u}_I} \tag{A.6}$$

Taking the complex conjugate of eq. (A.6) and comparing to the result in eq. (A.4) it is seen that $\boldsymbol{\lambda}_1 = \bar{\boldsymbol{\lambda}}_2$. Denoting $\boldsymbol{\lambda} = \boldsymbol{\lambda}_1$ the final expression becomes

$$\frac{\mathrm{d}L}{\mathrm{d}\rho^e} = \frac{\partial f}{\partial \rho^e} + \boldsymbol{\lambda}^T\left[\frac{\partial \boldsymbol{S}}{\partial \rho^e}\boldsymbol{u} - \frac{\partial \boldsymbol{b}}{\partial \rho^e}\right] + \bar{\boldsymbol{\lambda}}^T\left[\frac{\partial \bar{\boldsymbol{S}}}{\partial \rho^e}\bar{\boldsymbol{u}} - \frac{\partial \bar{\boldsymbol{b}}}{\partial \rho^e}\right]$$

Which can be stated more simply as

$$\frac{\mathrm{d}f}{\mathrm{d}\rho^e} = \frac{\mathrm{d}L}{\mathrm{d}\rho^e} = \frac{\partial f}{\partial \rho^e} + 2\mathbb{R}\left(\boldsymbol{\lambda}^T\left[\frac{\partial \boldsymbol{S}}{\partial \rho^e}\boldsymbol{u} - \frac{\partial \boldsymbol{b}}{\partial \rho^e}\right]\right) \tag{A.7}$$

where $\boldsymbol{\lambda}$ is the solution to

$$\boldsymbol{S}^T \boldsymbol{\lambda} = -\frac{1}{2}\left(\frac{\partial f}{\partial \boldsymbol{u}_R} - j\frac{\partial f}{\partial \boldsymbol{u}_I}\right)^T \tag{A.8}$$

The linear system in equation (A.8) is called the adjoint problem.

Appendix B
Coupled mode theory and wireless energy transfer

This appendix contains a brief introduction to the Coupled Mode Theory (CMT) mentioned in chapter 7, and is only intended to provide the reader with a basic knowledge of CMT which is very useful for studying publications on wireless energy transfer.

CMT is an idealized representation of the coupling between resonant modes, valid in cases where the exchange of energy is assumed to be slow compared to the frequency. It was proposed by Haus (1984) and for wireless energy transfer analysis its application is based on LC-circuit theory. The same theory can however be applied to systems in optics, mechanics and quantum mechanics to name but a few. The CMT formalism introduced in (Haus, 1984) is used, or mentioned, in virtually all publications on wireless energy transfer published to this date. The formalism is based on decomposing the 2nd order ordinary differential equation (ODE) that arise when analyzing e.g. a mass/spring system or a LC-circuit. Using complex variables the 2nd order ODE is described in terms of two decoupled 1st order ODEs with complex parameters. To exemplify the approach a simple mass/spring harmonic oscillator is considered, i.e.

$$m\ddot{x} + kx = 0 \tag{B.1}$$

where $\dot{()}$ refers to the derivative with respect to time. This equation can be stated as a first order system, i.e.

$$v = m\dot{x} \tag{B.2}$$

$$x = -\frac{1}{k}\dot{v} \tag{B.3}$$

The idea of CMT is the to define the two complex variables

$$a_{\pm} = \sqrt{\frac{1}{2k}}\left(v \pm j\sqrt{mk}x\right) \tag{B.4}$$

where j is the imaginary unit. By a series of manipulations the equations (B.2) and (B.3) can be expressed as

$$\dot{a}_{+} = j\omega a_{+} \tag{B.5}$$

$$\dot{a}_{-} = -j\omega a_{-} \tag{B.6}$$

which are completely decoupled first order ODEs and $\omega = \sqrt{\frac{k}{m}}$ is seen to be the resonant frequency for the mass/spring system. The amplitudes a_{+} and a_{-} refers to

positive and negative frequency components, respectively. The consequence of this decomposition is that only one of the two equations in equations (B.5) and (B.6) needs to be solved.

Next, the case of two coupled resonators is briefly described. The resonators are assumed be lossy, and using CMT the coupled system becomes as follows

$$\begin{aligned} \dot{a}_1 &= (j\omega_1 - \Gamma_1)\, a_1 + \kappa a_2 \\ \dot{a}_2 &= (j\omega_2 - \Gamma_2)\, a_2 + \kappa a_1 \end{aligned} \tag{B.7}$$

where a_i, ω_i and Γ_i are the amplitude, resonant frequency and damping parameter of resonators i. The coupling coefficient κ is assumed to be much smaller than the resonant frequencies. In case of an LC-circuit the resonant frequency of each of the oscillators can be computed as $\omega_i = \frac{1}{\sqrt{L_i C_i}}$, where L_i is the inductance and C_i the capacitance (Balanis, 1989). The damping coefficient consists of the sum of Ohmic, radiative, etc. losses present in the circuit. The coupling coefficient naturally depends on the ways the system is coupled, and with respect to wireless energy transfer this is a parameter that should be maximized.

In the case of two identical circuits, e.g. two identical copper coils, we have that $\omega = \omega_1 = \omega_2$ and $\Gamma = \Gamma_1 = \Gamma_2$. Assuming a time-harmonic time dependence, i.e. $a_i = a_i e^{j\Omega t}$, trivial manipulations of equation (B.7) leads to the following expression for Ω

$$\Omega = \omega + j\Gamma \pm \kappa \tag{B.8}$$

From this result it is clear that the normal modes of the combined system are split by 2κ. It is exactly this splitting phenomena that was observed in figure 7.2. When damping is very low or when $\kappa \gg \Gamma$ this means that energy will oscillate back and forth between the two modes, practically without any loss. This means that a good resonator for wireless energy transfer should exhibit extremely low damping, i.e. a high quality factor.

Publication [P1]

Topology optimization of metallic devices for microwave applications

INTERNATIONAL JOURNAL FOR NUMERICAL METHODS IN ENGINEERING
Int. J. Numer. Meth. Engng 2010; **83**:228–248
Published online 9 March 2010 in Wiley InterScience (www.interscience.wiley.com). DOI: 10.1002/nme.2837

Topology optimization of metallic devices for microwave applications

N. Aage[1,2,*,†], N. A. Mortensen[2] and O. Sigmund[1]

[1]*Department of Mechanical Engineering, Solid Mechanics, Technical University of Denmark, DK-2800 Kgs. Lyngby, Denmark*
[2]*Department of Photonic Engineering, Technical University of Denmark, DK-2800 Kgs. Lyngby, Denmark*

SUMMARY

In electromagnetic optimization problems of metallic radio-frequency devices, such as antennas and resonators for wireless energy transfer, the volumetric distribution of good conductors, e.g. copper, has been known to cause numerical bottlenecks. In finite element analysis the limiting factor is the skin depth, which calls for highly refined meshing in order to capture the physics. The skin depth problem has therefore prohibited the application of topology optimization to this class of problem. We present a design parameterization that remedies these numerical issues, by the interpolation of Maxwell's equations and a fictitious element impedance condition. The validity of the proposed design parameterization is confirmed by several numerical examples. Copyright © 2010 John Wiley & Sons, Ltd.

Received 4 May 2009; Revised 28 August 2009; Accepted 27 November 2009

KEY WORDS: topology optimization; finite elements; electromagnetics; microwaves; antenna design

1. INTRODUCTION

The motivation for this work originates from the ever increasing usage of small hand-held, or autonomous, electrical devices. Examples of such devices include hearing aids, medical implants and communication applications. Since more and more functionality is incorporated into these devices, issues regarding power supply has become a challenging design problem. The solution to the power supply problem took a new turn in 2007, where Soljacic and co-workers demonstrated that one can obtain efficient mid-range wireless energy transfer (WiTricity) using magnetically

*Correspondence to: N. Aage, Department of Mechanical Engineering, Solid Mechanics, Technical University of Denmark, DK-2800 Kgs. Lyngby, Denmark.
†E-mail: naa@mek.dtu.dk

Contract/grant sponsor: Danish National Advanced Technology Foundation
Contract/grant sponsor: Eurohorcs/ESF European Young Investigator Award
Contract/grant sponsor: Danish Center for Scientific Computing

resonant-coupled copper coils [1]. Since the publication of their work, improved designs have been proposed [2] and products based on the same theory have been demonstrated for use with city trams [3]. Common for the designs are that they consist of an elaborate spatial distribution of a good conductor, e.g. copper, in a dielectric background, e.g. air.

Another important design challenge associated with small electrical devices arises from the need for wireless communication. Owing to the small dimensions of these devices (compared with the wavelength of the radiation), standard antennas are no longer sufficient and the antenna system must in many cases be designed specifically for the application. A typical antenna is a metallic device with the signal being fed by a transmission line [4]. The antenna design problem can, therefore, also be reduced to determining the best distribution of a good conductor in a dielectric background.

Thus, both the design of antennas and the design of transmitters/receivers for WiTricity consist of determining an optimal distribution of metal and dielectric within the available design space. This makes the design problems obvious candidates for the topology optimization method [5]. The aim of the work presented in this paper is the development of an efficient and robust method for the design of metallic/dielectric microwave (i.e. 3 Hz to 300 GHz) devices using gradient-based topology optimization.

1.1. Topology optimization

Topology optimization is a numerical optimization method for finding optimized material distributions within a given design domain, such that a desired response of the system is optimized. The method was originally developed for the design of elastic structures, where the stiffness was to be maximized subject to a constraint on the structure's weight [5, 6]. Topology optimization has since then been proven to be a very successful design tool for general mechanical problems, both in academia and industry [5]. The method has also been applied to electromagnetic problems involving distribution of dielectric materials, e.g. dielectric loading of antennas [7] and photonic crystals [8, 9], with great success. The big advantage of topology optimization over other optimization techniques is that the structure's connectivity is not prescribed *a priori* and is allowed to evolve during the optimization process. This freedom is obtained by associating each volume element (3D) in the discretized design domain with a continuous variable, $0 \leqslant \rho^e \leqslant 1$, and to use this for interpolating between candidate materials. The design variable can be understood as the material density of one of the two material candidates. Since the method is iterative, it relies heavily on the efficient solution of the state equations, on the fast computation of sensitivities and on finely discretized meshes to obtain a large number of design variables. This means that topology optimization is especially well suited for numerical methods such as the finite element method (FEM) or the finite difference method (FDM) [5]. In the work presented in this paper, we have chosen to apply the FEM. The solution to the resulting optimization problem is obtained using the method of moving asymptotes (MMA) by Svanberg [10].

The development of a robust gradient-based topology optimization model for the design of metallic microwave applications has not been given much attention until recently. Only in Erentok and Sigmund [11] the authors show the possibilities for conformal antenna design using a full volumetric representation of the conductor. However, the work in Erentok and Sigmund [11] also reveals a severe bottleneck regarding numerical efficiency. The problem is due to skin depth, i.e. the characteristic length, the electromagnetic field penetrates into a conductor before having decreased by a factor e^{-1} [4]. The situation with the skin depth being much shorter than all other length scales

DOI: 10.1002/nme

in the problem (including the wavelength of the radiation) calls for highly refined and elaborate meshes for the FEM solution of Maxwell's equation [12]. Thus, for topology optimization to be robust and efficient, a method that alleviates the skin depth issue must be developed. A similar problem arises in the optimization of fluid problems with regard to the effect of the boundary layer [13].

In [14] an optimization scheme based on genetic algorithms (GA) showed a way to circumvent the skin depth issue in FEM. The method is restricted to patch antennas and uses a perfect electric conductor (PEC) condition between and on top of the dielectric layers of the patch antenna, to model the conductor. Though the results obtained with the GA are very good, the binary handling of the PEC condition leads to an optimization model for which sensitivities cannot be determined Furthermore, it is unclear how to extend the optimization model from layered structures to full volumetric design domains, which is needed for the design of resonators for WiTricity.

In this paper, we develop an optimization model based on Maxwell's vector wave equation and a design-dependent impedance boundary condition implemented on element level. The impedance condition remedies the skin depth bottleneck, and allows us to perform full volumetric distribution of metal and dielectric by gradient-based topology optimization. To the best of our knowledge, this paper is the first demonstration of a robust and numerically fast topology optimization design technique for metallic microwave devices.

1.2. Outline

The paper is organized as follows. First, we present Maxwell's equations on strong and weak forms along with necessary boundary conditions. This constitutes the basis for the development of the design parameterization, which is presented next. Following a general formulation of the design parameterization, a set of suitable interpolation functions is suggested. Our method is illustrated by a number of numerical examples. Finally, concluding remarks are given.

2. PHYSICAL MODEL

In this section we introduce Maxwell's vector wave equation and the associated weak formulation. This leads to the natural inclusion of a mixed boundary condition, i.e. the impedance condition, which will be of key importance to the design parameterization and the resulting optimization model.

2.1. Maxwell's equations

Maxwell's equations for a linear, isotropic medium with no free charges can be cast in the frequency domain assuming time-harmonic waves using the time convention $\boldsymbol{u}(\boldsymbol{r},t)=\mathbb{R}[\boldsymbol{u}(\boldsymbol{r})\,\mathrm{e}^{\mathrm{j}\omega t}]$, where ω is the frequency, j represents the imaginary unit and $\mathbb{R}(\cdot)$ is the real part [15]. By trivial manipulations, the set of first-order partial differential equations (PDEs) can be recast as a single second-order PDE in either the electric field, $\boldsymbol{E}$, or the magnetic field, $\boldsymbol{H}$, i.e.

$$\nabla\times[\mu_{\mathrm{r}}(\boldsymbol{r})^{-1}\nabla\times\boldsymbol{E}]-k_0^2\varepsilon_{\mathrm{c}}(\boldsymbol{r})\boldsymbol{E}=\boldsymbol{0} \tag{1}$$

$$\nabla\times[\varepsilon_{\mathrm{c}}(\boldsymbol{r})^{-1}\nabla\times\boldsymbol{H}]-k_0^2\mu_{\mathrm{r}}(\boldsymbol{r})\boldsymbol{H}=\boldsymbol{0} \tag{2}$$

DOI: 10.1002/nme

where $\boldsymbol{r}$ is the position, $k_0 = \omega\sqrt{\varepsilon_0\mu_0}$ is the free space wave number, ε_0 is the free space permittivity and μ_0 is the free space permeability. The material specific parameters $\mu_r(\boldsymbol{r})$ and $\varepsilon_c(\boldsymbol{r})$ are the relative permeability and relative complex permittivity, respectively. The complex permittivity is given by

$$\varepsilon_c(\boldsymbol{r}) = \varepsilon_r(\boldsymbol{r}) - \mathrm{j}\frac{\sigma(\boldsymbol{r})}{\omega\varepsilon_0} \tag{3}$$

where $\varepsilon_r(\boldsymbol{r})$ is the dielectric function and $\sigma(\boldsymbol{r})$ is the electric conductivity. With respect to the topology optimization problem, the position-dependent material parameters, $\mu_r(\boldsymbol{r})$, $\varepsilon_r(\boldsymbol{r})$ and $\sigma(\boldsymbol{r})$, are the unknown functions to be determined.

2.2. The weak form

The finite element (FE) formulation, or weak form, can for obvious reasons not determine the solution to Maxwell's equations in infinite space. Therefore, the domain of interest is truncated and some approximation to the Sommerfeld radiation condition [15] is applied at this boundary. The most frequently used numerical approximate techniques for truncation include absorbing boundary conditions (ABC), perfectly matched layers (PML) and finite element boundary integral (FE-BI) methods [12]. Here we use the first-order ABC, which is chosen for its simplicity since the focus of this paper is on the design parameterization for topology optimization. A general sketch of an analysis problem including optimization can be seen in Figure 1. Let Ω be the total computational domain, and Γ the truncation boundary. For example in the electric field formulation, the problem becomes to find $\boldsymbol{T} \in V$

$$\int_\Omega [(\nabla \times \boldsymbol{T}) \cdot \mu_r^{-1} \cdot (\nabla \times \boldsymbol{E}) - k_0^2 \boldsymbol{T} \cdot \varepsilon_c \cdot \boldsymbol{E}]\, \mathrm{d}\Omega - \int_\Gamma \boldsymbol{T} \cdot [\boldsymbol{n} \times (\mu_r^{-1} \cdot \nabla \times \boldsymbol{E})]\, \mathrm{d}\Gamma = 0 \quad \forall \boldsymbol{E} \in V \tag{4}$$

where $\boldsymbol{T}$ denotes vector test functions and $V := H(\nabla \times \boldsymbol{v}, \Omega) = \{\boldsymbol{v} \in [L_2(\Omega)]^3 | \nabla \times \boldsymbol{v} \in [L_2(\Omega)]^3\}$ is the Sobolev space associated with the curl-operator. For more details on the vector-, or edge-, based FEs associated with the function space $H(\nabla \times \boldsymbol{v}, \Omega)$, the reader is referred to e.g. [12, 16]. The surface integral in Equation (4) means that the discrete form, or FE equations, depends on the specific boundary condition applied on Γ. Therefore, and not to loose generality, the discrete form will be stated later in Section 3 after the presentation of the new design parameterization.

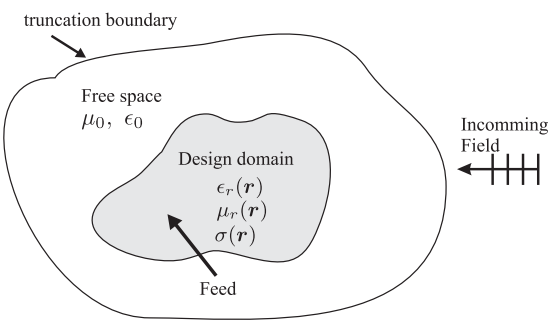

Figure 1. General sketch of an electromagnetic topology optimization problem, e.g. microwave antennas, magnetic resonators, etc.

DOI: 10.1002/nme

2.3. Conductor modeling

In EM wave propagation the skin depth, δ, is a measure for the distance through which the amplitude of a traveling plane wave decreases by a factor e^{-1} in a conductor [4]. An approximation can be obtained through the following formula [15]:

$$\delta = \frac{1}{\sqrt{\pi\sigma\mu f}} \tag{5}$$

The skin depth is important since most microwave devices have sizes in the order of mm, whereas the skin depth typically is in the μm range, i.e. three orders of magnitude smaller. To put skin depth into the context of FE and optimization, let us consider an example in which we wish to use a small cube of $1\times1\times1$ cm for the design domain. The target frequency is set to 400 MHz and the conductor is chosen to be copper with $\sigma = 5.998\times10^7$ S/m. In that case the skin depth becomes $\delta = 3.2\times10^{-6}$ m. For topology optimization each element in the design domain is possibly metallic, and thus the whole domain must be meshed such that the skin depth can be resolved. Using first-order elements[‡] one should have at least two elements per skin depth to capture the rapid decay. This leads to approximately 6200 elements in each spatial direction, i.e. a total of 2.4×10^{11} elements in 3D. Such numbers of elements imply that direct interpolation, as done in most other topology optimization problems [5], is insufficient for the microwave problem.

Owing to the skin depth issue most numerical modeling of metallic microwave devices utilizes boundary conditions to represent the conducting regions. For PEC, i.e. $\sigma=\infty$, the skin depth is zero, and the metal can be modeled by a homogenous Dirichlet condition for the electric field and a homogenous Neumann condition for the magnetic field. The above example supports that in a first approximation one may treat the metallic problem by applying a PEC boundary condition at the surface of the metallic domains. Relaxing the assumption of an infinite conductivity, an approximate relation between the electric and magnetic fields can be stated as $\boldsymbol{E}-(\boldsymbol{n}\cdot\boldsymbol{E})\boldsymbol{n} = \sqrt{\mu_\mathrm{r}/\varepsilon_\mathrm{c}}\sqrt{\mu_0/\varepsilon_0}\boldsymbol{n}\times\boldsymbol{H}$ [12] for the interface between a dielectric and a conductor. Here, $\boldsymbol{n}$ is a normal vector pointing into the conductive region. This can be cast on a form suitable for the weak formulation, i.e.

$$\boldsymbol{n}\times([\mu_\mathrm{r}^\mathrm{d}]^{-1}\nabla\times\boldsymbol{E}) + \mathrm{j}k_0\sqrt{\frac{\varepsilon_\mathrm{c}^\mathrm{m}}{\mu_\mathrm{r}^\mathrm{m}}}\boldsymbol{n}\times(\boldsymbol{n}\times\boldsymbol{E}) = \boldsymbol{0} \tag{6}$$

$$\boldsymbol{n}\times([\varepsilon_\mathrm{r}^\mathrm{d}]^{-1}\nabla\times\boldsymbol{H}) + \mathrm{j}k_0\sqrt{\frac{\mu_\mathrm{r}^\mathrm{m}}{\varepsilon_\mathrm{c}^\mathrm{m}}}\boldsymbol{n}\times(\boldsymbol{n}\times\boldsymbol{H}) = \boldsymbol{0} \tag{7}$$

where $(\cdot)^\mathrm{d}$ and $(\cdot)^\mathrm{m}$ refer to the dielectric and the metal, respectively. The conditions in Equations (6) and (7) are referred to as impedance conditions, and they form the backbone for the material interpolation scheme to be presented in the upcoming section. It should be noted that the use of adaptive, anisotropic meshes could be used to explicitly resolve the skin depth and thereby decrease the computational cost, see e.g. Erentok and Sigmund [11]. However, since microwave design problems often involve a design domain in the cm scale with skin depth in μm scale, the multiple length scales will inherently result in elaborate and dense FE meshes, even with the use

[‡]First-, or low-, order elements are often used in topology optimization since this yields the highest number of design variables [5].

DOI: 10.1002/nme

of adaptive meshing. Also, the use of adaptive meshing would require that the moving boundaries are tracked during the optimization process, thus resulting in a significant increase in algorithmic complexity.

3. DESIGN PARAMETERIZATION

The design parameterization proposed in this paper is based on the standard continuous topology optimization approach, where each FE in the design domain is associated with a continuous variable $0 \leqslant \rho^e \leqslant 1$. The design variable ρ^e is then used to interpolate between two candidate materials here denoted with $(\cdot)^{\mathrm{m}}$ for the conductor and $(\cdot)^{\mathrm{d}}$ for the dielectric. In this section, we derive a parameterization that takes the skin depth problem into account and suggests a set of suitable interpolation functions.

3.1. The element boundary condition

The skin depth problem associated with the volumetric meshing of conductive regions can be remedied by the inclusion of a design-dependent element impedance boundary condition. This can be understood as if each element in the design domain is wrapped in a possible impedance condition. An illustration of the approach can be seen in Figure 2 where Ω^e and Γ^e refer to the element volume and boundary, respectively. By the introduction of a monotonically varying function, $f(\rho^e)$, with range $f(\rho^e) \in [0, 1]$ for $\rho^e \in [0, 1]$ the impedance conditions given in Equations (6) and (7) can be made design dependent by scaling the second term with $f(\rho^e)$. For e.g. in the electric field the condition becomes

$$\boldsymbol{n} \times ([\mu_{\mathrm{r}}^{\mathrm{d}}]^{-1} \nabla \times \boldsymbol{E}) - f(\rho^e)\, \mathrm{j} k_0 \sqrt{\frac{\varepsilon_{\mathrm{c}}^{\mathrm{m}}}{\mu_{\mathrm{r}}^{\mathrm{m}}}} \boldsymbol{n} \times (\boldsymbol{n} \times \boldsymbol{E}) = \boldsymbol{0} \tag{8}$$

where it should be noted that the sign has been changed since the normal now points in the opposite direction, i.e. from conductor to dielectric, cf. Figure 2. When $f(\rho^e) = 0$ only the first term of Equation (8) remains and is equated to zero. With respect to the weak form, this means that the boundary integral in Equation (4) disappears and therefore that the standard wave equation is obtained. For $f(\rho^e) = 1$ the impedance condition is fully effective and the wave equation is suppressed, meaning that the state field is completely governed by the element boundary condition; hence, the skin depth is resolved.

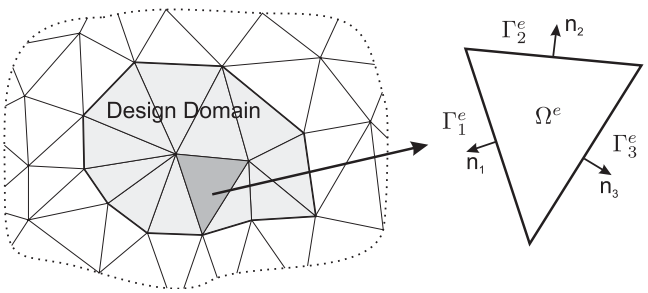

Figure 2. Sketch of FE mesh to illustrate the element boundary condition imposed on the design elements.

DOI: 10.1002/nme

Note that the obvious first choice of interpolation would have been the conductivity directly. However, since $\sigma = 0$ we have that $\varepsilon_c = \varepsilon_r$, which means that the element boundary condition does not vanish for $\rho^e = 0$. Instead we use Equation (8) that ensures that the element impedance condition vanishes for $f(\rho^e) = 0$. Also the physical interpretation of intermediate densities is uncertain, though one might be able to link them to materials with varying conductivities. However, if the final design has $\rho = 0$ or $\rho = 1$ in all design elements, the physical performance of the optimized design has been analyzed with a correct physical model. Thus, if the design parameterization is devised such that the final design is black and white, there is no problem in allowing the optimizer to pass through intermediate densities during the iterative optimization process. This is a commonly used trick in topology optimization [5] and will also be used in the work presented here.

3.2. Design-dependent Maxwell's equations

The design dependence in Maxwell's equations including the element boundary condition, Equation (8), can be stated generally, i.e. without explicit definitions of the interpolation functions, for a single design element as

$$\begin{aligned} \nabla \times (A \nabla \times \boldsymbol{u}) - k_0^2 B \boldsymbol{u} = 0 \quad & \text{in } \Omega^e \\ \boldsymbol{n} \times (\tilde{A} \nabla \times \boldsymbol{u}) - f(\rho^e) \mathrm{j} k_0 \sqrt{\tilde{A}\tilde{B}}\, \boldsymbol{n} \times (\boldsymbol{n} \times \boldsymbol{u}) = 0 \quad & \text{on } \Gamma^e \end{aligned} \tag{9}$$

where Ω^e and Γ^e refer to the element volume and boundary, respectively, and $\boldsymbol{n}$ is an outward normal for element e. The dependent vector field $\boldsymbol{u}$ and its associated parameters A, B, $\tilde{A}$, $\tilde{B}$ are given in Table I. The difference between parameters with $\tilde{(\cdot)}$ and those without is that A and B are design dependent while $\tilde{A}$ and $\tilde{B}$ simply refer to the conductor. The latter parameters must be constant since the element impedance condition's sole purpose is to remedy the skin depth problem associated with conducting regions.

3.3. Interpolation functions

The interpolation function needed to complete the design parameterization of Maxwell's equations, i.e. Equation (9), should be chosen such that the following requirements are met best possibly. The interpolation functions must be valid for both the electric and magnetic field formulations of Maxwell's equations. Furthermore, the functions have to be monotonically varying and should have the property that a small change in ρ^e should lead to a small change in system response. Finally, the interpolation functions should, if possible, result in designs free from intermediate values of ρ^e. In mechanical topology optimization problems a penalization parameter is required to obtain black and white designs, as done for e.g. in the solid isotropic material with penalization (SIMP) scheme, where the stiffness is penalized to make intermediate densities uneconomical [5, 17] for

Table I. Field-dependent parameters for the design parameterization used for conductor/dielectric-based topology optimization, Equations (9). The superscript $(\cdot)^{\mathrm{m}}$ refer to the metal, i.e. the conductor. The functions $\mu_r(\rho^e)$, $\varepsilon_r(\rho^e)$ and $\sigma(\rho^e)$ are given in Equation (10).

$\boldsymbol{u}$	A	B	$\tilde{A}$	$\tilde{B}$
$\boldsymbol{E}$	$\mu_r(\rho^e)^{-1}$	$\varepsilon_r(\rho^e) - \mathrm{j}\frac{\sigma(\rho^e)}{\omega\varepsilon_0}$	$(\mu_r^{\mathrm{m}})^{-1}$	$\varepsilon_r^{\mathrm{m}} - \mathrm{j}\frac{\sigma^{\mathrm{m}}}{\omega\varepsilon_0}$
$\boldsymbol{H}$	$(\varepsilon_r(\rho^e) - \mathrm{j}\frac{\sigma(\rho^e)}{\omega\varepsilon_0})^{-1}$	$\mu_r(\rho^e)$	$(\varepsilon_r^{\mathrm{m}} - \mathrm{j}\frac{\sigma^{\mathrm{m}}}{\omega\varepsilon_0})^{-1}$	μ_r^{m}

DOI: 10.1002/nme

the optimizer. However, as will be explained in the following section the EM optimization problem does not require any type of penalization to ensure black and white designs.

The functions presented below are determined based on numerical studies where we have used an energy measure, cf. the numerical examples in Section 5, to test and compare candidate interpolation schemes.

$$\begin{aligned}
&\mu_{\mathrm{r}}(\rho^e) = \mu_{\mathrm{r}}^{\mathrm{d}} + \rho^e(\mu_{\mathrm{r}}^{\mathrm{m}} - \mu_{\mathrm{r}}^{\mathrm{d}}), \quad \sigma(\rho) = \sigma_0 10^{\left[\log_{10}\left(\frac{\sigma^{\mathrm{d}}}{\sigma_0}\right) + \rho^e\left\{\log_{10}\left(\frac{\sigma^{\mathrm{m}}}{\sigma_0}\right) - \log_{10}\left(\frac{\sigma^{\mathrm{d}}}{\sigma_0}\right)\right\}\right]} \\
&\varepsilon_{\mathrm{r}}(\rho^e) = \varepsilon_{\mathrm{r}}^{\mathrm{d}} + \rho^e(\varepsilon_{\mathrm{r}}^{\mathrm{m}} - \varepsilon_{\mathrm{r}}^{\mathrm{d}}), \quad f(\rho^e) = \rho_{\mathrm{e}}^{p_{\mathrm{BC}}} \\
&p_{\mathrm{BC}} \approx 13 \text{ for } \boldsymbol{E}, \quad p_{\mathrm{BC}} \approx 1 \text{ for } \boldsymbol{H}
\end{aligned} \tag{10}$$

The linear interpolation of the dielectric function and the permeability are successfully adopted from e.g. [9, 18, 19]. Interpolation of the conductivity is however not straightforward. This is due to two properties of σ. First, the numerical range is huge, i.e. $\sigma = 0$ for free space and $\sigma = 10^7$ S/m for a typical good conductor [15]. Second, the conductivity is a damping parameter for the electromagnetic fields. This means that even numerically small conductivities can lead to large changes in field response, and furthermore that conductivities above a certain threshold limit will only have a small influence on the response. Owing to these issues, it was found that the interpolation of σ was best performed in the logarithmic scale, and then converted back to the physical scale using a power function as proposed in [20]. For the logarithmic scaling to be physically sound, a reference conductivity, σ_0, is introduced such that the interpolated conductivities become dimensionless. The reference conductivity could, for example, be chosen as the conductivity of copper, i.e. $\sigma_0 = 5.998 \times 10^7$ S/m. The resulting interpolation function can be seen plotted in Figure 3(a) and in logarithmic scale in Figure 3(b). Finally, note that σ^{d} must always be larger than zero, even for lossless dielectrics due to the logarithmic interpolation. For lossless dielectrics, we suggest to use $\sigma^{\mathrm{d}} = 10^{-4}$ based on the numerical experiments.

The interpolation function $f(\rho)$ for the element impedance condition must take the difference in field formulation into account. For the electric field the impedance condition is proportional to ε_{c}, whereas it is proportional to the inverse, i.e. $\varepsilon_{\mathrm{c}}^{-1}$, for the magnetic field. From numerical experiments it was found that $f(\rho)$ for the electric field should be similar to a logarithmic function, whereas $f(\rho)$ should be close to linear for the magnetic field. Since we wish to use the same function for both field formulations, a polynomial with varying exponent is a simple and convenient choice, i.e. $f(\rho) = \rho^{p_{\mathrm{BC}}}$. The exponent p_{BC}, which should not be seen as a penalization parameter cf. the SIMP scheme [17], yields good 0–1 results when using $p_{\mathrm{BC}} \approx 1$ for the magnetic field and $p_{\mathrm{BC}} \approx 13$ for the electric field. A plot of $f(\rho)$ can be seen in Figure 3(c). The reason why a penalization parameter is not needed for the EM problem is due to the inherent damping nature of the conducting material. By this is meant that regions of intermediate conductivities slowly damp, or absorb, the energy from the EM fields, whereas a high conductivity means fast spatial decay and as a result that less energy is dissipated.

As already stated one may think of the design of electrically conducting devices as the distribution of highly damping material. Owing to numerical precision this means that σ^{m} larger than some value, $\sigma_{\mathrm{cutoff}}^{\mathrm{m}}$, does not change the system response much. With respect to the optimization a numerically large σ^{m} will then lead to designs with intermediate design variables, since the optimizer would not benefit from letting $\sigma(\rho) \to \sigma^{\mathrm{m}}$. Therefore, a study to determine the threshold values of σ^{m} has been conducted. For the electric field the limit was found to coincide with the conductivity of copper, i.e. $\sigma_{\mathrm{E_{cutoff}}}^{\mathrm{m}} \approx 10^7$, S/m, whereas for the magnetic field it was lower, i.e.

DOI: 10.1002/nme

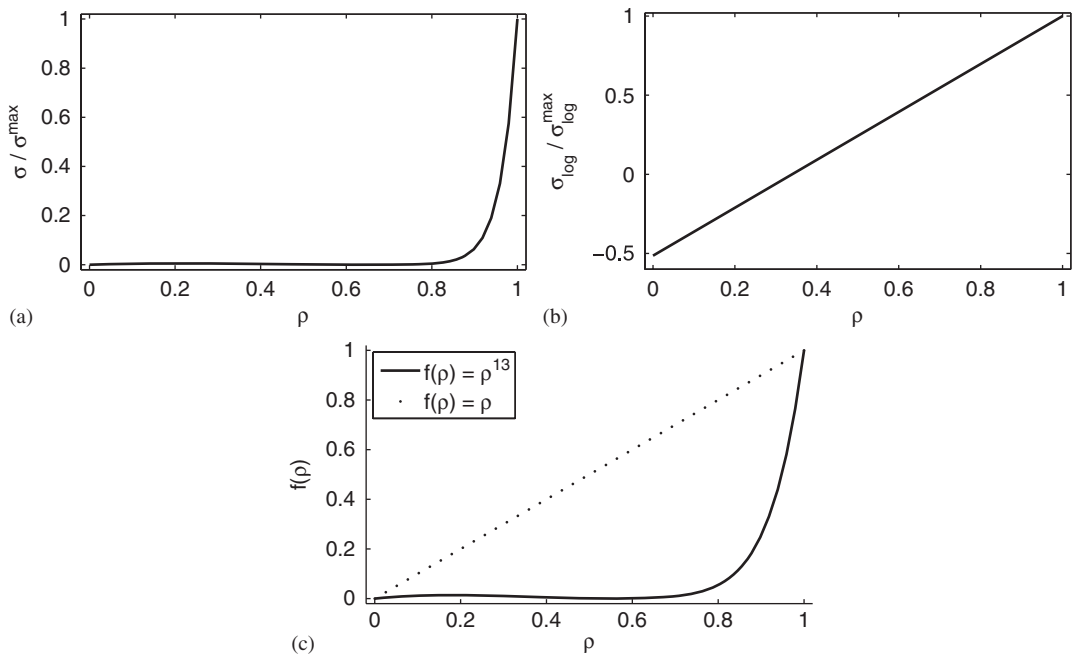

Figure 3. Plot of the interpolation function for the conductivity: (a) $\sigma(\rho)$ and (b) $\log 10(\sigma(\rho))$ using $\sigma^{\mathrm{m}} = 10^7\,\mathrm{S/m}$, $\sigma^{\mathrm{d}} = 10^{-4}\,\mathrm{S/m}$ and $\sigma_0 = \sigma^{\max} = 10^7\,\mathrm{S/m}$. In (c) the interpolation function for the element boundary condition, $f(\rho)$, is shown for both the magnetic, $p_{\mathrm{BC}} = 1$, and electric field, $p_{\mathrm{BC}} = 13$, formulations.

$\sigma^{\mathrm{m}}_{\mathrm{H_{cutoff}}} \approx 10^6\,\mathrm{S/m}$. Hence, the design parameterization should not be used to distinguish between good conductors, such as copper and silver, but should merely be used to model a good conductor.

3.4. Weak form for design elements

The linear system, or FE equations, resulting from the discretization of the design-dependent Maxwell's equations, i.e. Equation (9), can easily be computed based on the standard Galerkin method [12]. The linear system takes on the following form when the design domain is separated from the remaining computational domain:

$$(\boldsymbol{S}(\rho) + \boldsymbol{A})\boldsymbol{u} = \boldsymbol{f} \tag{11}$$

where $\boldsymbol{S}(\rho)$ refers to the design element contributions, $\boldsymbol{A}$ contains free space, fixed domains and domain truncation contributions and $\boldsymbol{f}$ contains the system load. The system matrix for the design elements can be computed for the electric field formulation as

$$\boldsymbol{S}(\rho) = \sum_{e=1}^{N} (\boldsymbol{K}^e(A) - \boldsymbol{M}^e(B) - \boldsymbol{B}^e(f(\rho), \tilde{A}, \tilde{B}))$$

$$\boldsymbol{K}^e(B) = \int_{\Omega^e} (\nabla \times \boldsymbol{N}) \cdot A \cdot (\nabla \times \boldsymbol{N})\, \mathrm{d}\Omega$$

DOI: 10.1002/nme

$$\boldsymbol{M}^e(A) = \int_{\Omega^e} k_0^2 \boldsymbol{N}\cdot B\cdot \boldsymbol{N}\,\mathrm{d}\Omega$$

$$\boldsymbol{B}^e(f(\rho), \tilde{A}, \tilde{B}) = f(\rho^e)\,\mathrm{j}k_0 \int_{\Gamma^e} (\boldsymbol{n}\times\boldsymbol{N})\cdot\sqrt{\tilde{A}\tilde{B}}\cdot(\boldsymbol{n}\times\boldsymbol{N})\,\mathrm{d}\Gamma \tag{12}$$

where the summation refers to the FE assembly process and N is the number of design elements. The only non-standard term in Equation (12) is the element boundary integral, which may be evaluated if access to element normals and shape functions is available. The contributions to the linear system due to loading and mesh truncation is not of importance to the work presented here, and the reader is referred to e.g. [12, 16] for details on the computation of $\boldsymbol{A}$ and $\boldsymbol{f}$.

4. OPTIMIZATION PROBLEM

The aim of this section is to introduce the topology optimization problem on standard form and to outline the numerical solution. The objective function, $\Phi(\rho, \boldsymbol{u})$, is for simplicity restricted to energy measures that can be stated as $\bar{\boldsymbol{u}}^{\mathrm{T}}\boldsymbol{Q}\boldsymbol{u}$, where $\bar{\boldsymbol{u}}^{\mathrm{T}}$ refers to the complex transpose and $\boldsymbol{Q}$ is a matrix specific to the energy evaluated. This approach can be used to optimize e.g. magnetic and electric energies as well as energy flow using the Poynting vector [15]. Based on this objective we formulate the following optimization problem:

$$\begin{aligned} \max_{\rho\in\mathbb{R}^N} \quad & \Phi(\rho,\boldsymbol{u}) = \log_{10}\left(\frac{\bar{\boldsymbol{u}}^{\mathrm{T}}\boldsymbol{Q}\boldsymbol{u}}{\Phi_0}\right) \\ \text{s.t.} \quad & \text{Governing equations} \\ & \frac{\sum_{\mathrm{e}}^N \rho_e V_e}{Vf^*} - 1 < 0 \\ & 0 \leqslant \rho^e \leqslant 1, \quad e = 1, N \end{aligned} \tag{13}$$

where Φ_0 is a reference energy used for rendering the objective function dimensionless. The second constraint is a restriction on the available material imposed to limit the amount of conductor used for the design problem, with the added benefit of possible convergence speed up (see numerical examples). Opposite to, e.g. compliance minimization [5] the electromagnetic problems investigated in this work do not, necessarily, lead to designs, which benefit from utilizing all of the available material. Thus, Vf^* should be regarded as a limit on the material and not as a target volume fraction. The logarithm for the objective is included for proper numerical scaling and the density filter, see [21–23], is applied to introduce a minimum length scale to the design problem. Since the density filter introduces a region of undesirable intermediate design variables, it is applied in conjunction with a continuation scheme such that the filter radius, $R_{\min}$, gradually approaches zero as the optimization process progresses. The sensitivities are determined using the adjoint method [18], and the design update is performed using the MMA written and implemented in Matlab by Svanberg [10]. A program capable of solving the described optimization problem has been implemented in Matlab. The implementation includes both nodal and edge-based 2D triangular elements [12]. For simplicity, only the first-order ABC is used for domain truncation and the open source mesh tool GMSH [24] is used to generate geometries and FE meshes.

DOI: 10.1002/nme

5. NUMERICAL EXAMPLES

In this section we demonstrate the usability of the proposed design parameterization by solving a couple of illustrative, yet academic, design problems.

5.1. Magnetic resonator

The first numerical example is the design of magnetic resonators, which can be regarded as the design of a highly simplified energy harvesting device. The goal is to maximize the magnetic energy, $\int_{\Omega^{\text{obj}}} \mu |H|^2 \, \mathrm{d}\Omega$, in the cylinder, Ω^{obj}, by the distribution of a good conductor, e.g. copper, in the two design domains, Ω^{des}. The system is fed by an incident plane wave traveling from left to right and the problem setup can be seen illustrated in Figure 4. The target frequency is set to 115 MHz, which is chosen since a frequency sweep of the structure (solid circle) with $\rho^e = 1$ for all $\rho^e \in \Omega^{\text{des}}$ showed a peak in magnetic energy at this frequency with $\Phi = -0.68$. This trivial design will in the following be referred to as the reference design.

The model problem assumes transverse electric (TE) polarization, that is

$$\begin{aligned} \boldsymbol{H} &= H_z(x, y)\boldsymbol{e}_z \\ \boldsymbol{E} &= E_x(x, y)\boldsymbol{e}_x + E_y(x, y)\boldsymbol{e}_y \end{aligned} \tag{14}$$

which leads to either the scalar Helmholtz equation for the H_z field, or a vector curl–curl equation for the electric field in the plane. To demonstrate that the design parameterization works equally well for both the electric and magnetic formulations, the design problem is solved using both formulations, i.e. nodal elements for H_z and edge elements for E_x and E_y [12].

The optimization problem is solved using $\sigma^{\text{m}} = 10^6$ S/m, an allowed volume fraction of 30%, $R_{\min} = 0.1$ m for the density filter, $\|\rho\|_\infty \leqslant 3\%$ as stopping criteria and a uniform initial distribution with $\rho_{\text{init}} = 0.3$ if nothing else is stated. The objective is evaluated using $\boldsymbol{Q} = \sum_{e=1}^{N_{\text{obj}}} \mu_e \boldsymbol{N}_{\text{e}}^{\text{T}} \boldsymbol{N}_e$, where N_{obj} is the number of elements in the objective domain. The reference energy used to make the objective function dimensionless is chosen to be $\Phi_0 = 4 \times 10^{-7}$ J.

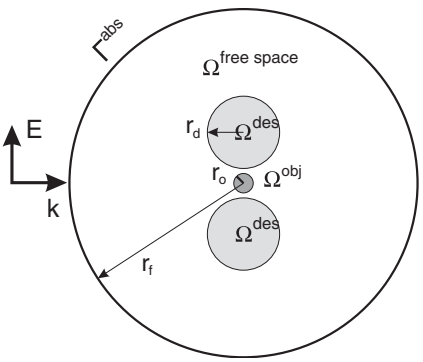

Figure 4. Sketch of design problem with $r_d = 0.65$ m, $r_o = 0.08$ m and $r_f = 3.0$ m. The target frequency is 115 MHz and the materials are a good conductor e.g. copper and air. No explicit symmetry is enforced on the two design domains.

DOI: 10.1002/nme

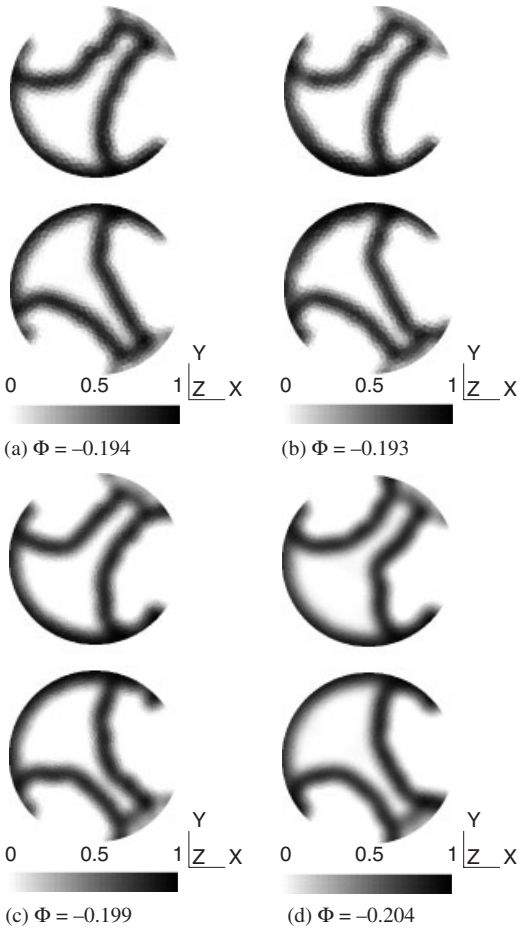

Figure 5. Optimized designs for the problem in Figure 4 for three different mesh resolutions with fixed density filter. The number of design elements are (a) 5000 edge elements; (b) 5000 nodal elements; (c) 10 000 nodal elements; and (d) 20 000 nodal elements. Convergence was reached in 100 to 150 iterations and the optimized designs are approximately 310% better than the reference design.

The optimized designs in Figure 5 are based on three different mesh resolutions using both nodal and edge FEs. The designs are obtained without the use of the continuation approach for the density filter, which means that they can be directly compared. All four designs in 5(a)–(d) are found to yield almost identical objectives, corresponding to a 310% improvement compared with the reference design. The designs are also seen to have qualitatively the same material layout, indicating that the design parameterization together with the fixed density filter radius provides a mesh and field-independent design method. However, by close inspection of the optimized designs it is noticed that they have small anomalies that break the expected symmetry. This is a direct consequence of the FE mesh being unstructured, i.e. asymmetric, and the anomalies can therefore be explained as numerical artifacts. The noise may be removed using morphology-based filters [23].

DOI: 10.1002/nme

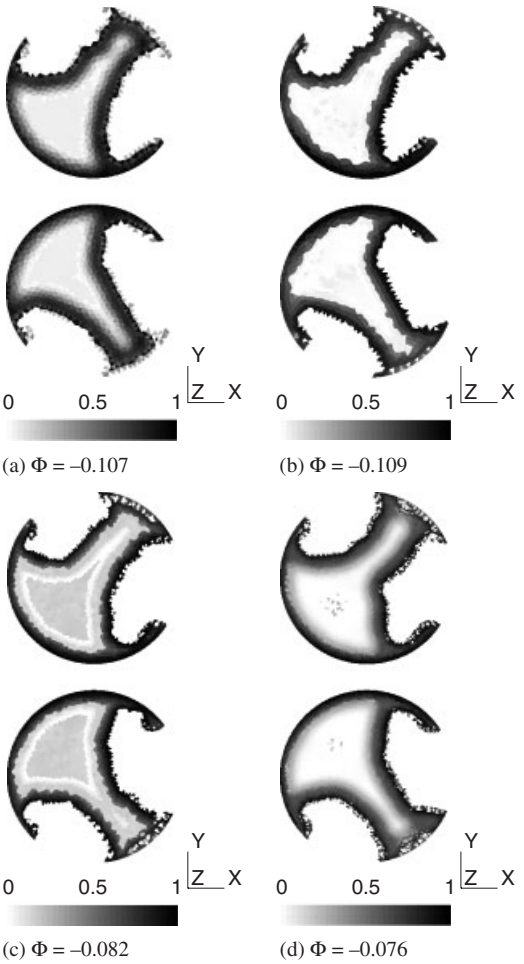

Figure 6. Optimized designs for the problem in Figure 4 for three different mesh resolutions. The number of design elements are (a) 5000 edge elements; (b) 5000 nodal elements; (c) 10 000 nodal elements; and (d) 20 000 nodal elements. Convergence was reached in 150 to 250 iterations using the continuation approach for the density filter. The optimized designs are approximately 400% better than the reference design.

Since the fixed filter radius forces the designs to be contaminated with gray design variables, the examples from Figure 5 are rerun using the continuation approach for the density filter. This means that the optimization problem is first solved to convergence with $R_{\min} = 0.1\,\mathrm{m}$, after which the filter radius is changed to $R_{\min} = 0.0\,\mathrm{m}$ and the optimization is continued until convergence is reached. The resulting optimized designs are shown in Figure 6(a)–(d). From this it is seen that the objective values are improved by a factor of two, i.e. the optimized designs are approximately 400% better than the reference. The overall topologies are still comparable, though now the optimizer has utilized the difference in mesh refinement, which leads to better objectives for higher mesh resolution. Though the density filter is applied as a continuation approach, there

DOI: 10.1002/nme

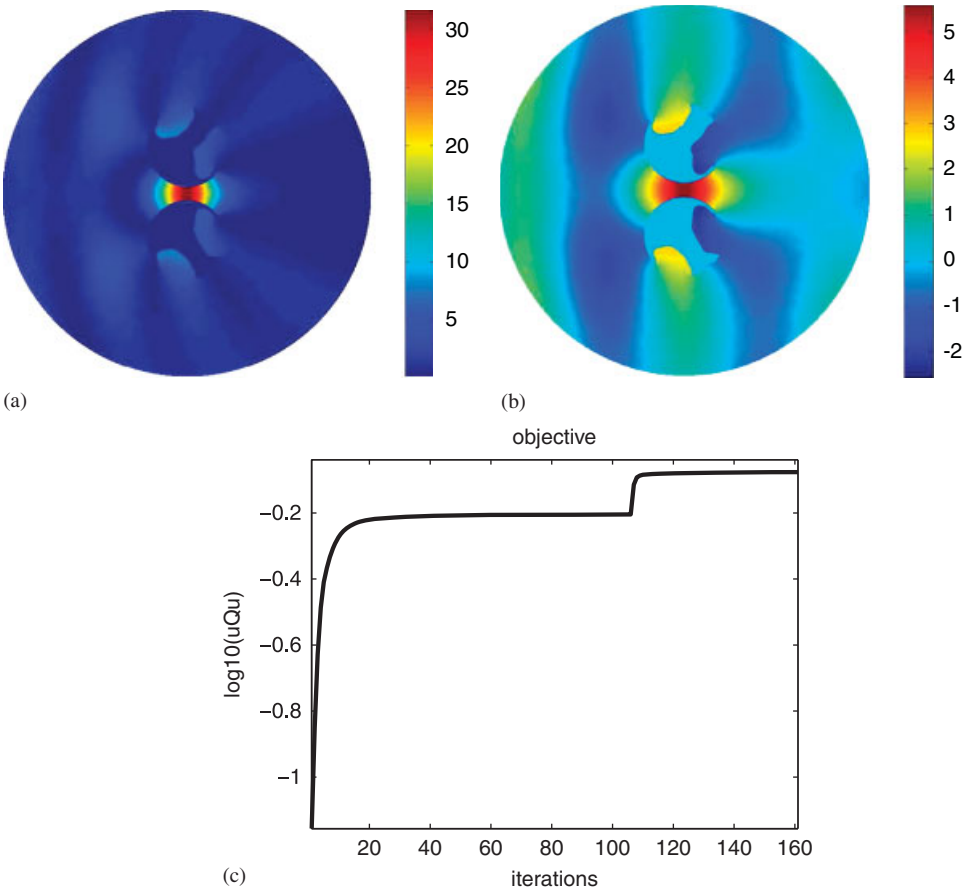

Figure 7. Plot of the magnetic energy (a), the magnetic field (b) and convergence history (c) associated with the optimized design in Figure 5(d). The kink in the convergence history is due to the continuation approach applied for the density filter.

are still gray elements in the optimized design. However, the intermediate densities are primarily located on the inside of the optimized structure where they have little influence on the system response. Also, the interface between free space and conductor is noted to be rugged and prone to checkerboards, i.e. single node connections. This rough transition and one-node connections makes possible manufacturing difficult, which indicates that a more advanced filter, such as the Heaviside filter [25], should be applied to prevent rapid oscillations.

The magnetic field and the energy associated with the optimized design in Figure 6(d) is shown in Figure 7 together with the convergence history. The convergence, both with and without the density filter, is seen to be monotone. From the plot of the magnetic energy in Figure 7(a), one can see that the energy attains its maximum at the center of the domain, i.e. in Ω^{obj}. From the plot of the magnetic field in Figure 7(b) it is observed that the field inside the hammer-like design is zero. This means that the system response would be the same if one were to fill the cavity with metal.

DOI: 10.1002/nme

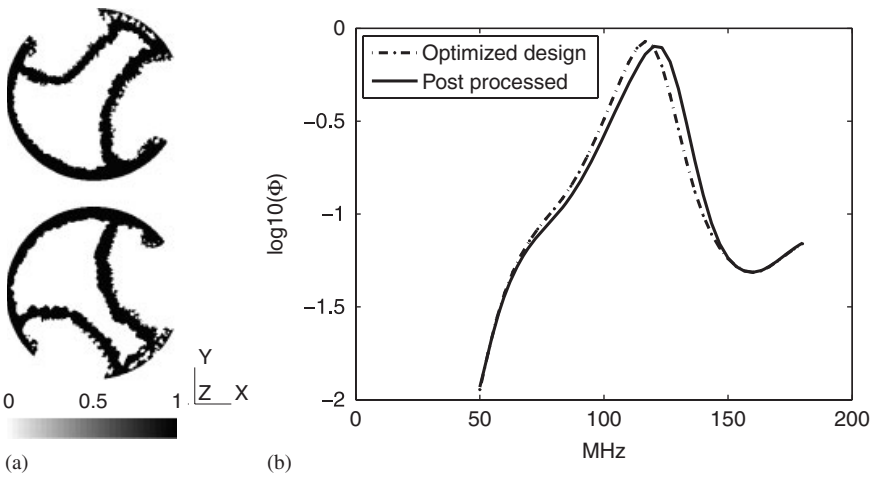

Figure 8. Post processing results based on the optimized design of Figure 6(b). The cut off is chosen as $\rho^e > 0.5 \rightarrow 1$ and zero for all other elements. The frequency sweep of the post processed design displays its maximum at 120 MHz with $\Phi = -0.075$, whereas the optimized design has $\Phi = -0.07$ at 116 MHz.

To validate the optimization results, the optimized designs are rendered pure 0–1 and then analyzed using a PEC condition. The fully black and white design is obtained by setting all design variables with $\rho^e \geqslant \rho^e_{\text{cutoff}}$ equal to one and all others to zero. On the now well-defined interface between metal and air we apply a PEC condition and analyze the system response with a frequency sweep. As example the design in Figure 6(c) is used with $\rho^e_{\text{cutoff}} = 0.5$. The rendered design and frequency response is shown in Figure 8. From this figure it is seen that the objective value is in good agreement with the optimization result. However, there is a 4% shift in target frequency, i.e. the post processed design has its maximum at 120 MHz opposed to the 115 MHz used for the optimization. Almost identical frequency responses and shifts in target frequency is obtained using $\rho^e_{\text{cutoff}} = 0.3$ and $\rho^e_{\text{cutoff}} = 0.7$. The shift in frequency is most likely due to the remaining gray design variables in the optimized design and the none smooth interface between air and conductor. We emphasize that while the interpolation function $f(\rho)$ of course have clear interpretations in the limits of either $\rho = 0$ or $\rho = 1$, the function is merely an optimization instrument in the intermediate regime. The proposed interpolation is not unique but as argued above it serves the present optimization purpose.

To illustrate the necessity of a design filter to achieve coherent and easily manufacturable designs, an optimization problem started with $R_{\text{min}} = 0$ is conducted. The result is shown in Figure 9(a). Though the objective value is comparable with the one obtained using the filtered design approach, the unfiltered design is clearly less coherent and shows the presence of unconnected design variables with $\rho^e > 0$. In the 3D setting this would lead to gravity defying designs, and should thus be avoided.

The classical problem of reaching undesired local minima, due to non convexity in the total optimization problem [5], is also present for the design of metallic microwave devices. This can easily be exemplified by starting the optimization with different values of ρ_{init}. In Figure 9(b) an optimized design using $\rho_{\text{init}} = 0$ without a volume constraint is given. This design yielded an function value of $\Phi = -0.42$ and was terminated after 600 iterations without reaching the convergence criteria. The design is seen to be of a completely different topology compared with those in Figure 6, and the objective is only a 90% improvement of the reference design. Generally it

DOI: 10.1002/nme

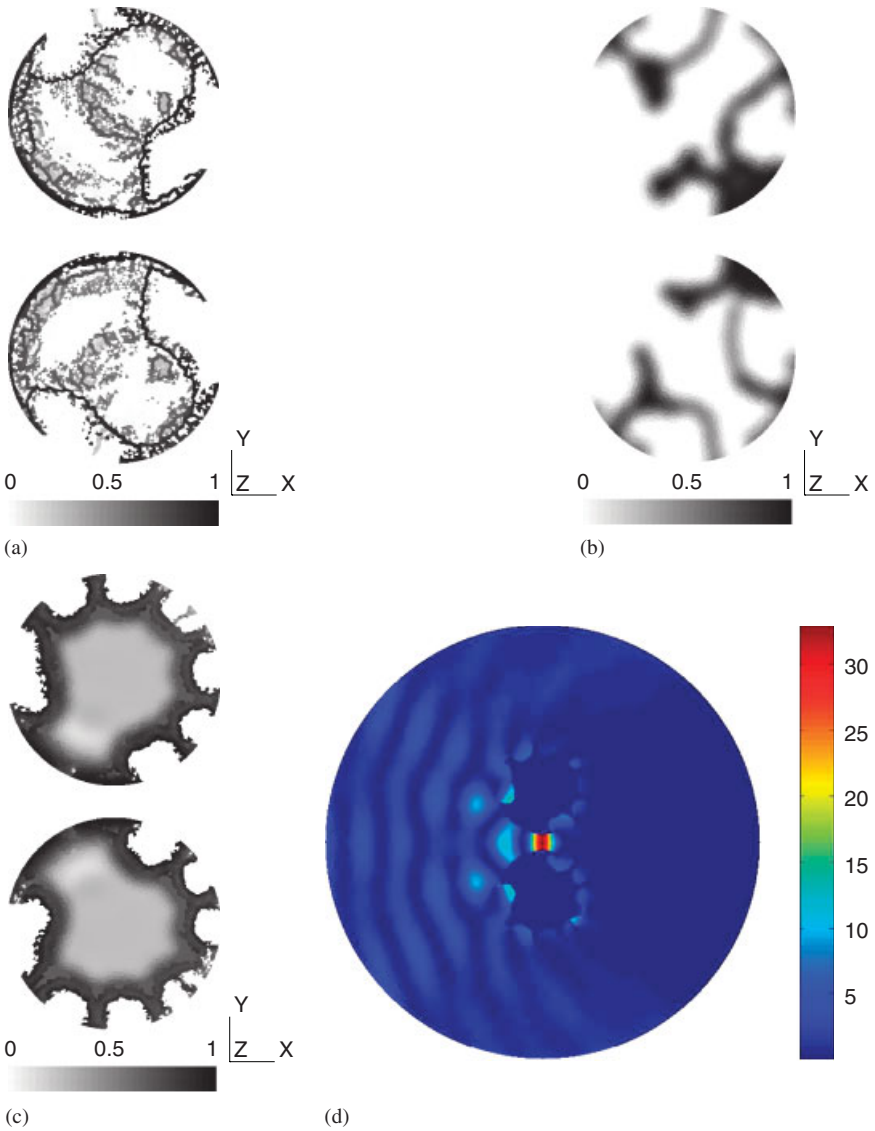

Figure 9. (a) Design obtained without the density filter that yields an objective of $\Phi = -0.10$. In (b) the optimized design is obtained using $\rho_{\text{init}} = 0$, which lead to $\Phi = -0.42$ after 600 iterations, i.e. terminated before convergence was achieved. The design in (c) is obtained using 300 MHz as target frequency. The associated magnetic field is shown in (d).

was found that using $\rho_{\text{init}} \in [0.1, 0.4]$ led to designs similar to those in Figure 6, whereas $\rho_{\text{init}} < 0.1$ yielded less good designs in terms of objective. For ρ_{init} near one the optimization process is locked and no significant improvement was obtained, i.e. the stopping criteria was reached in one or two iterations indicating a local optimum. Finally, it should be noted that all designs presented in this section utilized all of the available material, i.e. had active volume constraints upon termination

DOI: 10.1002/nme

of the optimization process. The same examples were also run without a volume constrain, i.e. $f^* = 1$, which resulted in many more optimization iterations before convergence, if the problem converged at all before reaching the maximum number of iterations. The designs and objectives were however found to be close to identical, with the only noticeable difference being the material layout in the interior of the optimized structure. This indicates that the volume constraint can be used to restrict the optimization algorithm, and thus speed up convergence, due to the enclosed nature of the optimized designs.

The last example uses the same settings as given in the introduction to this section, but with a target frequency of 300 MHz. The optimized design is shown in Figure 9(c), where it is noted that the shorter wavelength leads to more grooves in the circumference of the design domain. As for the other successfully optimized designs for 115 MHz, the energy is concentrated in the objective domain, cf. Figure 9(d). The similar topologies in the optimized designs for both frequencies indicates that the design with grooves along the circumference is a strong local minima. The physical interpretation of the grooves, e.g. groove size vs wavelength and field enhancement effect, is not pursued further in this paper and is left to future work.

5.2. *Electric resonator*

The second optimization problem is the design of an electric resonator. This example is primarily included to demonstrate that some optimization problems lead to designs that are in excellent agreement with the post processing result. The objective for the current design problem is to maximize the electric energy, $\int_{\Omega^{\text{obj}}} \varepsilon |E|^2 \, \mathrm{d}\Omega$, in the cylinder, Ω^{obj}, by the distribution of a good conductor, e.g. copper, in the design domain Ω^{des}. An incident electric field is imposed from left to right. The target frequency is set to 300 MHz and the design problem is shown in Figure 10. The model problem assumes TE polarization, that is

$$\begin{aligned} \boldsymbol{E} &= E_z(x, y)\boldsymbol{e}_z \\ \boldsymbol{H} &= H_x(x, y)\boldsymbol{e}_x + H_y(x, y)\boldsymbol{e}_y \end{aligned} \tag{15}$$

The optimization problem is solved for 8000 design variables with $\rho_{\text{init}} = 0.1$ and fixed filter radius $R_{\min} = 0.04$ m. The objective function is in this example scaled by a reference energy of $\Phi_0 = 8.8452 \times 10^{-12}$ J. The optimized design is shown in Figure 11(a), and is seen to take on the shape of a multilayered parabola, which makes intuitive sense. The achieved objective is $\Phi = 0.47$ and the optimization converged in 120 iterations. The gray part of the design in the left side of the domain does not influence the performance of the system since this is shielded from the incoming field. The intermediate densities could probably be avoided by the imposition of a volume constraint. It is interesting to see that this design problem does not benefit from a volume constraint w.r.t. convergence speedup, as opposed to the examples of the previous section. This is due to the fact that the optimized design in Figure 11 does not contain any enclosed regions as was the case for the TM optimized design.

In Figure 11(b) a post processed design is shown and in Figure 11(c) the result of a frequency sweep using a PEC conditions is presented. The post processed design has an objective of $\Phi = 0.53$ at 299 MHz, which is in excellent agreement with the optimization result. The increase in objective for the post processed design is a direct result of the removal of intermediate design variables caused by the density filter, just as seen when using the continuation scheme for $R_{\min}$ in the magnetic resonator design problem. It is seen that the frequency response of the optimized design

DOI: 10.1002/nme

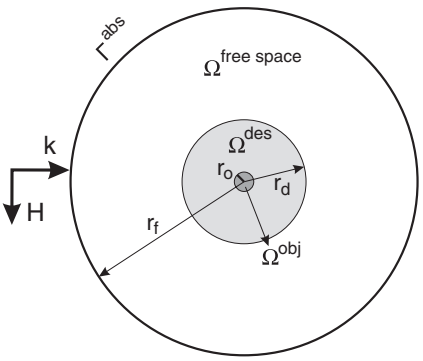

Figure 10. Sketch of the design problem with $r_d = 1.0\,\text{m}$, $r_o = 0.15\,\text{m}$ and $r_f = 5.0\,\text{m}$. The target frequency is 300 MHz and the materials are a good conductor e.g. copper and air.

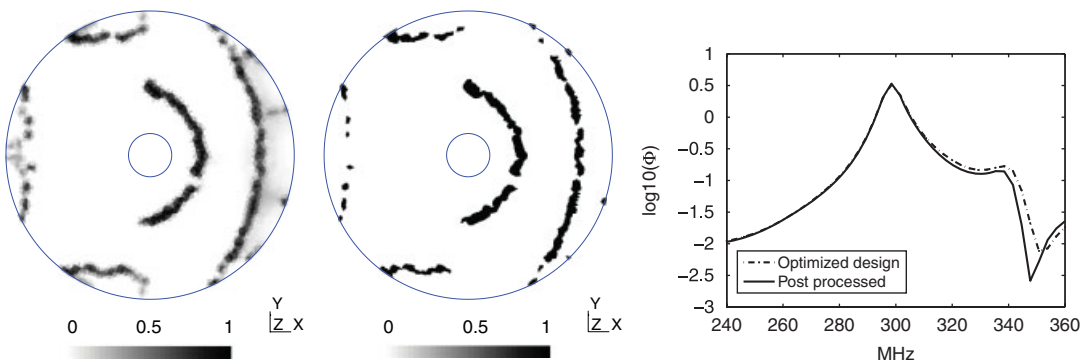

(a) (b) (c)

Figure 11. (a) Optimized design based on the problem described in Figure 10. Convergence was achieved after 120 iterations with $\Phi = 0.47$. The design in (b) is post processed using $\rho > 0.5 \rightarrow 1$, and graph in (c) shows the frequency sweep of both the optimized and post processed designs. The post processed has maximum at 299 MHz with $\Phi = 0.53$, whereas the optimized design has maximum of $\Phi = 0.51$ at 299 MHz.

deviates from the response of the post processed design for higher frequencies. This could indicate that the mesh used is not fine enough to capture the physics above 320 MHz.

5.3. *Monopole antenna*

The final numerical example is included to demonstrate the design parameterization applied to a real, though rather simple antenna design problem. The optimization problem consists of determining the optimal length of a $50\,\Omega$ fed monopole antenna operating at 300 MHz. This problem has an analytic solution that states that $l \approx 0.211\lambda$ with $\lambda = 1\,\text{m}$ [4]. The physical problem can be described by a 2D axial symmetric model, i.e.

$$\begin{aligned} \boldsymbol{H} &= H_\phi(r,z)\boldsymbol{e}_\phi \\ \boldsymbol{E} &= E_\text{r}(r,z)\boldsymbol{e}_\text{r} + E_z(r,z)\boldsymbol{e}_z \end{aligned} \tag{16}$$

DOI: 10.1002/nme

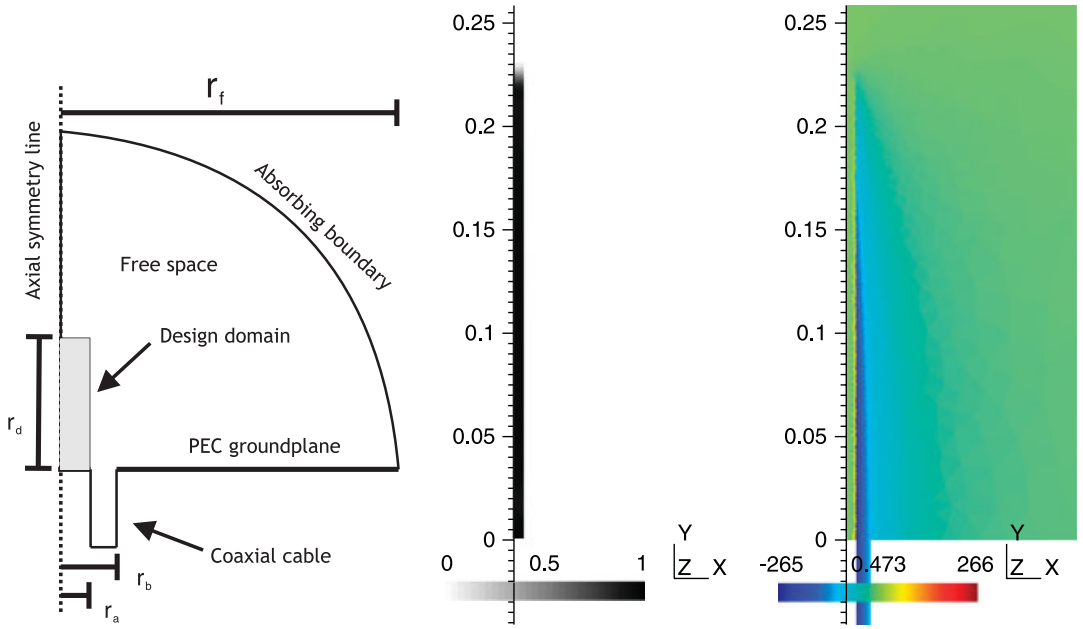

Figure 12. (a) Sketch of the design problem with $r_a = 5\,\text{mm}$, $r_b = 11.5\,\text{mm}$, $r_d = 0.5\,\text{m}$ and $r_f = 1.0\,\text{m}$. The optimized design in shown in (b), where the monopole length is seen to be in fair agreement with the analytical prediction. The magnetic field along the monopole antenna is shown in Figure (c).

The $50\,\Omega$ coaxial cable feed is modeled using a waveguide port boundary condition where only the first TEM mode is included [26]. The problem setup is sketched in Figure 12(a), and the objective is to maximize the energy flowing through the absorbing boundary, i.e. the time-averaged Poynting vector.

$$\langle S \rangle = \int_{\Gamma^{\text{abc}}} \boldsymbol{n} \cdot \left(\frac{1}{2} \mathbb{R}[\boldsymbol{E} \times \bar{\boldsymbol{H}}] \right) \mathrm{d}\Gamma \tag{17}$$

which is scaled by $\Phi_0 = \omega^{-1} 8.8542 \times 10^{12}\,\text{W}$ to ensure a non-dimensional objective function. The optimization problem is solved using a fixed filter radius, $R_{\min} = 5\,\text{mm}$, and without any volume constraint. The filter radius is chosen such that the optimized design is forced to be a rod, i.e. a monopole antenna, and thus the design problem is reduced to the determination of the optimal monopole length. The optimization is conducted on a mesh of 17 782 triangular elements of which 2078 are design variables. From Figure 12(b) we see that the optimized length of approximately 0.225λ is in fairly good agreement with the analytical prediction, which further validates the proposed design parameterization. The increase in monopole length obtained by topology optimization is attributed to the fact that the analytical prediction assumes the monopole width to be infinitesimal. It is thus to be expected that an increase in width leads to an increase in optimal length [4].

DOI: 10.1002/nme

6. CONCLUSION AND FUTURE WORK

In this paper, we have developed a design parameterization that allows for numerically efficient topology optimization of electromagnetic metallic microwave devices.

The design method is based on the frequency-domain FEM with elementwise constant design variables. The numerical efficiency is obtained by the use of a fictitious element impedance boundary condition, which remedies the skin depth issue associated with volumetric metallic microwave FE modeling. Owing to a mixture of the numerically large values of good conductors and the element impedance condition, the design method cannot be used to distinguish between, e.g., silver and copper but should only be used to model conductor and no conductor. The proposed set of interpolation functions showed that the threshold value of the conductivity for the electric field was of the order $\sigma^{\mathrm{m}}_{\mathrm{E}_{\mathrm{cutoff}}} \approx 10^7\,\mathrm{S/m}$ whereas $\sigma^{\mathrm{m}}_{\mathrm{H}_{\mathrm{cutoff}}} \approx 10^6\,\mathrm{S/m}$ for the magnetic field.

The design method is demonstrated to work for both field formulations of Maxwell's equations and, in conjunction with a design variable filter, is shown to yield mesh- and field-type independent designs. The optimized designs are validated by a postprocessing in which the designs are rendered fully 0–1 and analyzed using the PEC condition. The post processed designs showed good agreement with the optimized designs. However, in some cases a shift of up to 4% in target frequency was found after postprocessing, which is contributed to the presence of gray elements in the optimized design. This means that the proposed design method could advantageously be combined in a two step approach, in which the second step would be to apply shape optimization to the optimized design in order to fine tune the system response using, e.g., an iso-geometric design scheme [27].

The implementation of the proposed design parameterization into existing high-level FE software, such as Comsol Multiphysics [28], is not straightforward, since it requires the integration along element boundaries. However, if access to element normals and shape functions is available the implementation can be done following the outline of this paper.

Future works include the development of an efficient 3D parallel FE code to be used for conformal antenna design and the design of magnetic resonators for wireless energy transfer.

ACKNOWLEDGEMENTS

This work is supported by the Danish National Advanced Technology Foundation through the grant *Wireless Coupling in Small Autonomous Apparatus* (www.hoejteknologifonden.dk), by the Eurohorcs/ESF European Young Investigator Award (EURYI, www.esf.org/euryi) through the grant *Synthesis and topology optimization of optomechanical systems* and by the Danish Center for Scientific Computing (www.dcsc.dk). The authors would finally like to extend their gratitude to the partners at the Danish Institute of Technology and the research groups TopOpt and TopAnt at the Technical University of Denmark for many useful and enlightening discussions.

REFERENCES

1. Kurs A, Karalis A, Moffatt R, Joannopoulos JD, Fisher P, Soljacic M. Wireless power transfer via strongly coupled magnetic resonators. *Science* 2007; **317**(5834):83–86.
2. Intel Corporation. Wireless energy transfer, 2008. Available from: http://dvice.com/archives/2008/08/intel_wireless.php.
3. Bombardier Inc. PriMove, 2008. Available from: http://www.bombardier.com/en/transportation/sustainability/technology/primove-catenary-free-operation.
4. Balanis CA. *Antenna Theory*: *Analysis and Design* (3rd edn). Wiley: New York, 2005.

DOI: 10.1002/nme

5. Bendsøe MP, Sigmund O. *Topology Optimization—Theory, Methods and Applications*. Springer: Berlin, 2003.
6. Bendsøe MP, Kikuchi N. Generating optimal topologies in structural design using a homogenization method. *Computer Methods in Applied Mechanics and Engineering* 1988; **71**:197–224.
7. Kiziltas G, Kikuchi N, Volakis JL, Halloran J. Topology optimization of dielectric substrates for filters and antennas using SIMP. *Archives of Computational Methods in Engineering* 2004; **11**(4):355–388.
8. Borel PI, Harpth A, Frandsen LH, Kristensen M, Shi P, Jensen JS, Sigmund O. Topology optimization and fabrication of photonic crystal structures. *Optical Express* 2004; **12**:1996–2001.
9. Jensen J, Sigmund O. Systematic design of photonic crystal structures using topology optimization: low-loss waveguide bends. *Applied Physics Letters* 2004; **84**(12):2022–2024.
10. Svanberg K. The method of moving asymptotes—a new method for structural optimization. *International Journal for Numerical Methods in Engineering* 1987; **24**:359–373.
11. Erentok A, Sigmund O. Three-dimensional topology optimized electrically small conformal antenna. *IEEE AP-S International Symposium on Antennas and Propagation and USNC/URSI National Radio Science Meeting*, San Diego, CA, U.S.A., 5–12 July 2008.
12. Jin J. *The Finite Element Method in Electromagnetics* (2nd edn). Wiley: New York, 2002.
13. Borrvall T, Petersson J. Topology optimization of fluids in Stokes flow. *International Journal for Numerical Methods in Fluids* 2003; **41**:77–107.
14. Koulouridis S, Psychoudakis D, Volakis JL. Multiobjective optimal antenna design based on volumetric material optimization. *IEEE Transactions on Antennas and Propagation* 2003; **55**(3):594–603.
15. Balanis CA. *Advanced Engineering Electromagnetics* (1st edn). Wiley: New York, 1989.
16. Zhu Y, Cangellaris A. *Multigrid Finite Element Methods for Electromagnetic Field Modeling* (1st edn). Wiley: New York, 2006.
17. Bendsøe MP. Optimal shape design as a material distribution problem. *Structural Optimization* 1989; **1**:193–202.
18. Jensen J, Sigmund O. Topology optimization of photonic crystal structures: a high-bandwidth low-loss T-junction waveguide. *Journal of the Optical Society of America* 2005; **22**(6).
19. Sigmund O, Hougaard K. Geometric properties of optimal photonic crystals. *PRL*, vol. 100(15). The American Physical Society, 2008. Article No. 153904.
20. Diaz AR, Sigmund O. Negative permeability metamaterial design by topology optimization. *Structural and Multidisciplinary Optimization* 2009; **41**:163–177.
21. Bourdin B. Filters in topology optimization. *International Journal for Numerical Methods in Engineering* 2001; **50**(9):2143–2158.
22. Bruns TE, Tortorelli DA. Topology optimization of nonlinear elastic structures and compliant mechanisms. *Computer Methods in Applied Mechanics and Engineering* 2001; **190**(26–27):3443–3459.
23. Sigmund O. Morphology-based black and white filters for topology optimization. *Structural and Multidisciplinary Optimization* 2007; **33**:401–424.
24. Geuzaine C, Remacle JF. GMSH, version 2.3.1, 2009. Available from: http://www.geuz.org/gmsh/.
25. Guest J, Prevost J, Belytschko T. Achieving minimum length scale in topology optimization using nodal design variables and projection functions. *International Journal for Numerical Methods in Engineering* 2004; **61**(2): 238–254.
26. Jin J, Riley DJ. *The Finite Element Analysis of Antennas and Arrays* (1st edn). Wiley: New York, 2008.
27. Cottrell JA, Reali A, Bazilevs Y, Hughes TJR. Isogeometric analysis of structural vibrations. *Computer Methods in Applied Mechanics and Engineering* 2006; **195**:5257–5296.
28. Comsol Multiphysics, Reference Manual for Comsol 3.4. COMSOL AB, Stockholm. Available from: www.comsol.se.

DOI: 10.1002/nme

Publication [P2]

Parallel multiphysics topology optimization using the method of moving asymptotes

Noname manuscript No.
(will be inserted by the editor)

Parallel multiphysics topology optimization using the method of moving asymptotes

Niels Aage · **Boyan S. Lazarov**

Received: date / Accepted: date

Abstract The complexity of the problems attacked in topology optimization has increased dramatically during the past decade. Examples include fully coupled multiphysics problems in thermo-elasticity, fluid-structure interaction, Micro-Electro Mechanical System (MEMS) design and large-scale three dimensional problems. The only feasible way to obtain a solutions within a reasonable amount of time is to use parallel computations in order to speed up the solution process. The focus in this article is on a fully parallel topology optimization framework implemented in C++. The code is developed to be easily extendable in terms of physical models as well as in terms of solution methods, without compromising the parallel scalability. The widely used Method of Moving Asymptotes optimization algorithm is parallelized and included as a fundamental part of the code. The capabilities of the presented approaches are demonstrated on topology optimization of a Stokes problem with target outflow constraints as well as the minimum compliance problem with a volume constraint from linear elasticity.

Keywords Topology optimization · method of moving asymptotes · parallel computing · multiphysics problems

The authors acknowledge the support of the Danish National Advanced Technology Foundation, the Danish Center for Scientific Computing, the CSC supercomputer center in Finland, and the Elite Research Prize from the Danish Minister of Research.

N. Aage · B.S. Lazarov
Department of Mechanical Engineering, Solid Mechanics,
Technical University of Denmark, Nils Koppels Alle, B.404,
DK-2800 Kgs. Lyngby, Denmark
E-mail: naa@mek.dtu.dk

1 Introduction

The main motivation for the presented work is the desire to have an easily extendable topology optimization code capable of solving large-scale multiphysics problems. An object oriented design ensures flexibility of the code. The implementation utilizes C++ (e.g. Stroustrup, 1997) as a programming language and the parallelization is based on the Message-Passing Interface (MPI) (e.g. Gropp et al, 1999).

Previous work on parallel topology optimization is fairly sparse and consists of contributions from (Borrvall and Petersson, 2001), (Kim et al, 2004), (Vemaganti and Lawrence, 2005), (Mahdavi et al, 2006), (Aage et al, 2008) and (Evgrafov et al, 2008). The limited number of publications on the subject is, as also noticed in (Evgrafov et al, 2008), not in line with the development seen in e.g. fluid mechanics where the publications on parallel computing is plentiful. Recently, in (Wadbro and Berggren, 2009) and (Schmidt and Schulz, 2009) GPU's have been used to parallelize optimization problems in heat conduction and linear elasticity, respectively. It is noticed that most of the mentioned publications describe problem specific implementations of a given optimization problem and/or linear solver. In the work presented here, the focus is on the development of a general purpose framework, capable of solving *any* large-scale, or multiphysics, PDE constrained topology optimization problem.

The subject of flexible and easily extendable codes is addressed in Borrvall and Petersson (2001), in which the authors also deals with the issue of flexibility vs. performance. That is, the use of an easily maintainable programming language such as C++, results in a code that will execute slower than e.g. an equivalent and dedicated C/Fortran code. Speed can be regained by careful design of the operations and using dedicated mathematical libraries. Clearly, using higher

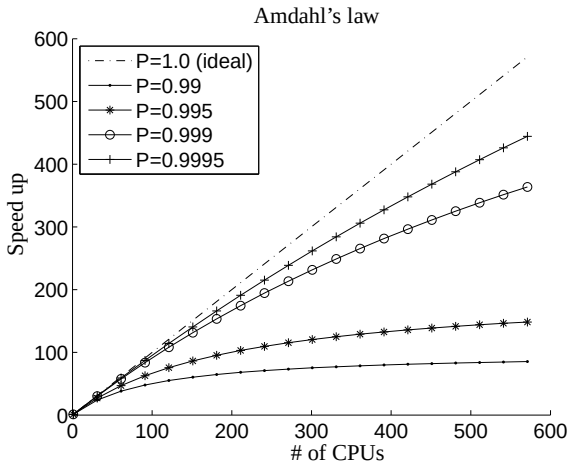

Fig. 1 Amdahl's law for parallel speedup.

abstraction comes at a cost and minimizing it is discussed in the following text.

An important aspect when writing a parallel code is to ensure that the entire program is parallelized. This can be illustrated through Amdahl's law (Amdahl, 1967) which, amongst others, provides a simple model for the parallel speed up, S, as a function of the number of CPUs, N, and the percentage, P, of the program that is parallelized. The law can be stated as

$$S = \frac{1}{1 - P + \frac{P}{N}} \tag{1}$$

A plot of Amdahl's law for different percentages of scalability can be seen in figure 1. In standard topology optimization problems the majority of the computational effort is spent on solving the state problem and usually less than one percent in the optimizer. Therefore it might seem like a fruitful idea to parallelize only the state solver. However, inspection of figure 1 reveals that this can be a potentially critical decision even if only 0.05% of the computational time is spent within the optimizer. For this example Amdahl's law predict that using 600 CPUs will only lead to a speed up of 400. Thus, to ensure that the code is truly scalable everything must be parallelized.

The paper is divided into two main parts. The first part consists of the development of a framework in which partial differential equations can efficiently be implemented and solved by any discrete scheme e.g. the finite element (FEM), finite volume (FVM) or finite difference (FD) methods. The second part gives details about parallelizing the optimizer. Here the Method of Moving Asymptotes (MMA) (Svanberg, 1987) has been chosen. The reason for this choice is first and foremost that the method has been demonstrated to work very well on a vast variety of topology optimization problems (Bendsøe and Sigmund, 2004). Secondly the method is very attractive for parallel computations due to the separable nature of the approximations. It should of course be mentioned that by choosing MMA as the optimizer one must accept that the optimization problems are restricted to problems with relatively few constraints. Finally, numerical examples which demonstrate the capabilities of the parallel optimization framework are presented and the findings are concluded.

2 The parallel optimization framework

The parallel optimization framework DFEM is developed over the last 3 years using ideas presented in Lazarov and Augarde (2005). The code is based on object oriented programming concepts, which allows for easy maintainability, extendability and clear communication interface both between the different objects and between the processes working in parallel. Each of these three points are discussed in details in the upcoming section, and is followed by an explanation of the steps required to implement a topology optimization problem within the parallel framework.

2.1 The object oriented approach and parallelism

An object is a basic building block for every object oriented program, and it encapsulates data structures and the operations defined over the data. The actual data structures are often hidden from the rest of the code and access to them is granted by clearly defined interfaces. The concept is exemplified here by using sparse matrices arising from some numerical discretization procedure like finite elements, finite difference, finite volume, etc. A sparse matrix can be stored in the computer memory by using several storage format, e.g. compressed sparse row (CSR) or coordinate format (COO) (e.g. Davis, 2006). These formats minimize the stored information by neglecting all zeros in the matrix. A large number of the freely available sparse solvers requires the matrices to be supplied to them in some of these formats. In order to speed up the mathematical operations, i.e. the memory access, the data structures are static and not suitable for dynamic expansion. During the assembly process new element entries are often added to the matrix and dynamic structures like lists or trees are more suitable for representing the matrix storage. On the other hand dynamic structures perform poorly on operations such as matrix vector products, which are required by every iterative solver. Both static and dynamic structures have advantages and disadvantages and implementing only one of them would compromise either the mathematical or the assembly operations. An object can easily hide the storage representation from the user and it can implement both dynamically growing assembly efficient storage and computationally effective static sparse storage. Conversion between them can be performed

quietly, without explicit user interaction, before the first matrix vector product. An object is controlled by its methods which for sparse matrix can be

```
AddValue(i,j,a)
```

for adding values, where `i,j` denote the coordinates and `a` the actual value. The method for sparse matrix vector product can be defined as

```
MatVecProd(Vector Vinp, Vector Vout)
```

where `Vector Vinp` is an object representing the input vector in the operation and `Vout` is the resulting vector. Adding a new sparse matrix representation to an object oriented code is relatively easy. The new class can either inherit the interface from the previous and redefine the methods, or both sparse matrix classes can inherit a common pure virtual class in the C++ terminology, which define only the interface without specifying any data storage representation. In the first case the class can inherit the storage data structures from the initial sparse matrix class. For the rest of the code, object realizations from both classes are accessed through the defined interface and changes are not required for utilizing the new sparse matrix implementation.

The sparse matrix example, although incomplete demonstrates the basic features of object oriented (OO) programming. Well developed OO code can be easily extended by inheriting clearly defined interfaces. Furthermore it is easy to maintain, as adding a new class doesn't require changes in the other classes which communicate with object through the predefined class interface. Improperly defined interfaces make modifications of the original code extremely difficult. The first step in the design of an OO program or library, is identification and definition of the common interface between the different objects and their relations. For example using the above methods for controlling sparse matrix classes make the objects suitable for finite element discretization, finite volume and finite difference schemes. In FEM each element stores its contribution to the global tangent matrix (sparse matrix) by calling `AddValue(i,j,a)` for each entry in the local element matrix. An equivalent operator can be defined for each finite volume or finite difference stencil. Cycling through the elements, the finite volumes or the collocation points assembles the global matrix. One disadvantage in such an assembly process is that the sparse matrix abstraction might introduce additional overhead on the operations. This overhead is multiplied by the number of elements, the volumes or the collocation points. Speed up can be achieved by defining super elements, super volumes or super stencils and defining the method to work over arrays, i.e. `AddValues(n,i[],j[],a[])` where `i[],j[],a[]` are arrays with the entries indices and values and `n` is their size. Using the above methods for defining an interface to a sparse matrix makes the code practically independent from the sparse storage and its allocation. The program can handle several discretization schemes without significant changes. In the DFEM the object oriented ideas are applied not only to the mathematical objects but also for representing the elements, the computational domains, the material properties and the geometry.

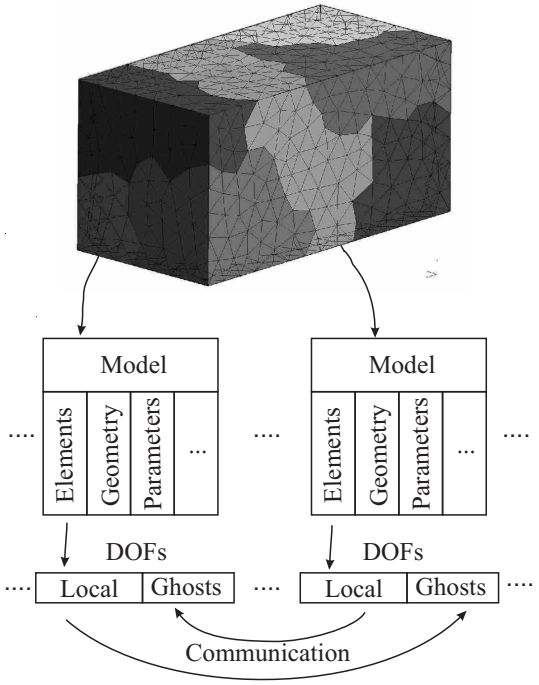

Fig. 2 DFEM framework applied in the assembly of a distributed vector.

The DFEM model, illustrated in Figure 2, consists of four object databases - one for the geometric objects, one for material objects, one for element objects and one for solution parameter objects. Search in these databases is performed by using a unique global ID assigned in advance to the objects or unique internal ID assigned when an object is added to the model. The internal ID doesn't require any search to be performed as it directly gives the position of the object in the memory, the global ID is used to define relations between the object in the input files. All matrix and vector objects are assembled by cycling thought the objects in the element database. The overhead due to the higher abstraction can be reduced by defining super elements or subdomains. The geometry database consists of nodes and their main task is to administrate the associated degrees of freedom. The degrees of freedom are assigned to the nodes in an initial step by the elements. Each node holds a table which relates a degree of freedom with a global number used in the matrix and the vector assembly process. Dynamical allocation of these tables allows different number of the degrees to be assigned per node and therefore the code is eas-

ily extendable to work with many physical fields and solve mixed problems in physics, e.g. fluid structure interaction or thermo-mechanics. For problems with weakly coupled fields more tables can be added for each of the addressed physical problems. Such an approach allows for splitting one big problem into several smaller by decoupling them.

Using the OO approach simplifies the linear system solver interface. DFEM works with both direct and iterative methods. Iterative methods (e.g. Saad, 2003) are preferable in parallel computing due to the lower amount of communications. They require the matrix vector product operation to be defined for the discretized differential operators. In order to speed up the convergence a good preconditioner for the physical problem needs to be derived. General preconditioners such as incomplete factorization or inverse sparse approximate inverses applicable for a broad range of matrices are implemented as well. The construction of these general preconditioners is speed-up by exploiting the different sparse matrix storage schemes. Direct solvers can be viewed as the perfect preconditioner and therefore they can be implemented using the same object oriented interface. Several freely available solvers UMFPACK (Davis and Duff, 1997; Davis, 2006), SuperLU, MUMPS (Amestoy et al, 2000), are interfaced and used in the program.

The defined objects and hierarchy between them simplify significantly the communication interface. The communications are based on messages by using the Message Passing Interface (MPI) and they are performed on database level. Each of the defined four databases communicates with the corresponding one located on different processes. In order to hide the latency in the communications the data transfer is split in two parts: first initiation of the data transfer and second completion of the data transfer. In the initial phase all messages are posted using non-blocking send mechanism provided by MPI. Once the communications are initiated some local computations which do not require data exchange are performed allowing the messages to arrive to the destinations. The completion step is used to ensure that the data has arrived safely and to free any memory associated with the operation. In order to ensure good scalability, the communication pattern is not required to be regular. Scalability can be achieved if the local computations time is larger than the time necessary for data exchange.

All of the described structures can be used in the solution process of every PDE problem discretized in DFEM. Introducing a new physical problem in the framework requires the implementation of new element class which defines the element topology, interpolation and PDE operator discretization. The boundary conditions are represented as elements also and they can be implemented by using either penalty or Lagrange multiplier methods. Any global operation such as removing or modifying a matrix row or column

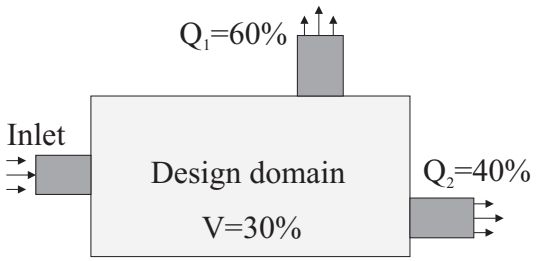

Fig. 3 Problem sketch for a flow problem. The dark grey regions corresponds to inlets and outlet and the light grey region to the design domain. The objective is to minimize the pressure drop subject to a 30% volume constraint. Constraints on the mass flow at outlet 1 and 2 are set to 60% and 40%, respectively, of the total inflow.

for imposing boundary conditions is undesirable. It imposes order in the operations which limits the parallelism.

In order to minimize the communication cost the computational domain is spit into several sub-domains by using graph partitioning library METIS (Karypis and Kumar, 1999). The partitions are used as a base for creating input files for each process which can be read and parsed independently on each of them. The original mesh is generated by using GMSH (Geuzaine and Remacle, 2009) or CUBIT, and ParaView is used for visualization of the presented results.

2.2 Implementing a topology optimization problem

The implementation of any given topology optimization problem within the parallel framework follows the two steps which are presented in this section. The procedure is exemplified on the Stokes flow optimization problem illustrated in figure 3. The goal is to minimize the pressure drop, subject to a 30% volume constraint as well as constraints on the mass flow at outlet 1 and 2. Though the flow problem is not a multiphysics problem it requires the definition of two state fields, velocity and pressure, and thus has the same characteristics as a fully coupled problem e.g. a saddle point system with large bandwidth of the system matrix.

The first step in the implementation is to create the elements needed for solving the state and optimization problem. This includes the discretization of the PDE as well as the objective, constraints and sensitivities for the optimization problem. Within the C++ framework an element class follows a predefined, yet versatile, interface, i.e. utilizing the concept of inheritance and virtual methods. The user only has to define the methods which are relevant to the specific element, while all other methods can be left empty. This is best illustrated with the example problem of figure 3. To solve this problem a total of 5 elements must be written, i.e. two volumetric elements and three boundary condition elements. The first volume element solves the flow problem alone and is used in the inlet and outlets. This element only

requires three methods to be specified; `read()` to parse input from the input file, `SetDOF()` for setting the DOFs and `SetMat()` to compute and add element contributions to the global tangent matrix. The second volume element solves the flow problem inside the design domain. Besides the three methods mentioned before, this element also requires additional optimization methods to be defined, i.e. methods that returns the objective, constraints and sensitivities. The last three elements are boundary elements which corresponds to inlet, outlet and a no-slip boundary conditions respectively. The methods for these elements follow the same logic as the two previously described.

Thus, implementing any given PDE constrained optimization problem within the framework only requires that the user can express the PDE problem in a discrete form, e.g. finite element form, and provide expressions for the objective, constraints and sensitivities. The user is not required to poses knowledge about parallel communications and partitioning, mesh and node tables, DOF numbering, assembly procedures, etc. So even though the framework is not intended for high-level use, such as e.g. Comsol Multiphysics, the approach for implementing a new physical or multiphysical problem is similar.

The second and the final step of the implementation is to create a driver program that performs the actual optimization task. The driver has the same structure as the topology optimization flowchart for the considered problem. For the Stokes flow problem the flowchart, and thus the driver, can be stated as

1 Initialize problem parameters and call `SetDof()`
2 Declare the matrix, vector and optimization structures and choose the linear solver (and preconditioner) for the state and adjoint problems.
3 Loop until convergence:
   – Assemble and solve the state problem.
   – Compute objective and constraints.
   – Solve adjoints and compute sensitivities.
   – Update design and check for convergence.
4 End

Of course, the practical realization of the driver requires a few more lines of code to be written, but the overall structure is as stated above.

3 Parallel generation and solution of the MMA sub-problem

This section introduces a general optimization problem which can be solved using the presented parallel framework. An inequality constrained optimization problem can be stated as

$$\begin{aligned} \min_{x\in\mathbb{R}^n} \quad & g(x) \\ \text{s.t.} \quad & g_i(x) \leq 0, \qquad i = 1,m \\ & x_{\min} \leq x_j \leq x_{\max}, \; j = 1,n \end{aligned} \tag{2}$$

where n is the number of design variables and m is the number of constraints. We assume that the functions g and g_i are smooth and both non-linear and non-convex. It is difficult to directly attack problems in the form stated in eq. (2). A well established approach for the solution to the non-linear programming problem given by eq. (2) is to generate and solve a series of approximate sub-problems. This type of solution strategy is considered in MMA.

3.1 The MMA sub-problem

The idea behind MMA, as well as behind other optimization methods such as CONLIN (Fleury, 1993) or sequential quadratic programming (SQP), see e.g. Andrasson et al (2005), is to solve a series of approximate sub-problems instead of the original non-linear problem. This means that the functions $g(x)$ and $g_i(x)$ in eq. (2) are approximated by some appropriate function. To obtain a well-posed optimization problem the approximations are required to be convex. An example of such approximations is the Taylor expansions used in SQP methods. Since the approximation is valid only in the vicinity of the expansion point, the process of generating and solving a sub-problem must be repeated and thus a sequence of solutions x^k is produced, where k is an iterate counter. The procedure is repeated until a specified convergence criteria is fulfilled.

In MMA the approximations are based on convex functions of the type

$$f_i(x) = \sum_{j=1}^{n} \left(\frac{p_{ij}}{U_j - x_j} + \frac{q_{ij}}{x_j - L_j} \right) + r_i \tag{3}$$

where U and L are the upper and lower asymptote responsible for (half of) the name of the method. The coefficients and asymptotes, i.e. p_{ij}, q_{ij}, r_i, U, L, are updated at each iteration based on the current design variables at x^k, the function values evaluated at x^k, i.e. $g(x^k)$ and $g_i(x^k)$, as well as the sensitivities $\partial g(x)/\partial x_j$ and $\partial g_i(x)/\partial x_j$. If available the design history is also used. The expressions for generating the coefficients of the MMA sub-problem are described in detail in Svanberg (1987) and Svanberg (2002). The latter contains a globally convergent version of MMA which is not implemented in the parallel framework presented here. However, the modification to the asymptote updates presented in Svanberg (2002) are incorporated since this leads to better performance of the method.

The MMA sub-problem utilizes artificial, or "elastic", variables to ensure that the sub-problem always has a feasible solution. The inclusion of elastic variables consists of modifying the inequality constraints by the subtraction of an extra variable, i.e. $y_i \geq 0$. The elastic variables are included to provide more freedom for the optimizer. An example of their importance is the case where a feasible starting guess x^0 is not available. In such cases the MMA sub-problem can still be solved and the solution at x^k can be interpreted as an iterate that is as close to being feasible as possible (Svanberg, 1987). Since such variables are artificial they should be zero in the final solution, and therefore they are added to the objective, penalized by some large number c_i.

The most common formulation of the MMA sub-problem also includes an additional extra variable, z, which can be used to solve non-smooth problems such as min-max problems. Such a variable is also included in the implementation presented here.

By summarizing the above ideas, the MMA sub-problem can be stated as

$$\begin{aligned} \min_{x\in\mathbb{R}^n, y\in\mathbb{R}^m, z\in\mathbb{R}} \quad & f_0(x) + z + \tfrac{1}{2}z^2 + \sum_{i=1}^{m}\left(y_i c_i + \tfrac{1}{2}y_i^2\right) \\ \text{s.t.} \quad & f_i(x) - a_i z - y_i \leq 0,\ i = 1,m \\ & \alpha_j \leq x_j \leq \beta_j,\ \ j = 1,n \\ & y_i \geq 0,\ \ i = 1,m \\ & z \geq 0 \end{aligned} \tag{4}$$

The quadratic terms for z and y_i are necessary when a dual method is used for solving the sub-problem, but could be omitted for a primal approach. An important result (Svanberg, 1987) is that if the constants c_i are chosen sufficiently large, it can be proved that the elastic variables will be zero in the optimal solution to eq. (4). This, of course, only holds if there exists a feasible solution to the original problem (2).

The approximations in MMA are both convex and separable. The convexity ensures that the sub-problem in eq. (4) can be solved and the separability that the Hessian wrt. x forms a diagonal matrix (Luenberger and Ye, 2008). Furthermore, the separability makes dual approaches very attractive since the dual function can be stated explicitly without significant difficulties (Svanberg, 1987).

The MMA sub-problem can be solved using several different approaches. Within the presented C++ framework we have implemented both a primal/dual and a dual solver. A primal/dual solver solves the subproblem for both the primal variables, i.e. x, y and z, as well as for the set of Lagrange multipliers corresponding to the constraints. The Lagrange multipliers are here termed dual variables (Andrasson et al, 2005). A dual method consist of rewriting the optimization problem in eq. (4) as a problem in terms of the Lagrange multipliers alone.

3.2 The dual solver

In the presented optimization framework the dual of the MMA subproblem, eq. (4), is solved using an interior point method. The first step in constructing the solver is to obtain the dual of the MMA subproblem in eq. (4). This is achieved by forming the augmented Lagrangian, L, i.e.

$$\begin{aligned} L(x,y,z,\lambda) = & \sum_{j=1}^{n}\left(f_0(x_j) + \sum_{i=1}^{m}\lambda_i f_i(x_j)\right) \\ & + z + \tfrac{1}{2}z^2 - \sum_{i=1}^{m}(\lambda_i a_i z) \\ & + \sum_{i=1}^{m}\left(y_i c_i + \tfrac{1}{2}y_i^2 - \lambda_i y_i\right) \Rightarrow \\ L(x,y,z,\lambda) = & L_x(x,\lambda) + L_z(z,\lambda) + L_y(y,\lambda) \end{aligned} \tag{5}$$

where the terms are organized to illustrate the separability of the subproblem and $\lambda_i \geq 0$, $i = 1,m$ are Lagrange multipliers for the non-linear inequality constraints.

The Lagrangian dual, $\Psi(\lambda)$, is then formed by solving the following sequence of simple minimization problems.

$$\begin{aligned} \Psi(\lambda) = & \sum_{j=1}^{n}\left(\min_{x_j}\{L_x(x_j,\lambda) | \alpha_j \leq x_j \leq \beta_j\}\right) \\ & + \min_{z}\{L_z(z,\lambda) | z \geq 0\} \\ & + \sum_{e=1}^{m}\left(\min_{y_i}\{L_y(y_i,\lambda) | y_i \geq 0\}\right) \end{aligned} \tag{6}$$

As a natural part of these calculations one obtains explicit expressions for $x_j(\lambda)$, $y_i(\lambda)$ and $z(\lambda)$. Upon reinsertion of these into eq. (6) the dual problem can be stated as the following maximization problem

$$\begin{aligned} \max_{\lambda\in\mathbb{R}^m} \quad & \Psi(\lambda) \\ \text{s.t.} \quad & \lambda_i \geq 0,\ i = 1,m \end{aligned} \tag{7}$$

Since the dual function is concave the maximization problem in eq. (7) is convex (Andrasson et al, 2005). When the solution to the dual problem is obtained, the optimal primal solution can be computed by reinserting the optimum λ^* into the expression for $x_j(\lambda)$, $y_i(\lambda)$ and $z(\lambda)$. This is a direct consequence of the convexity of the MMA subproblem and thereby the zero duality gap which follows from the strong duality theorem (Luenberger and Ye, 2008). As already mentioned, there exist several solution strategies for solving the optimization problems of the type stated in eq. (7). Here the primal/dual approach is chosen, which means that another augmented Lagrangian has to be formed, i.e.

$$\Phi(\lambda,\eta) = \Psi(\lambda) + \eta^T\lambda \tag{8}$$

$\eta \in \mathbb{R}^m$ is a vector of Lagrange multipliers and the conditions $\eta_i \geq 0$ and $\lambda_i \geq 0$ for $i = 1,m$ are required to be fulfilled. Note that the primal/dual type solver now refers to λ

as the primal variables and η as the dual variables, and not to the primal and dual variables of the MMA subproblem. The first order optimality conditions, i.e. the Karush-Kuhn-Tucker (KKT) conditions (Andrasson et al, 2005), can be stated as

$$\begin{aligned} \nabla\Psi(\lambda)+\eta &= 0 && \text{(stationarity)} \\ \eta_i\lambda_i &= 0, \quad i=1,m && \text{(compl. slackness)} \\ \eta_i &\geq 0, \quad i=1,m && \text{(dual feasibility)} \\ \lambda_i &\geq 0, \quad i=1,m && \text{(primal feasibility)} \end{aligned} \tag{9}$$

The above system is then solved by an interior point method. The solution process involves adding a penalty parameter μ to the right hand side of each of the complementary slackness conditions, such that the conditions now read $\eta_i\lambda_i = \mu$. The modification of the complementary slackness conditions is equivalent to the optimization problem arising from adding a logarithmic barrier, i.e. $\mu\sum_{i=1}^{m}\log(\eta_i)$, to the dual function, and interpreting $\eta_i > 0$ as a slack variable (Andrasson et al, 2005). The modified KKT system can then be solved by Newton's method. The resulting linearized system has size $2m \times 2m$. Taking the Schur complement it can be written as a $m \times m$ system of the form

$$\left[\nabla^2\Psi(\lambda) - \Omega\Lambda\right]\Delta\lambda = -\nabla\Psi(\lambda) - \mu\Lambda e \tag{10}$$

where Λ and Ω are diagonal matrices with $\frac{1}{\lambda_i}$ and η_i on the diagonal, respectively, and e is a vector of ones. The search direction for η can then be found as

$$\Delta\eta_i = -\eta_i + \frac{\mu}{\lambda_i} - \Delta\lambda_i\frac{\eta_i}{\lambda_i} \tag{11}$$

Based on the computed search direction a line-search is performed such that the step leaves all η's and λ's strictly positive. This requirement is equivalent to finding the maximal $\theta \leq 1$ such that

$$\lambda_i + \theta\Delta\lambda_i \geq 0.01\lambda_i$$
$$\eta_i + \theta\Delta\eta_i \geq 0.01\eta_i$$

for all $i = 1,m$. When $\theta = 1$ this corresponds to a full Newton step. Each barrier problem is solved to a tolerance such that the infinity norm of the KKT residual is less than 0.9μ, i.e. $||\text{KKT}||_\infty < 0.9\mu$, after which μ is reduced by a factor of ten. This is continued until $\mu < 10^{-7}$.

Finally to ensure robustness of the implementation, the Hessian is updated by adding a scaled identity matrix to the Hessian, i.e. γI. The parameter γ can be determined by application of the Levenberg-Marquardt algorithm (Andrasson et al, 2005), or by a heuristic update. In the presented implementation a heuristic update is used such that γ is chosen as the maximum value of $10^{-5}\,tr(\text{Hessian})$ or 10^{-7}. In addition to the heuristic update of the Hessian it is required that the search direction is in fact an ascent direction. This requirement is fulfilled when the inner product between the search direction and the gradient of eq. (8) is larger than zero. These checks should then ensure positive definiteness of the Hessian and that the search direction is always an ascent direction.

3.3 Parallel considerations

The parallel implementation of the dual solver is based on a decomposition of the computational domain, c.f. the parallel approach described in section 2.1. The distribution of the primal variables x, their bounds and the sensitivities of the objective and the constraints follow directly form this decomposition. The values of the constraints and objective are global parameters as they are, in general, global measures of the system performance. Hence, it is natural to assume y, z, λ and η to be global variables receiving contribution from all computationally active sub-domains. A local copy of these variables is kept on each process and the copy is updated through the communication required for the primal variables and bounds. This means that the fully populated KKT system is solved simultaneously on all processors. This fact is also the main reason as to why this optimizer only works efficiently for a small number of constraints, i.e. $m < 1500$.

In the following the different parts of the dual solver will be illuminated wrt. its parallelization.

Generating the MMA subproblem is almost embarrassingly parallel. The only information which need to be communicated is the correction terms r_i from eq. (3).

As already mentioned the solution to the Newton system, eq. (10), is done locally and does not require any communications. This however, is not the case for its assembly. Both the Hessian and the gradient, i.e. $\nabla^2\Psi(\lambda)$ and $\nabla\Psi(\lambda)$, depends on x and therefore requires communication. In order to quantify the parallel complexity associated with the assembly of the Hessian and gradient, it is necessary to examine how they are formed in details. Using results from Lagrangian duality (Luenberger and Ye, 2008) the Hessian and gradient can be computed as follows

$$\nabla\Psi(\lambda) = h \tag{12}$$

$$\nabla^2\Psi(\lambda) = -\nabla h^T[\nabla^2 L]^{-1}\nabla h \tag{13}$$

where the differentiation is with respect to x, y and z and the Lagrangian, L, is given in eq. (5). The vector h consists of the constraints of the MMA subproblem, eq. (4), i.e.

$$h_i = h_i(x(\lambda), y(\lambda), z(\lambda)) \tag{14}$$
$$= f_i(x(\lambda)) - a_i z(\lambda) - y_i(\lambda)), \quad i = 1,m \tag{15}$$

The evaluation of the gradient $\nabla\Psi(\lambda)$ only requires communication for the terms $f_i(x(\lambda))$.

The assembly of the Hessian for the dual problem can be easily implemented using for-loops. However, to obtain an efficient parallel implementation it is convenient to assemble the matrices ∇h and $\nabla^2 L$ separately, and then compute the Hessian through matrix-matrix operations. Both of these assemblies are local operations, which can be seen from their expression for the x-dependent terms

$$\nabla_x h_{ij} = \frac{p_{ij}}{(U_j - x_j(\lambda))^2} - \frac{p_{ij}}{(x_j(\lambda) - L_j)^2}$$
$$\nabla_x^2 L_{jj} = \frac{2\left(p_{0j} + \sum_{i=1}^{m} \lambda_i p_{ij}\right)}{(U_j - x_j(\lambda))^3} + \frac{2\left(q_{0j} + \sum_{i=1}^{m} \lambda_i q_{ij}\right)}{(x_j(\lambda) - L_j)^3}$$

Since only the part of the Hessian that depends on x requires communication, the expressions for $\nabla_z^2 \Psi(\lambda)$ and $\nabla_y^2 \Psi(\lambda)$ are not presented here. The presented approach requires communication for performing the matrix-matrix product. Note that the inversion of the matrix $\nabla_x^2 L$ is, of course, only practically possible due to the separable nature of the MMA approximations, i.e. it forms a diagonal matrix. Also it should be noted that the differentiation must take into account whether or not the primal variables have reached their bounds since they are now functions of λ. This means that a bounded variable will not contribute to the Hessian since it is constant wrt. λ. To avoid too many if-statements, the check for bounded x_j can efficiently be done only for the $\nabla_x^2 L$ term.

With regards to the full parallel implementation it is noticeable that *all* operations that require communication can be cast in the form of matrix-vector or matrix-matrix operations. These types of operations are desirable in terms of parallel performance since the relation between computations and communications are in favor of the computations, as opposed to e.g. max and min operators. In fact, for a single Newton iterate communications are only required once for the gradient evaluation, once for the Hessian and once for the KKT residual. The line-search and the computation of the primal variables are completely local.

The other solver in our C++ framework. i.e. the interior point primal/dual method for eq. (4), has higher communication complexity. This is a result of working directly with the primal variables and their associated Lagrange multipliers. This means, for example, that computing the step length requires the use of several max operators which increases the number of barriers. Hence, from a parallel point of view, the dual solver is more attractive.

4 Numerical examples

In this section the capabilities and shortcomings of the already discussed C++ optimization framework are presented with regard to parallel performance by solving known topology optimization problems from fluid and solid mechanics. For the topology optimization examples the design problems are meshed using Cubit and the domain decomposition is obtained using METIS (Karypis and Kumar, 1999). The post-processing is performed in Paraview.

4.1 MMA convergence and general scalability

A verification of the implemented MMA dual solver can be obtained by checking the convergence rate for a fixed barrier parameter μ. According to theory (Andrasson et al, 2005) the convergence of the Newton solver should be 2nd order when close to an optimum. A plot of the convergence is given in figure 4. Note that each barrier problem in figure 4 is solved to a tolerance of 10^{-14} as opposed to the tolerance suggested in section 3.2.

To measure the parallel speed up, and thus the scalability, for the MMA implementation as well as the entire parallel PDE and optimization framework, we use the relative speed up. The relative speed up can be expressed as the ratio of CPU time spend on N CPUs to the CPU time spend on minimum number of CPUs the problem allows us to use. This measure is used since large problems cannot be run on a single, or even several CPUs, mainly due to memory limitations.

The parallel scalability of the C++ framework is shown in figure 5. The measurements are based on a minimum compliance example, c.f. section 4.3, and the time is measured for the first 10 optimization iterations. The timing includes all steps, from reading the input files, the FE analysis, the optimization, to writing the results back to disc. From the graph in figure 5 it is evident that the code scales as expected. For a given problem size the code scales linearly until the communication becomes dominant. The considered problems results in linear scalability up to approximately 800 CPUs. The range of linear scalability can be extended further by increasing the local operations, i.e. improving the solvers by decreasing the amount of communications which is a subject of future research. Furthermore the code is expected to scale linearly for larger numbers of dof.

In order to measure the scalability of the MMA implementation alone, a simple pure mathematical problem is constructed. The problem has no physical explanation or motivation, and is as such not interesting. The problem should simply ensure that the mechanics of the MMA implementation is executed such that scalability can be measured. The problem used for this purpose is

$$\begin{aligned} \min_{x \in \mathbb{R}^n} \quad & \tfrac{1}{a}\textstyle\sum_j^n x_j^2 + x_j^3 \\ \text{s.t.} \quad & 1 + \tfrac{1}{b}\textstyle\sum_j^n x_j \leq 0 \\ & \tfrac{1}{b}\textstyle\sum_j^n \sin(x_j) - 1 \leq 0 \\ & -2 \leq x_j \leq 2, \quad j = 1, n \end{aligned} \tag{16}$$

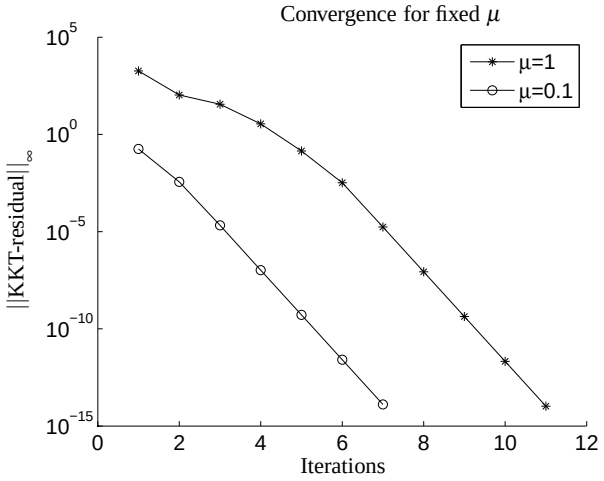

Fig. 4 Convergence of the Newton solver for the MMA dual problem for a fixed barrier parameter.

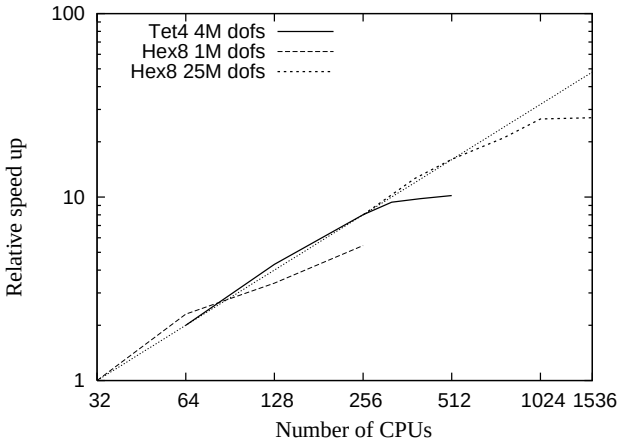

Fig. 5 Relative speed up for the parallel framework measured on 10 optimization iterations of the minimum compliance example. The dotted line represents linear speed up. The measurements were performed on a Cray XT4/XT5 supercomputer .

where a and b are large numbers used to scale the problem to obtain better numerical properties for large numbers of design variables. This problem has the nice benefit that setting up the objective and constraints only gives rise to one parallel barrier while the sensitivity computation is fully parallel. This means that almost all communication will take place within MMA. For the scalability measurements the scalars are chosen to be $a = \sqrt{n}$ and $b = n$.[1] In order to obtain reliable results with respect to timing, the problem is solved repeatedly a total of 60 times with an external move-limit of 0.05. Four different uniform initial x^0's are used for the scaling measurement i.e. $x^0 = \{-1.5, -0.5, 0.5, 1.5\}$. The result can be seen in figure 6 and it is observed that the MMA implementation has scalability close to linear. This is as expected based on the excellent parallel structure of MMA and the chosen solver.

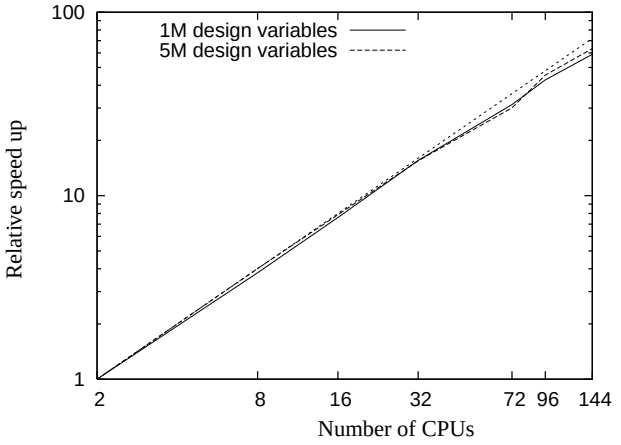

Fig. 6 Relative speed up of for the MMA implementation. The dotted line represents linear speed up. The measurements were performed on a small cluster consisting of 144 CPUs (18 nodes with each 2 AMD Opteron quad core 2376 at 2.3 GHz and 16GB memory per node connected by an Infiniband interconnect).

4.2 Stokes flow

The first numerical example which demonstrates the capabilities of the implemented optimization package is Stokes flow with minimum pressure drop and six target outflow constraints, see e.g. Aage et al (2008). This problem is chosen since it offers to test the presented MMA implementation with several non-linear constraints and non-feasible starting point for the design field. Moreover the state equations give rise to a saddle point problem, which is often the case in coupled multiphysics problems. The optimization problem can be stated compactly as

$$\begin{aligned} \min_{\rho\in\mathbb{R}^n} \quad & \int_\Omega \nu\nabla\boldsymbol{u}\cdot\left(\nabla\boldsymbol{u}+(\nabla\boldsymbol{u})^T\right)+\alpha(\rho)\boldsymbol{u}\cdot\boldsymbol{u}\mathrm{d}\Omega \\ \text{s.t.} \quad & \nu\nabla\cdot\left(\nabla\boldsymbol{u}+(\nabla\boldsymbol{u})^T\right)+\alpha(\rho)\boldsymbol{u}-\nabla p=0 \\ & \nabla\cdot\boldsymbol{u}=0 \\ & \left(\frac{\int_{A_i}\boldsymbol{n}\cdot\boldsymbol{u}\mathrm{d}A}{Q_i}-1\right)^2-\varepsilon^2\leq 0 \;\; i=1,m \\ & \frac{\int_V\rho\mathrm{d}V}{V^*}-1\leq 0 \\ & 0\leq\rho_j\leq 1, \quad j=1,n \end{aligned} \tag{17}$$

where $\boldsymbol{u}$ and p are the velocity and pressure, respectively, and $\nu = 1$ is the non-dimensionalized viscosity. The design

[1] With these parameters the optimum is $x_j^* = -2$ for $j = 1, n$.

interpolation

$$\alpha(\rho) = \alpha_{\max} + (\alpha_{\min} - \alpha_{\max})\rho\frac{1+q}{\rho+q} \tag{18}$$

is as suggested by Borrvall and Petersson (2003) with $q = 1$, $\alpha_{\max} = 10^4$ and $\alpha_{\min} = 10^{-4}$. After the state equations the first constraint is that of the target outflow rate where $Q_i = Q_{inlet} f_i$ is the desired mass flow at outlet i and $\sum_i^m f_i = 1$. The parameter ε, here chosen to be 0.015, is the error allowed at each outlet. A constraint on the volume is included with V^* set to 30% of volume of the design domain. The optimization is performed on a design domain of dimensions $5 \times 3 \times 3$. The inlet and the six outlets are modeled using rectangular boxes of dimensions $1 \times 0.5 \times 0.5$ where the long dimension is parallel direction of the flow. The outlets are distributed such that there is no symmetry in the design problem.

The state problem is discretized using FEM with linear elements for the velocities and constant pressure, i.e. u1p0 Lagrange elements. For the presented example this resulted in a total of $3.3 \cdot 10^6$ degrees of freedom (dofs) for the state field and $7.5 \cdot 10^5$ dofs for the design field using element wise constant design variables. Despite that these elements, i.e. u1p0, are known not to be LBB stable (Zienkiewicz and Taylor, 2000), they have previously been demonstrated to work adequately for this problem when allowing the flow to be slightly compressible (Aage et al, 2008). The boundary conditions are implemented using Lagrange multipliers and consist of no-slip conditions on all walls excepts the inlet, where a parabolic profile is prescribed, and the outlets which are free surfaces. The state problem is solved using a block version of the FSAI (Lazarov and Sigmund, 2011a) preconditioner and the minimum residual method is applied due to the saddle point nature of the linear system. Note that each optimization iteration requires two solutions of eight linear systems; one for the state problem, one for the objective adjoint and six adjoints for the target outflow constraints. The problem is tested on a cluster consisting of 18 nodes with each 2 AMD Opteron quad core 2376 at 2.3 GHz and 16GB memory per node connected by an Infiniband interconnect, i.e. a total of 144 cores. Each linear solve requires approximately 3000 MinRes iterations and takes about one minute. Thus each optimization iteration takes a little under 8 minutes. Note that the number of iterations increases from approximately 1700 for a uniform initial guess to around 3000 for the black and white optimized design. The total computational time can be decreased by a factor equal to the number of the solutions by employing block version of the MinRes and such study together with a detailed presentation of the block FSAI preconditioner is left for subsequent article. As a comparison to the iterative solver the problem was also solved using the parallelized LU factorization package MUMPS (Amestoy et al, 2000), which facilitates that the factorization can be reused for the adjoint problems. However, the factorization alone takes more than an hour and uses more than 275 GB of memory due to densely populated saddle point system. The direct approach is therefore abandoned. The optimization process is terminated after 850 design iterations with $||\rho^k - \rho^{k-1}|| = 0.019$. It takes MMA the first seven iterations to reach a feasible design, and within the first two iterations the objective was as a consequence increased by 0.2% compared to the objective for the initial distribution of uniform $\rho^0 = 0.3$. The convergence is found to be monotonically decreasing from the third iteration and on. Of the six outflow constraints five are active upon termination and one is inactive. This has been the case from iteration $\approx$30, which is also the point where the main characteristics of the optimized design were first observed. In the remain-

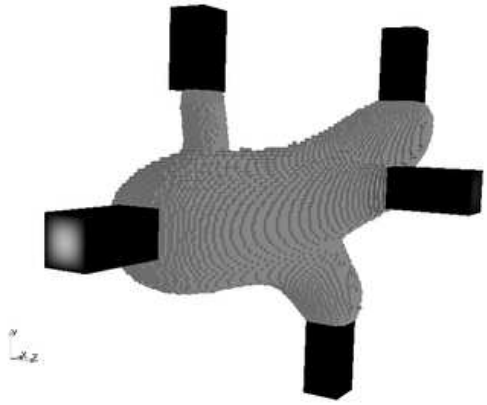

Fig. 7 Threshold plot showing all elements with $\rho > 0.98$ of the optimized design for the Stokes problem with target outflow constraints. The design is shown in gray which correspond to the fluid part of the domain. The black rectangular bricks are the inlet (left) and outlets. The white color seen on the face of the inlet shows the parabolic inlet profile. .

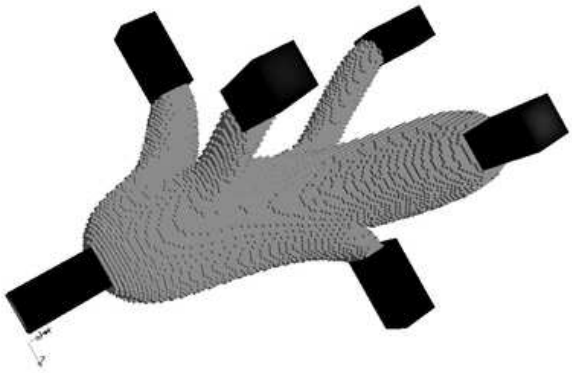

Fig. 8 Threshold plot showing all element with $\rho > 0.98$ of the optimized design for the Stokes problem with target outflow constraints. The design is shown in gray which correspond to the fluid part of the domain. The black rectangular bricks are the inlet (left) and outlets.

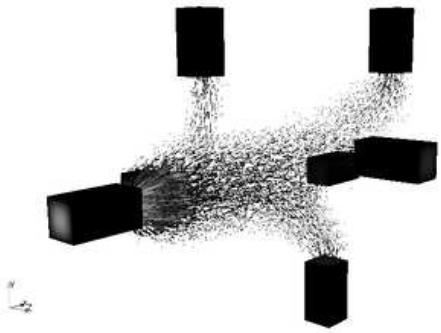

Fig. 9 Plot of the flow field for the optimized design.

ing 800 iterations the design only changed slightly, which is a commonly observed behavior in topology optimization. Threshold plots of the optimized design can be seen in figure 7 and figure 8. The flow field for the optimized design is given in figure 9, from which it is observed that the flow field is properly penalized in regions with $\rho = 0$.

4.3 Linear elasticity

The last numerical example considered is the minimum compliance problem with a volume constraint from linear elasticity (Bendsøe and Sigmund, 2004). The problem can be formulated on a discrete form as

$$\begin{aligned} \min_{\rho \in \mathbb{R}^n} \quad & \boldsymbol{f}^T \boldsymbol{u} \\ \text{s.t.} \quad & \boldsymbol{K}(\rho)\boldsymbol{u} = \boldsymbol{f} \\ & \frac{\Sigma_e^n \rho_e V_e}{V^*} - 1 \leq 0 \\ & 0.001 \leq \rho_e \leq 1, \;\; e = 1, n \end{aligned} \tag{19}$$

where the first constraint contains the finite element discretization of the linear elasticity state problem, e.g. (Zienkiewicz and Taylor, 2000). The SIMP scheme is used for the design interpolation, i.e.

$$\boldsymbol{K}^e = \rho_e^p \boldsymbol{K}_0^e \tag{20}$$

where $\boldsymbol{K}_0^e$ is a reference element stiffness matrix corresponding to solid material and $p > 1$ is the penalization parameter used to penalize regions with intermediate densities. The penalization parameter is fixed to $p = 3$. As opposed to the Stokes flow problem of the previous section the minimum compliance problem is self-adjoint (Bendsøe and Sigmund, 2004), and thus no adjoint problem needs to be solved to obtain the sensitivities.

The state problem is solved using a FSAI preconditioned conjugate gradient (PCG) method, which is possible since the Dirichlet boundary conditions are imposed using the penalty method (Cook et al, 2002). To impose a minimum length scale the PDE filter introduced in Lazarov and Sigmund (2011b) is implemented as well. The scalar PDE problem that constitutes the PDE filter is solved using a Jacobi PCG method. For further details and discussions on the PDE filter the reader is referred to the aforementioned paper.

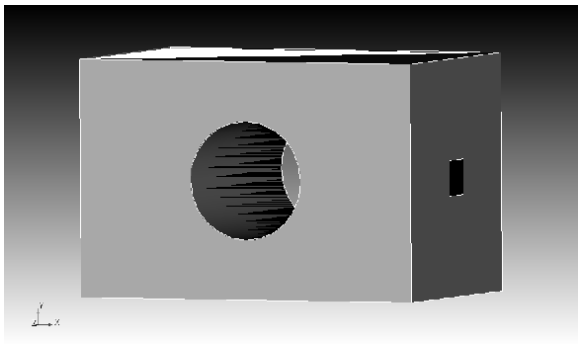

Fig. 10 Design domain for the minimum compliance problem consisting of a $3 \times 2 \times 2$ solid block. A hole with radius 0.5 along the z-axis has been removed to fully utilize the hexahedral elements used for the finite element model. The domain is clamped on the left side and the black area on the right side illustrates where a distributed traction force is applied. The direction of the loading is into the paper, i.e. in the negative z-direction. Symmetry it not enforced on the design domain.

The design problem attacked in this paper is shown in figure 10. The finite element implementation uses linear hexahedral elements and the mesh for the problem in figure 10 consists of $4.7 \cdot 10^6$ design dofs and a total $14 \cdot 10^6$ state dofs. The design problem described in figure 10 has two symmetry axes that could have been used to reduced the number of unknowns by a factor of four. This is however not utilized since the aim is to demonstrate the capability of large scale modeling within the presented parallel framework. The problem is solved on a cluster of 25 nodes with each 2 AMD Opteron quad core 2354 CPUs at 2.2 GHz with 8 GB memory per node which is connected by standard Ethernet, i.e. a total of 200 cores. Each optimization iteration takes approximately 5 minutes. The process is stopped at iteration 375 since the time available on the cluster ran out. At termination the change was $||\rho_k - \rho_{k-1}|| = 0.06$, and thus the design is not fully converged. The convergence behavior was observed to be monotonic up until termination. The optimized design can be seen from two different angles in figure 11 and figure 12.

5 Conclusion

A general outline of the key aspects which are important in the successful development of an easily maintainable and extendable parallel framework for topology optimization problems is presented in this paper. Emphasis is put on a thor-

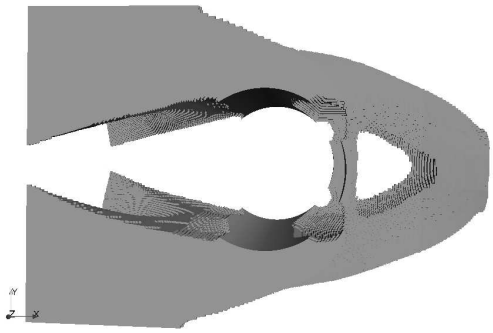

Fig. 11 Threshold plot showing all elements with $\rho > 0.98$ of the optimized design for the minimum compliance problem.

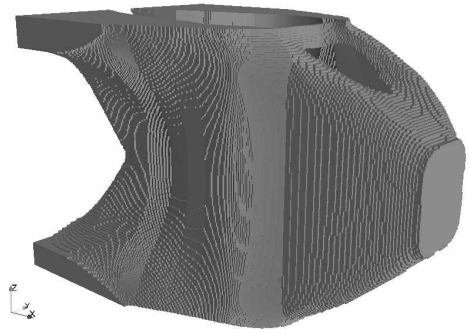

Fig. 12 Threshold plot showing all elements with $\rho > 0.98$ of the optimized design for the minimum compliance problem.

ough description of an efficient parallel implementation of an interior point dual solver for the MMA subproblem.

Both the general framework for solving PDE's and the MMA implementation, are shown to have excellent parallel scaling properties. The capabilities of the framework are successfully demonstrated on optimization problems from both fluid mechanics and solid mechanics.

Future works include extension of the MMA implementation to a globally convergent version. This should be straightforward since the main work, i.e. the subproblem solver, can be reused.

Several approaches can be applied to further improve the performance of the proposed optimization framework. One of the most promising methods is to decouple the discretizations for the separate physical problems. In Nguyen et al (2010), such an approach is successfully applied to topology optimization, in which the design field mesh is decoupled from the state problem mesh. The concept of decoupling can also be combined with more advanced linear solvers, such as FETI or multigrid (e.g. Toselli and Widlund, 2004; Trottenberg et al, 2001), which can be used to decrease the total solution time. Further decreases in solution time can be obtained by utilizing GPUs.

Acknowledgements The authors would like to extend their gratitude to associate Professor Mathias Stolpe, DTU Mathematics, for enlightening discussions on different approaches for solving the MMA subproblem.

References

Aage N, Poulsen T, Gersborg-Hansen A, Sigmund O (2008) Topology optimization of large scale stokes flow problems. Structural and Multidisciplinary Optimization 35(2):175–180

Amdahl G (1967) Validity of the single processor approach to achieving large-scale computing capabilities. In: AFIPS Conference Proceedings, vol 30, p 483485

Amestoy PR, Duff IS, L'Excellent JY (2000) Multifrontal parallel distributed symmetric and unsymmetric solvers. Computer Methods in Applied Mechanics and Engineering 184(2-4):501–520

Andrasson N, Evgrafov A, Patriksson M (2005) An Introduction to Continuous Optimization. Studentlitteratur, Lund, Sweden, iSBN: 91-44-04455-0

Bendsøe M, Sigmund O (2004) Topology Optimization; Theory, Methods and Applications, 2nd edn. Springer Verlag Berlin Heidelberg New York

Borrvall T, Petersson J (2001) Large-scale topology optimization in 3d using parallel computing. Computer Methods in Applied Mechanics and Engineering 190(46-47):6201–6229

Borrvall T, Petersson J (2003) Topology optimization of fluids in stokes flow. Int J Numer Meth Fluids 41(1):77–107

Cook R, Malkus D, Plesha M, Witt R (2002) Concepts and application of finite element analysis, 4th edn. John Wiley & Sons Inc.

Davis TA (2006) Direct Methods for Sparse Linear System. SIAM

Davis TA, Duff IS (1997) SIAM Journal on Matrix Analysis and Applications 18:140–158

Evgrafov A, Rupp CJ, Maute K, Dunn ML (2008) Large-scale parallel topology optimization using a dual-primal substructuring solver. Structural And Multidisciplinary Optimization 36(4):329–345

Fleury C (1993) Mathematical programming methods for constrained optimization: dual methods. In: Karmat MP (ed) Structural optimization - Status and Promise, vol 150, Progress in Astronautics ans Aeronautics, AIAA, pp 123–150

Geuzaine C, Remacle JF (2009) International Journal for Numerical Methods in Engineering 79:1309–1331

Gropp W, Lusk E, Skjellum A (1999) Using MPI: Portable Parallel Programming with the Message-Passing Interface. MIT Press

Karypis G, Kumar V (1999) A fast and high quality multilevel scheme for partitioning irregular graphs. SIAM Journal on Scientific Computing 20(1):359 – 392, mETIS

Kim TS, Kim JE, Kim YY (2004) Parallelized structural topology optimization for eigenvalue problems. International Journal of Solids and Structures 41(9-10):2623–2641

Lazarov B, Augarde C (2005) Object oriented design of parallel and sequential finite element codes. In: Proceedings of the 13th ACME Conference

Lazarov BS, Sigmund O (2011a) Factorized parallel preconditioner for the saddle point problem. Int J Numer Meth Biomed Engng DOI 10.1002/cnm.1366

Lazarov BS, Sigmund O (2011b) Filters in topology optimization based on helmholtz-type differential equations. Int J Numer Meth Engng DOI 10.1002/nme.3072

Luenberger B, Ye Y (2008) Linear and nonlinear programming, 3rd edn. Springer

Mahdavi A, Balaji R, Frecker M, Mockensturm EM (2006) Topology optimization of 2D continua for minimum compliance using parallel computing. Structural And Multidisciplinary Optimization 32(2):121–132, DOI {10.1007/s00158-006-0006-1}

Nguyen TH, Paulino GH, Song J, Le CH (2010) A computational paradigm for multiresolution topology optimization (MTOP). STRUCTURAL AND MULTIDISCIPLINARY OPTIMIZATION 41:525–539

Saad Y (2003) Iterative Methods for Sparse Linear Systems. SIAM

Schmidt S, Schulz V (2009) A 2589 line topology optimization code written for the graphics card. Tech. rep., Deutsche Forschungsgemeinschaft

Stroustrup B (1997) The C++ Programming Language. Addison-Wesley

Svanberg K (1987) The method of moving asymptotes - a new method for structural optimization. International Journal for Numerical Methods in Engineering 25

Svanberg K (2002) *A class of globally convergent optimization methods based on conservative convex separable approximations*. SIAM J OPTIM 12:555–573

Toselli A, Widlund O (2004) Domain Decomposition Methods - Algorithms and Theory. Springer

Trottenberg U, Oosterlee CW, Schuller A (2001) Multigrid: Basics, Parallelism and Adaptivity. Academic Press

Vemaganti K, Lawrence WE (2005) Parallel methods for optimality criteria-based topology optimization. Computer Methods in Applied Mechanics and Engineering 194(34-35):3637–3667

Wadbro E, Berggren M (2009) Megapixel topology optimization on a graphics processing unit. SIAM Review 51(4):707–721

Zienkiewicz OC, Taylor RL (2000) Finite Element Method: (parts 1-3), 5th edn. Butterworth-Heinemann

Publication [P3]

Topology optimization of radio frequency and microwave antennas by free distribution of conducting material

Topology optimization of radio frequency and microwave antennas by free distribution of conducting material

N. Aage[a,*], O. Sigmund[a]

[a] *Department of Mechanical Engineering, Solid Mechanics, Technical University of Denmark, Bld. 404, DK-2800 Kgs. Lyngby.*

Abstract

A methodology for topology optimization of three-dimensional conductor-based microwave and radio frequency structures is presented. Particular attention is directed towards obtaining a design formalism applicable to the systematic design of sub-wavelength antennas for wireless communication. To achieve a robust antenna optimization method, we propose a two phase procedure which eliminates dependence on initial design. Phase I consists of solving an incomplete inverse antenna optimization problem, which is shown, by numerical experiments, to result in useful initial antenna design. The result of the phase I problem is then used as initial guess for phase II, in which the radiated power is maximized. The proposed design formulation is implemented in a parallel C++ finite element code based on first order tetrahedral edge elements. The capabilities of the design formulation is successfully demonstrated on the design of an energy focusing device as well as the design of sub-wavelength antennas.

Keywords:
topology optimization, electromagnetic, finite elements, energy focusing, antenna design

1. Introduction

The design of electrically small antennas for devices such as cellular phones, sensors and hearing aids, has posed new challenges for electrical engineers. In many situations standard antenna design do not fit within the available design space, or their performances are inadequate, and therefore new antenna designs must be devised (Mittra, 2007). As a consequence thereof, the design of electrically small antennas has been extensively studied over the past ten years and among the various designs the most well-known is probably that of the folded helix antenna by Best (2004). This antenna consist of an elaborate distribution of a good conductor, e.g. cobber, on a sphere, which leads to an excellent performance with respect to radiation efficiency. Unfortunately, this antenna design does not fit all areas of application and therefore much effort has been put into optimizing the performance of electrically small antennas for a variety of specific applications.

*Corresponding author
Email address: naa@mek.dtu.dk (N. Aage)

Within the field of electrical engineering most of the optimization approaches are based on simple parameter studies and/or evolutionary algorithms (Hoorfar, 2007). The success of parameter optimization is closely related to the knowledge of a working initial antenna design. The initial configuration can then be optimized by tuning a single, or several, of its parameters such as dimensions, distances between conducting elements, etc. Parameter-type optimization has been conducted using both genetic and gradient-based methods. Optimization of antenna topologies using genetic algorithms has been demonstrated in e.g. (Altshuler, 2002; Robinson and Rahmat-Samii, 2004; Bayraktar et al., 2006; Zaharis, 2008). However, the use of genetic algorithms requires very large numbers of expensive performance evaluations and therefore these examples are restricted to cases of few design variables, and are therefore not applicable to general antenna design problems.

The topology optimization method is however tailored for problems with free material distributions (Bendsøe and Sigmund, 2004). The design and optimization of electrically small antennas is therefore a natural candidate for application of the topology optimization method. The method can be described as an iterative numerical optimization procedure that allows for material to be freely distributed within a predefined design domain, such that a desired performance measure is optimized. Topology optimization works by discretizing the design domain into a number of small volumes, e.g. by the finite element method, and then applying an optimization algorithm to determine if each element should be air or solid. Apposed to other optimization methods, such as size, shape and iso-geometric optimization, the topology optimization approach allows the design topology to change during the optimization process. The method has its origin in mechanical engineering, but has since its development in the late 1980's, successfully been applied to a wide variety of different physical disciplines such as MEMS, fluid mechanics, heat transfer and acoustics to name but a few (Bendsøe and Sigmund, 2004).

The method has already been proven to be highly efficient for electromagnetic problems within the field of optics, see e.g. (Frandsen et al., 2004; Sigmund and Hougaard, 2008; Matzen et al., 2010; Jensen and Sigmund, 2011). For applications in the regime of microwave and radio frequencies the method has primarily been used to enhance performance, such as bandwidth, of antennas by the distribution of a dielectric substrate (Kiziltas et al., 2003, 2004). Also the design of dielectric resonant antennas has been investigated in Nomura et al. (2007).

1.1. Topology optimization by distributing conductive material

A severe challenge of topology optimization for conductor-based design problems is the skin depth issue. The skin depth is defined as the length for which an electromagnetic plane wave can penetrate into a conductor before the amplitude is decreased by a factor of e^{-1} (Balanis, 2005). The skin depth, δ, can be approximated by the following expression

$$\delta = \frac{1}{\sqrt{\pi \sigma \mu f}} \tag{1}$$

where f is the frequency, σ the conductivity and μ the permeability. Using e.g. copper as the conductor, the skin depth in the microwave regime is in the order of μm, whereas the antennas has dimensions in mm or cm. The three order of magnitude difference in wavelength and antenna dimensions compared to that of the skin depth, means that 3D

models would require billions of elements within the design space to ensure that the skin depth is properly resolved.

Despite this numerical bottleneck, some works on topology optimization of metallic RF and microwave devices have been published within the past decade. In Kiziltas (2003), a first approach was demonstrated based on a modified version of the well-known solid isotropic material with penalization (SIMP) interpolation scheme (Bendse, 1989). This approach was also pursued in Erentok and Sigmund (2011) for the design of electrically small antennas. The method was shown to work, but since the interpolation scheme do not fulfil the energy balance, the optimized result require elaborate postprocessing to obtain a functioning antenna. This is a consequence of not resolving the skin depth. In Diaz and Sigmund (2010) the topology optimization method is used to design conductor-based metamaterials with negative permeability. For this optimization problem the dimensions of the design domain are naturally chosen such that the skin depth is resolved. A similar design problem was solved by a level-set method in Zhou et al. (2010b) and in Zhou et al. (2010a) the same level-set method was applied to the design of planar dipole antennas.

A general cure for the skin depth problem in standard topology optimization was proposed in Aage et al. (2010). In this paper a new design interpolation was introduced which dealt with the skin depth by the imposition of an impedance boundary condition on each finite element in the design domain. The design interpolation was successfully demonstrated for the design of 2D electric and magnetic resonators and a monopole antenna.

The work presented in this paper is an extension of the design method described in Aage et al. (2010) to the three dimensional setting. In addition we also propose a design formalism that enables systematic design of sub-wavelength antennas without the presence of a functioning initial antenna design.

2. The analysis problem

The physics governing the propagation of electromagnetic waves are fully described by Maxwell's equations (Balanis, 1989). In the setting of the presented work, the system loading is adequately modeled as being time-harmonic and Maxwell's equations can therefore solved in the frequency domain. We use the finite element method to discretize and solve the partial differential equations based on vector, or edge, elements (Zhu and Cangellaris, 2006; Jin, 2002). A general problem definition for the modeling and optimization of antennas and other RF and microwave systems can be seen in figure 1. The grey region of figure 1 can represent either a design domain for optimization or an already known antenna configuration to be analyzed. Throughout this paper, the wave equation is solved for the electric field, and therefore only results for the electric field is presented. Note however that both the modeling and optimization procedure has an equivalent magnetic field formulation, see Aage et al. (2010) for details. The wave equation for the electric field takes the form of a curl-curl equation, i.e.

$$\nabla \times \left(\mu_r^{-1} \nabla \times \boldsymbol{E}\right) - k_0^2 \left(\epsilon_r - j\frac{\sigma}{\omega \epsilon_0}\right) \boldsymbol{E} = 0 \text{ in } \Omega \tag{2}$$

where μ_r, ϵ_r and ϵ_0 are the relative permeability, relative permittivity and free space permittivity, respectively. The free space wave number is denoted by k_0 and σ is the

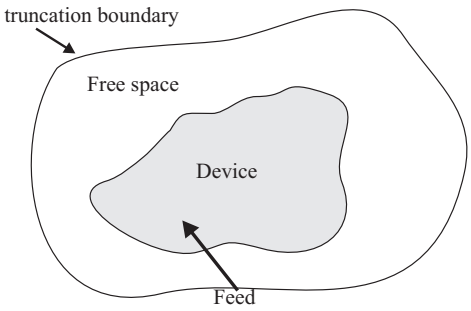

Figure 1: General sketch of a modeling problem for an antenna analysis. In case of optimization the grey area represents the design domain.

conductivity. The frequency is given by ω and j refers to the imaginary unit. The computational domain is truncated using a first order absorbing boundary condition (ABC). This condition can be considered adequate if placed far enough from the structure, such that the scattered waves are normal incident to the ABC surface. The condition can be formulated such that it includes a possible incident field. This results in an inhomogeneous mixed boundary condition that can be stated as

$$\boldsymbol{n} \times (\nabla \times \boldsymbol{E}) + jk_0 \boldsymbol{n} \times (\boldsymbol{n} \times \boldsymbol{E}) = -\boldsymbol{n} \times [\boldsymbol{E}_0(\boldsymbol{r}) \times jk_0(\boldsymbol{n} - \boldsymbol{k})]\, e^{-jk_0 \boldsymbol{k}\cdot\boldsymbol{r}} \tag{3}$$

where $\boldsymbol{n}$ is an outward normal vector, $\boldsymbol{E}_0(\boldsymbol{r})$ contains the profile of the incident wave, $\boldsymbol{k}$ the direction of propagation and $\boldsymbol{r}$ the coordinates. Another boundary condition which is often used in antenna design problems is the perfect electric conductor (PEC) condition, i.e.

$$\boldsymbol{n} \times \boldsymbol{E} = \boldsymbol{0} \tag{4}$$

By application of the standard Galerkin method the continuous problem is discretized and cast on the form of a linear system, i.e.

$$\boldsymbol{S}\boldsymbol{E} = \boldsymbol{b} \tag{5}$$

where $\boldsymbol{S}$ is the system matrix, $\boldsymbol{E}$ a vector of edge degrees of freedom (dofs) and $\boldsymbol{b}$ is the load vector. The specific structure of the system matrix and the load vector is described in details in e.g. Jin (2002).

The finite element problem described above is discretized using first order tetrahedral edge elements and the PDE problem is implemented in a parallel C++ framework developed in-house (Aage and Lazarov, 2011). The parallelization is obtained using the Message-Passing Interface (MPI) (e.g. Gropp et al., 1999). The preprocessing and mesh generation is performed using Cubit (Sandia Corporation) and the partitioning is obtained from METIS (Karypis and Kumar, 1999). The visualization and postprocessing is done using the open source visualization package Paraview (`www.paraview.org`). The parallel LU factorization package MUMPS (Amestoy et al., 2000) is used to solve the linear system in equation (5). All numerical experiments have been conducted on a cluster consisting of 18 nodes with each 2 AMD Opteron quad core 2376 processors working at 2.3 GHz with 16 GB memory. The nodes are connected by an Infiniband interconnect.

3. The optimization problem

3.1. Design interpolation

The goal of the optimization process is to determine whether or not each of the design elements should be void or solid, i.e. have conductivity zero or σ_c. Here σ_c corresponds to the conductivity of a good conductor such as e.g. copper. The direct approach leads to a binary optimization problem, which is not readily solvable for large number of design variables (Bendsøe and Sigmund, 2004). In standard topology optimization this limitation is remedied by the introduction of a continuous variable for each design element $0 \leq \rho_e \leq 1$, which is then used to smoothly interpolate between the two material phases. The choice of interpolation function is crucial for the success of the optimization process, and must be derived subject to a number of requirements such as e.g. circumventing the skin depth issue. Such an interpolation scheme is introduced in Aage et al. (2010) and is adopted in this work. The interpolation remedies the skin depth problem by wrapping each design element in an impedance boundary condition that can be turned on or off by the design variables. For the electric field the interpolation scheme can be stated for a single design element as

$$\begin{aligned} &\nabla \times (\mu_r^{-1} \nabla \times \boldsymbol{E}) - k_0^2 \left(\epsilon_r - j \frac{\sigma^d \left(\frac{\sigma^m}{\sigma^d} \right)^{\rho_e}}{\omega \epsilon_0} \right) \boldsymbol{E} = 0, && \text{in } \Omega_e \\ &\boldsymbol{n} \times (\mu_r^{-1} \nabla \times \boldsymbol{E}) - \rho_e^{13} j k_0 \sqrt{\epsilon_r^m - j \frac{\sigma^m}{\omega \epsilon_0}} \boldsymbol{n} \times (\boldsymbol{n} \times \boldsymbol{E}) = 0, && \text{on } \Gamma_e \end{aligned} \tag{6}$$

where $(\cdot)^m$ refers to material properties of the conducting material and $(\cdot)^d$ to the properties of the background material. The element volume is denoted by Ω_e and Γ_e refers to the elements surface. Due to numerical reasons σ^d must be chosen larger than zero, but small enough such that it does not damp out the electromagnetic fields excessively. Experience from both Aage et al. (2010) and Diaz and Sigmund (2010) have shown that $\sigma^d = 10^{-4}$ is a good choice. The second equation in the design parameterization is a modified form of an impedance condition. Impedance conditions are usually used in FEA to model interfaces between dielectrics and conductors with finite conductivity, that is, the condition simply models the effect of the skin depth. The effect of the element impedance condition is to ensure that design elements with $\rho_e = 1$ will resolve the skin depth regardless of the element size. In the case of $\rho_e = 0$ the impedance condition does not contribute to the finite element equations, and thus allows for normal wave propagation. For intermediate design variables the design parameterization has no clear physical interpretation, though one might be able to link them to materials with varying conductivities. However, since the aim is to end up with designs with clear 0-1 solutions, the interpolation scheme should merely be interpreted as a tool used to obtain a well posed continuous optimization problem. It is worth noting that the interpolation scheme leads to a self-penalized optimization problem, and that almost 0-1 solution therefore can be expected. This is because regions with intermediate conductivities will slowly damp the electromagnetic energy, and thus absorb more energy than regions of high conductivity where the spatial decay is faster (Aage et al., 2010).

3.2. Problem formulation and solution method

The optimization problem is, in standard gradient-based topology optimization, posed in the form of a non-linear mathematical programme. The optimization problems inves-

tigated in the present work can be formulated as

$$\begin{aligned} \max_{\rho \in \mathbb{R}^n} \quad & f(\boldsymbol{E}(\rho)) \\ \text{subject to} \quad & \frac{\sum_e^n \rho^e V^e}{V^*} - 1 \leq 0, \\ & \boldsymbol{S}(\rho)\boldsymbol{E} - \boldsymbol{b} = 0 \\ & 0 \leq \rho^e \leq 1, \qquad e = 1, n \end{aligned} \tag{7}$$

where $f(\boldsymbol{E}(\rho))$ is a real valued objective function with complex input, ρ is a vector of design variables and $\frac{\sum_e^n \rho^e V^e}{V f^*} - 1 \leq 0$ is a constraint on the amount of available material denoted by V^*. Optimization problems of the form in equation (7) can be solved using a gradient-based optimizer such as the Method of Moving Asymptotes (MMA) (Svanberg, 1987). The MMA algorithm has also been implemented in the parallel C++ framework, where it is solved using an interior point dual method, see e.g. Luenberger and Ye (2008).

The sensitivities required for the application of gradient-based optimization methods are obtained using the adjoint method as described in (Jensen and Sigmund, 2005). This leads to the following expression for the sensitivities, using the assumption that the objective and right hand side of the state problem do not explicitly depend on the design variables

$$\frac{\partial f}{\partial \rho^e} = 2\mathbb{R}\left(\boldsymbol{\lambda}^T \frac{\partial \boldsymbol{S}}{\partial \rho^e}\boldsymbol{E}\right) \tag{8}$$

where $\mathbb{R}$ refers to the real part, $(\cdot)^T$ is the real transpose and $\boldsymbol{\lambda}$ is an adjoint field which is obtained from the solution of the adjoint problem given by

$$\boldsymbol{S}\boldsymbol{\lambda} = -\frac{1}{2}\left(\frac{\partial f}{\partial \boldsymbol{E}_R} - j\frac{\partial f}{\partial \boldsymbol{E}_I}\right)^T \tag{9}$$

where $\boldsymbol{E}_R$ and $\boldsymbol{E}_I$ correspond to the real and imaginary part of the electric field, respectively. Finally, in order to avoid the appearance of single conducting elements in the optimized design, a PDE-based design variable filter is applied to impose a minimum length scale on the optimized design (Lazarov and Sigmund, 2010). As will be shown later, filtering is in fact necessary for the successful optimization of antenna structures.

4. Design of an electric energy focusing device

The first optimization problem examined is the design of an electric energy focusing device. This problem is a straight forward extension of the 2D examples shown in Aage et al. (2010) to the 3D setting, and is primarily used to validate and examine the behavior of the 3D optimization implementation. However, this type of design problem is also very useful for the design of sub-wavelength antennas. The reason for this will be explained in the upcoming sections on antenna design.

The objective for the focusing device is to maximize the time averaged electric energy within an a priori specified objective domain, i.e.

$$f(\boldsymbol{E}(\rho)) = \log_{10}\left(\frac{1}{\phi_{\text{ref}}}\int_{\Omega_{\text{obj}}} |\epsilon \boldsymbol{E}|^2 \, \mathrm{d}\Omega\right) \tag{10}$$

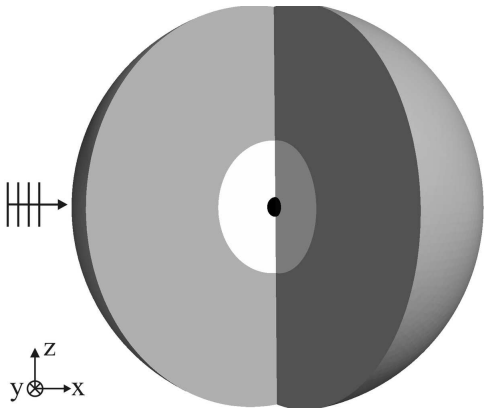

Figure 2: Sketch of modeling setting for the optimization of an 3D electric resonator. The white sphere with $r = 1$ m corresponds to the design domain, the black sphere with $r = 0.08$ m to the objective domain and the grey sphere with $r = 3$ m to free space. The target frequency is 120MHz and $\sigma^m = 10^7$ S/m and $\sigma^d = 10^{-4}$ S/m. The design domain is illuminated by a plane wave with unit amplitude traveling along the x-axis with polarization in the z-direction.

where $\phi_{\text{ref}} = 4\epsilon_0$ J is used to scale, and non-dimensionalize the electric energy, and the logarithm is applied to scale the objective since experience have shown that this leads to better numerical performance. The design problem considered is illustrated in figure 2. The optimization is performed in the RF regime at a target frequency of 120 MHz using a conducting material with $\sigma^m = 10^7$ S/m and a dielectric background material with $\epsilon_r = 1$. The excitation is a plane wave with unit amplitude traveling along the positive x-axis with the electric field linearly polarized in the z-direction. The discretized problem has 10^6 complex state dofs and a total of $3.8{\cdot}10^5$ design elements. The mesh is partitioned into 72 parts, and each design cycle takes approximately 3 minutes. In order to have a frame of reference to which the performance of the optimized design can be compared, the electric energy is computed for the case where all $\rho = 0$, i.e. the free space energy. The reference objective is found to be $f_0 = -1.88$.

The settings for the optimization problem are as follows. The allowed amount of material is set to 60% of the total design domain and the radius of influence for the PDE filter is chosen to $R_{\text{min}} = 0.08$ m. The initial design variable distribution is uniform with $\rho_{\text{init}} = 0.3$, and the optimization process is terminated when the stopping criteria $||\rho^k - \rho^{k-1}||_\infty < 1\%$ is fulfilled.

The optimization process converged in 201 iterations having used 35% of the available material, i.e. the volume constraint was inactive upon convergence. The optimized design and convergence history can be seen in figure 3 and the final objective value is $f = 0.98$. This corresponds to an electric energy that is 723 times larger than that of the reference energy. The optimized design is seen to take on a shape similar to that of a parabola, but with two extra arms that touch the objective domain. Furthermore a small reflector is seen centered in front of the larger parabola-like structure. This design makes intuitive sense, since such a structure will first reflect the incoming wave towards the reflector situated to the left, which will then reflect the wave into the objective domain. The two arms that are in contact with the objective domain allows the electric field to flow from

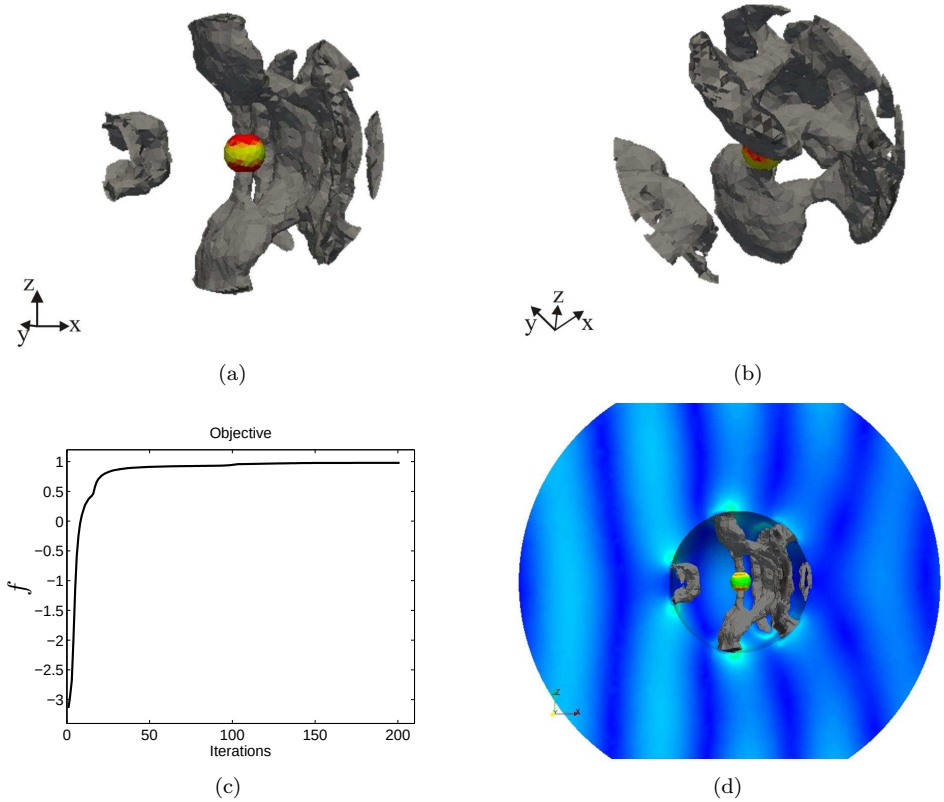

Figure 3: (a) and (b) optimized design for the problem described in figure 2. (c) convergence history, and (d) optimized design and a slice-plot of the electric field is visualized. The design plots are based on an isosurface representation with cut off at $\rho > 0.5$. .

one arm to the other, similar to how charge build-up in a capacitor.

As is the case for many optimization problems, the optimized design in figure 3 is likely to be a local minimum, due to non-convexity of the optimization problem investigated. However, similar designs and objectives were obtained by starting the optimization with initial distributions of $\rho = 0.2$ and $\rho = 0.5$. This behavior was also observed for the 2D examples presented in Aage et al. (2010).

5. Antenna design

We consider an antenna design problem in which a hemispherical design domain with radius 0.08 m, located on an PEC groundplane, is fed by a 50 Ohm coaxial cable. The target frequency is 300 MHz and the coaxial cable situated at the outer surface of the spherical design domain. The coaxial cable has an inner radius of $r = 2$ mm and supplies 1 W of input power. To ensure a good connection between the coaxial feed and the design domain, the inner conductor is extended 1 cm into the design domain. The model problem can be seen illustrated in figure 4. The choice of design domain

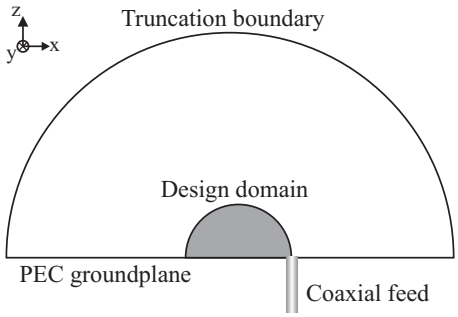

Figure 4: Sketch of the model for the optimization of an 3D electrically small antenna, here shown as a slice in the xz-plane. Both design and freespace domains are hemispheres with radius $r = 1$ m and $r = 0.08$ m, respectively. The free space domain is truncated by a first order ABC. The target frequency is 300 MHz. The design domain is fed through a coaxial cable which impose a TEM coaxial mode with characteristic impedance of 50 Ohm and an input power of 1 W. The inner conductor has radius $r = 2$ mm and the cable uses a dielectric with $\epsilon_r = 1$. The inner conductor of the coaxial cable is extended 1 cm into the design domain in order to properly connect the feed line with the design. The length of the coaxial cable is $l = 0.12$ m.

dimensions and target frequency leads to a sub-wavelength antenna design problem, i.e. $D/\lambda = 0.16$ where $D = 0.16$ m is the overall length of the design domain and $\lambda \approx 1$ m is the wavelength. This design problem is similar to the problem examined in (Erentok and Sigmund, 2011). However, here we extend the design problem such that conducting material is allowed to be distributed within the entire design domain hemisphere and not just in the shell enclosing it.

The objective of the optimization problem is to maximize the radiated power, which should result in an antenna with a large operational bandwidth. The radiated power can be computed as the time averaged power flow through the boundary used to truncate the free space domain, i.e.

$$f(\boldsymbol{E}(\rho)) = \int_{\Gamma} \boldsymbol{n} \cdot \left(\frac{1}{2} \mathbb{R} \left[\boldsymbol{E} \times \bar{\boldsymbol{H}} \right] \right) \mathrm{d}\Gamma \tag{11}$$

where $\bar{(\cdot)}$ refers to the complex conjugate and the magnetic field is obtained by application of Faraday's law to the finite element solution for the electric field. Another useful parameter relevant for determining the characteristics of an antenna is the reflection coefficient, also called the S_{11} parameter, which can be expressed as

$$S_{11} = \frac{\int_A (\boldsymbol{E} - \boldsymbol{E}_0) \cdot \bar{\boldsymbol{E}}_0 \mathrm{d}A}{\int_A |\boldsymbol{E}_0|^2 \mathrm{d}A} \tag{12}$$

where $\boldsymbol{E}_0$ refers to the fundamental Transverse Electric and Magnetic (TEM) mode of a coaxial cable (Balanis, 1989), and the integration is performed on the surface that terminates the coaxial cable. Based on the reflection coefficient it is possible to compute the operational bandwidth of the optimized antenna.

To systematically optimize the layout of antenna structures, we propose a two step optimization procedure. The first step consists of determining an useful material layout that can be used as an initial guess for step two, i.e. the antenna optimization problem

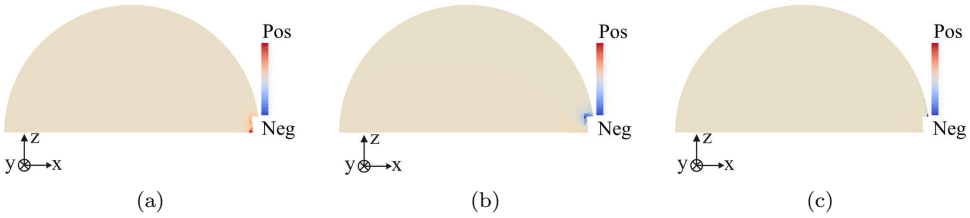

Figure 5: Slice plots in the xz-plane of the sensitivities for the antenna design problem in figure fig:Antennaproblemsketch for different uniform initial distributions. (a)-(c) sensitivities corresponding to the cases where $\rho_{\text{init}} = 0$, $\rho_{\text{init}} = 0.3$ and $\rho_{\text{init}} = 1$, respectively. The feed is located in the bottom right corner of the domain.

presented above. The reason for splitting the seemingly ready-to-solve antenna design problem into two phases, is because the success of the antenna optimization is highly dependent on the existence of a good initial design. In the upcoming sections we will first explain why the antenna problem require a good initial design, secondly why filtering is necessary and finally present the two step optimization approach.

5.1. The effect of the system feed on the initial stage of the optimization

The antenna design problem in figure 4 has many similarities with the focusing device example. The main difference lies in the way the system is fed, i.e. a coaxial port apposed to an incident plane wave. Though the difference in type of excitation seems small at first, it turns out that the optimization problems have quite different characteristics. A simple way to exemplify this, is to examine the sensitivity distribution for a series of uniform initial distributions.

Figure 5 shows the objective sensitivities for the antenna problem for three different uniform initial design distributions. From these plots it is clear that the sensitivity information is localized at the feed point. The reason for this is due to the physics of the antenna problem. That is, an antenna works by coupling the signal from the feed into the antenna structure. The signal will then flow along the boundary of the antenna structure and, if the antenna is designed properly, radiate into space (Balanis, 2005). This means, in the absence of an antenna structure, that the field intensity will be localized at the feed line termination, and (numerically) zero elsewhere. From the sensitivity expression in equation (8), it is evident that a zero electric field will result in zero sensitivities, which is exactly what the plots in figure 5 shows. With respect to solving the optimization problem, this means that the chance of getting stuck in a local minimum before having unfolded a well performing antenna must be considered high. In Erentok and Sigmund (2011) the authors works around this problem by initializing the design with $\rho_{\text{init}} = 1$ and by applying a volume constraint that only allows for 60% material. This means that the initial design is infeasible and that the optimizer will start to reduce the used material to reach a feasible point. In the process of achieving feasibility, the optimizer passes through a material layout that has the characteristics of an antenna. Unfortunately, the authors were not successful in applying this approach for the full hemispherical design domain.

However, for the case of energy focusing device optimization the sensitivity distribution is entirely different. This is shown in figure 6 where the sensitivities are seen to be

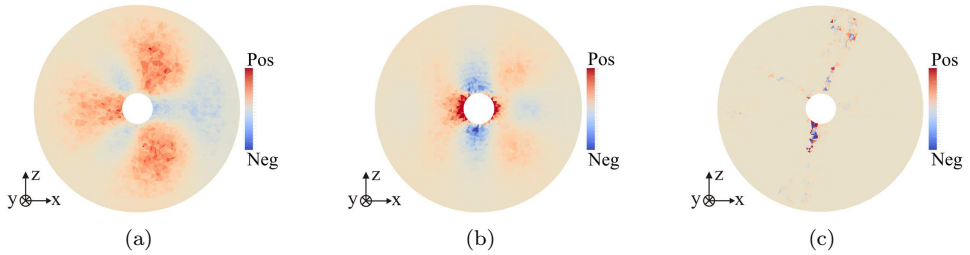

Figure 6: Slice plots in the xz-plane of the sensitivities for the energy focusing device presented in section 4. (a)-(c) sensitivities corresponding the cases where $\rho_{\text{init}} = 0$, $\rho_{\text{init}} = 0.3$ and $\rho_{\text{init}} = 1$, respectively.

distributed throughout the design domain. This is due to the prescribed incident field which illuminates the design domain, and thus ensure the existence of a non-zero electric field. It is duely noted, and expected, that $\rho_{\text{init}} = 1$ is a poor starting guess since the damping in this case will render almost all sensitivities zero.

5.2. The influence of sharp material interfaces

The concentration of the electric field intensity along the surface of an antenna structure complicates the optimization process by the introduction of artificial local minima. The problem is caused by the presence of sharp material interfaces, and can be exemplified by a simple sizing problem, in which the height, h, of a monopole antenna is optimized. This problem has an analytical solution, i.e. the optimal height is $h^* = 0.21\lambda$ for an infinitesimal thin copper wire (Balanis, 2005). The design problem is illustrated in figure 7(a), from which it is seen that the current design has $h > h^*$ and thus that the height needs to be reduced. Figure 7(b) shows two different design variable distributions which could occur when $h > h^*$. For both cases the dark gray region correspond to $\rho = 1$ and white to $\rho = 0$. For the first case, the light gray region corresponds to $\rho = 0$, which results in a field intensity illustrated by the red curve. This curve shows that energy is zero within the conductor and that it attains its maximum at the interface between $\rho = 1$ and $\rho = 0$, after which it decays monotonically by $1/r^3$. In the second case, the light gray region corresponds to $\rho = 0.5$ which gives rise to a field intensity as shown by the blue curve. The blue curve display peaks in the field intensity for both the interface between $\rho = 1$ and $\rho = 0.5$, and for the interface between $\rho = 0.5$ and $\rho = 0$. The consequence of these extra peaks in energy can be seen in figure 7(c), which illustrates how the radiated power varies as a function of the ρ in the light gray region. From this figure it is seen that the objective is larger for $\rho = 0$ than for $\rho = 1$, which is expected since the optimal height is lower than the current antenna configuration. However, for intermediate values of the design variable, it is seen that the objective function attains its actual minimum. This means that the optimizer has no chance of changing the tip of the design from $\rho = 1$ to $\rho = 0$, due to the sign change in sensitivities for intermediate ρ. However, this problem can be remedied by filtering the design variables. The application of design filter results in smeared interfaces, which eliminates the existence of multiple field intensity peaks. This has been verified by several numerical experiments.

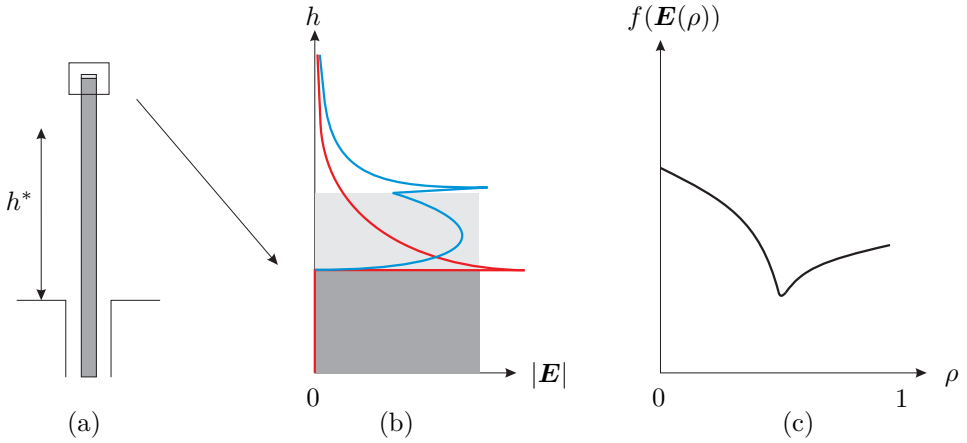

Figure 7: Illustration of how the localized field intensity affects the optimization process. (a) the monopole antenna with $h > h^*$, where h^* refers to the optimal height. (b) field intensity at the tip of the design front, for two different design variable distributions. For both cases dark gray corresponds to $\rho = 1$ and white to $\rho = 0$. In case one, the light gray refers to $\rho = 0$ and gives rise to the red field intensity curve. For case two, $\rho = 0.5$ in the light gray region, which corresponds to the field intensity shown as the blue curve. (c) illustration of how different values of ρ in the light gray region affects the radiated power.

5.3. The two phase optimization setting

The main idea of the phase I design problem is to invert the antenna optimization task. So instead of feeding the system through the coaxial cable and maximizing the power flow over the truncation boundary, the system is fed by a number of incident waves, prescribed on the truncation boundary, and the power flow is maximized at the coaxial port. This should, based on the findings from the energy focusing example, result in a design problem for which the sensitivities are not localized. Note that it is generally not possible to determine a correct and proper excitation in order to obtain a true inverse antenna design problem. However, since the goal of the inverse design problem is not to design the actual antenna, but merely to obtain a design adequate for use as an initial guess, the number of incident waves can be kept finite and in practise quite low. Based on the same argument, there is no need to let the phase I problem converge. Therefore a heuristic termination criteria for the phase I problem is to stop when the change in objective function is below a certain tolerance, i.e. when the objective function flattens out. For most topology optimization problems this happens within the first 20 to 30 design cycles (Bendsøe and Sigmund, 2004). In the remainder of this work the stopping criteria for the phase I problem is 30 iterations.

The objective for the phase I optimization problem can be formally stated as

$$\max_{\rho \in \mathbb{R}^n} \quad \frac{1}{q} \sum_{k=1}^{q} \log_{10} \left(\frac{1}{\phi_{\text{ref}}} f_k(\boldsymbol{E}_k(\rho)) \right) \tag{13}$$

where $\phi_{\text{ref}} = 1$ W is used to non-dimensionalize the argument for the logarithm and $f_k(\boldsymbol{E}_k(\rho))$ refers to the power flow, equation (11), evaluated at the coaxial port for each of the q incident waves. In the formulation proposed here all incident waves are weighed

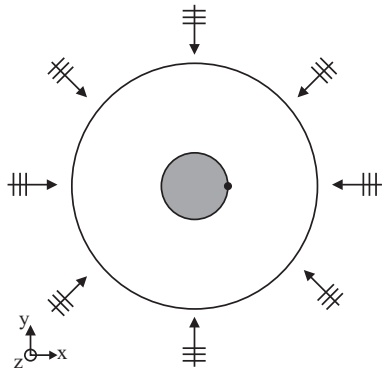

Figure 8: Sketch of the incident waves used for the phase I problem. All waves propagate in the xy-plane and also oscillates in this plane. The gray region refers to the design domain and outer circle to the truncation boundary on which the incident waves are imposed. The small black dot to the right of the design domain illustrates the coaxial feed.

equally. It should also be noted that since the excitation frequency is fixed, the system matrix is identical for all load cases. This means that the factorization can be reused and thus that the increase in number of load conditions comes at a very low numerical cost.

5.4. Numerical examples

In this section the antenna optimization problem described in figure 4 is solved using the proposed two phase procedure. The examples cover both the shell problem, as well as the full volumetric problem.

The phase I problem is solved using only eight incident waves. The directions of these are chosen such that they illuminate the design domain from eight different angles in the xy-plane and can be seen illustrated in figure 8. The incident waves are all chosen to propagate in the plane parallel to the groundplane, since we wish to minimize the effect of reflections that will occur if the waves are not parallel to the PEC groundplane. The amplitude for all the incoming waves is set to unity.

The phase I problem is solved subject to a 60% volume constraint. The radius of influence for the filter is set to $R_{\min} = 0.01$ m and the initial distribution is uniform with $\rho_{\text{init}} = 0.3$. The conducting material has $\sigma^m = 10^6$ S/m and the background material has $\epsilon_r = 1$.

The phase II problem is subject to the same volume constraint, but uses a stopping criteria related to the infinity norm of the design change, i.e. the optimization is stopped when $||\rho^k - \rho^{k-1}||_\infty < 1\%$. The filter is, however, applied using a continuation approach. The continuation scheme consists of starting the optimization with $R_{\min} = 0.02$ m. After 50 iterations, or if the optimization converges, the filter radius is reduced according to $R_{\min} = R_{\min}/2$. This is repeated until $R_{\min} < 10^{-3}$ m. At this point the filter radius is kept fixed while the conductivity is increased to $\sigma^m = 5.98 \cdot 10^7$ S/m, and the optimization is continued until the convergence criteria is met. The reason for using a seemingly complicated continuation approach for both the filter and the conductivity, is that numerical experiments have shown that it is hard for the optimizer to determine a

design which is resonant at the target frequency. When a continuation approach is not applied, the deviation between the resonant frequency of the optimized antenna and the target frequency is seen to be up to 10 %. Furthermore, the argument for starting with an increased filter radius compared to the one used in phase I, is to ensure that the phase I design used as starting point for the phase II problem, does not lead directly into a local minimum for the antenna optimization.

The discretized problem has $1.2 \cdot 10^6$ complex state dofs and a total of $7.2 \cdot 10^5$ design variables for the full volumetric problem and $1.7 \cdot 10^5$ for the shell problem. The mesh is partitioned into 88 parts and each design cycle takes approximately 2.5 minute.

5.4.1. The shell design problem

In this section the antenna optimization problem described in figure 4 is optimized for the case where only the outer shell, with a thickness of 4 mm, is used as design domain.

The phase I design after 30 iterations along with the convergence history is shown in figure 9(a),(b) and (c). In figure 9(d) the objective function values for each of the eight load cases are illustrated. From this figure it is seen that the energies of the individual load cases differ by a more than one order of magnitude. This is a consequence of the mean-value approach used for the phase I objective. From the plots of the optimized shell structure in figure 9(a) and (b), it is seen that a small disconnected region of conducting material is situated in front of the main structure that connects the device to the coaxial feed. This is similar to the optimized focusing device, c.f. figure 3, and the disconnected region is believed to act as a mirror for the incident waves which help to guide the waves into the coaxial cable. When analyzing the phase I design with respect to its radiation efficiency, it was found that the radiated power was 0.41 W out of 1 W supplied to the system. Thus, the optimized phase I design in figure 9 is already functional antenna. The optimized design should therefore be a good choice for initializing the actual antenna optimization.

The optimized phase II design is shown in figure 10(a) and (b). The stopping criteria is met after 366 iterations leading to an optimized design with a radiated power of 0.92 W at the target frequency. It is observed that the disconnected region of conducting material has been almost completely removed. The effect of the remaining disconnected region with respect to the antennas performance is considered to be negligible. Otherwise, the phase I and phase II optimized design share many overall similarities, including the shorting strip. In fact, the optimized design has a strong similarity to a planar inverted F-antenna (PIFA), i.e. a shorting strip is located close to the feed point which is connected to a larger top-plate. From the convergence history in 10(c), the effect of the continuation scheme for the filter radius and conductivity can be seen as the jumps in objective value. The increase in objective as the filter radius in decreased is to be expected since less intermediate design variables means less energy absorbtion and thus more possible energy to radiate. It is also observed, that the final stages of the continuation scheme, i.e. from iteration 200 and on, leads to small reductions in the objective function when the filter is reduced. The origin for the decrease in objective will be addressed later in the text.

From the frequency sweep in figure 10(d) it is seen that the actual resonance for optimized design situated at 305 MHz for which the radiated power is 0.96 W. This corresponds to 1.7 % deviation from the target frequency. Figure 10(d) also includes a frequency sweep of a post processed design for which all elements with $\rho > 0.5$ are set to 1 and all other to zero. For the binary design maximum amplitude is found to be 0.98

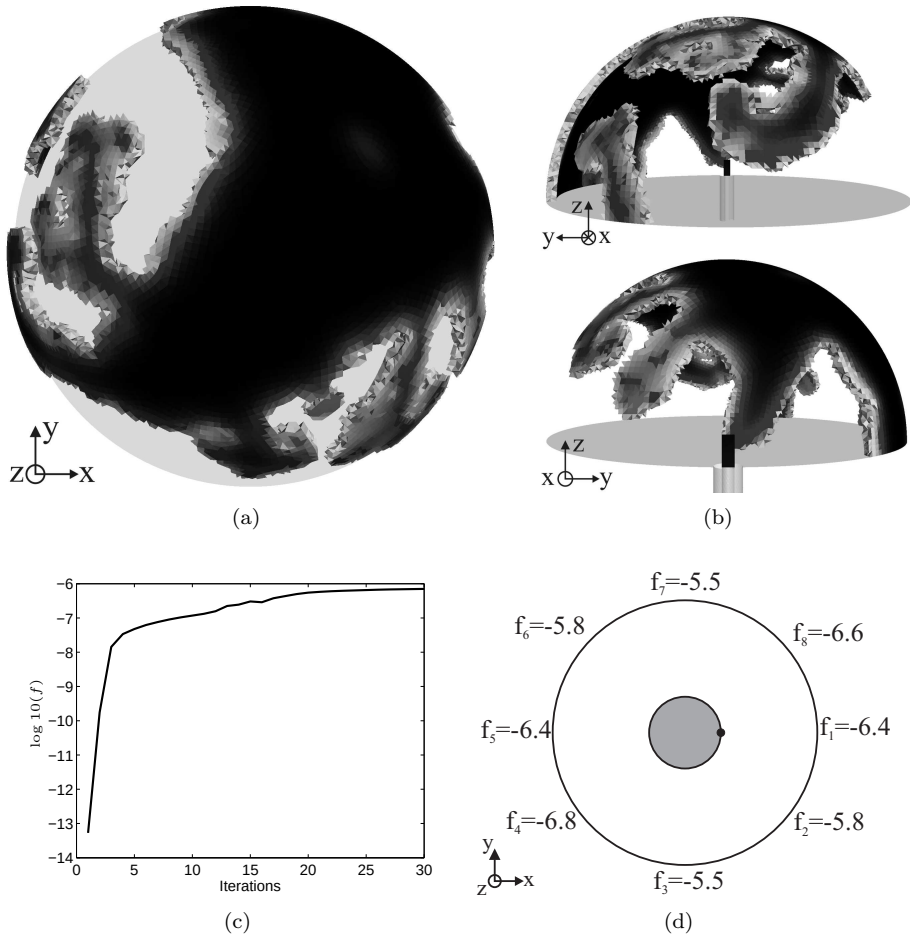

Figure 9: Phase I optimized design for the shell antenna design problem. (a) optimized design seen from the top, and (b) from the front and back. (c) convergence history and (d) the objective, i.e. equation (13), corresponding to each of the eight incident waves is shown.

W at 305.5 MHz. The observed shift in resonant frequency is believed to be a result of the design domain dimensions. That is, the size of the design domain is too small to contain an antenna resonant at 300 MHz. This assumption is confirmed by preliminary optimization results obtained using the same design configuration but optmized for 280 MHz and 330 MHz, respectively. This showed that the 280 MHz example has an approximately 10 % deviation from the target frequency, while the difference for the 330 MHz example is less than 0.5 %. Thus, even though the frequency shift can be reduced using a electrically larger design domain, it seems as if a small shift in resonance is unavoidable. A similar behavior is observed for the optimized matematerial designs in Diaz and Sigmund (2010).

A possible explanation for the difference in resonant frequency for the optimized and post processed design, as well as the small decreases in objective observed in the

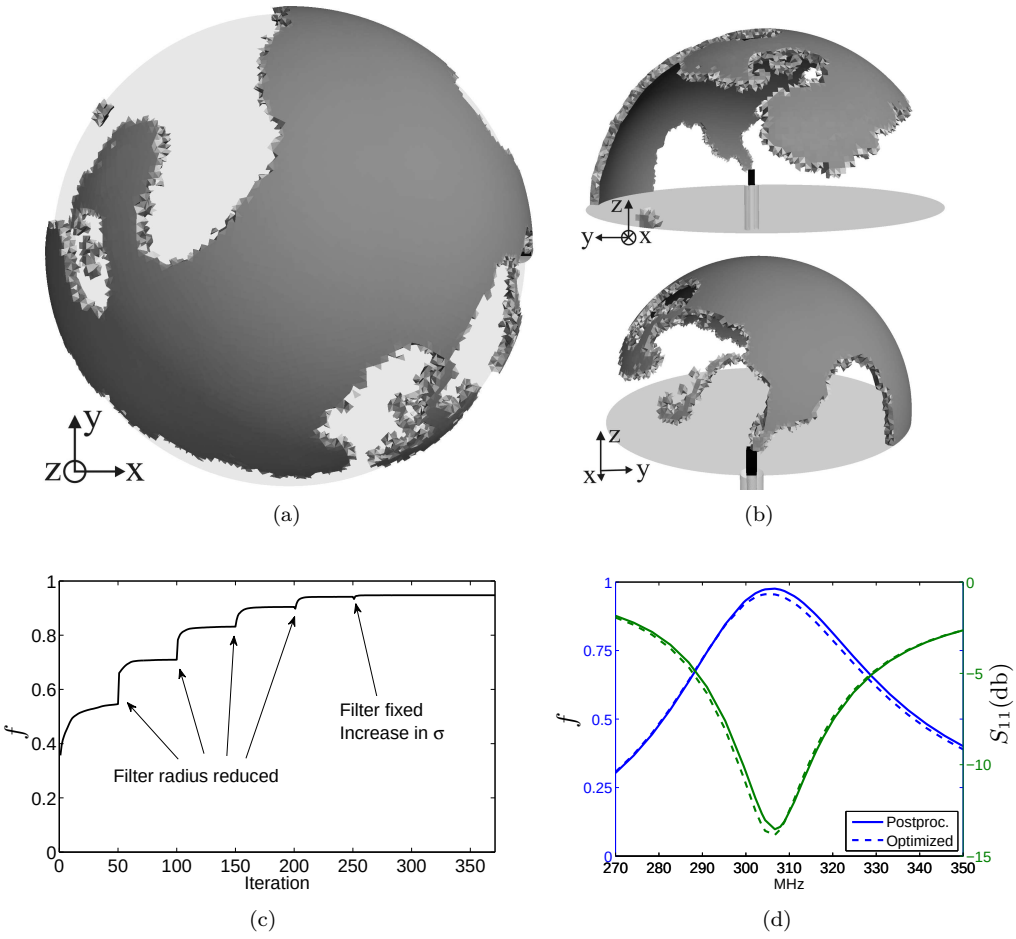

Figure 10: (a) and (b) threshold plots of the optimized design for the shell problem. The threshold is applied such that all $\rho > 0.5$ are displayed. (a) design seen from the top, and (b) from the front and back. (c) convergence history and (d) frequency sweeps of the radiated power and S_{11} parameter. The sweep is conducted using both the optimized design, included intermediate design elements, as well as a post processed design in which all $\rho > 0.5$ are set to 1 and all other to zero. From the frequency sweep it is seen that the radiated power is 0.96 W at 305 MHz and 0.975 W at 305.5 MHz for the optimized and post processed design, respectively.

convergence history, can be obtained using a mechanical analogy. For a mechanical oscillator, i.e. a mass/spring/damper system, the damped natural frequency is expressed as $\omega_d = \omega\sqrt{1-\zeta^2}$ where ζ is the damping coefficient and ω the undamped natural frequency. From this expression it is clear that large damping, i.e. intermediate design elements or low conductivity, will lead to a lower resonance. Thus, it is believed that the small reductions in objective function is due to an upward shift in resonant frequency. This assumption is confirmed by a frequency sweep of the optimized at iteration 50. This is shown in figure 11 from which it is seen that the resonance is located at 300.5 MHz with an objective of 0.57 W. From figure 11 it is also observed that the reflection

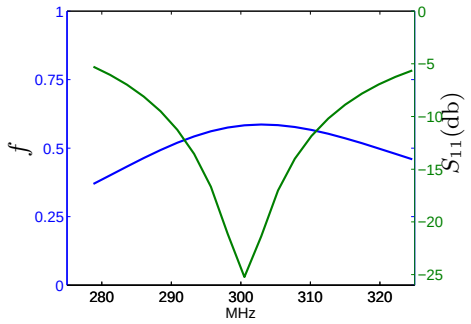

Figure 11: Frequency sweep of the antenna performance corresponding to the optimized design at iteration 50 in figure 10. It demonstrates that a large filter radius, i.e. high damping, makes it possible to have a resonance very close to the target frequency of 300 MHz.

coefficient is much smaller than for the final optimized design. This behavior is also linked to the damping nature of the intermediate design variables, i.e. more damping means more energy absorbtion and thus less energy to be reflected.

Compared to other high performing antennas, see e.g. (Balanis, 2005), it is noted that the reflection coefficient for the optimized design is quite large. Usually, the reflection will drop to -25 dB, or lower, at resonance. For the design problem presented here, this discrepancy is contributed to the length of the coaxial cable, i.e. $l = 0.12\ \lambda$, as well as its cross-sectional diameter. The large diameter and the fine mesh used allows for higher order modes to propagate in the cable, and the short length means that these higher order modes do not have time to be damped out before reaching the termination surface of the coaxial cable. Nonetheless, the fractional bandwidth at -10 dB is found to be reasonably good for both the optimized and post processed design. The post processed design displays a bandwidth of $FBW_{-10dB} = (314\text{MHz} - 298\text{MHz})/305\text{MHz} = 5.25\ \%$.

Finally, by comparison of the optimized antenna to the result presented in Erentok and Sigmund (2011), it is seen that the two design share many overall characteristics, i.e. the resemblance to the PIFA antenna. However, the optimized design presented here is obtained using a more elaborate interpolation scheme, which ensures that the energy is conserved and therefore that the level of post processing required to evaluate the antenna performance is reduced significantly.

5.4.2. The full design problem

The last numerical example extends the previous optimization problem by allowing material to be distributed throughout the hemispherical design domain.

The phase I optimized design and convergence history is visualized in figure 12 together with a plot showing the objective values for each of the eight load cases. The optimized design in figure 12(a-b) is seen to consist of two separated regions of conducting material of which only one is connected to the coaxial cable. It is also observed that the optimizer has utilized the extended freedom and has distributed material in the interior of the hemispherical design domain. However, the mean objective for this design problem is seen to be almost identical to that of the shell problem. This is believed to be a result of the filtering. For the shell problem the filter radius ensures that the

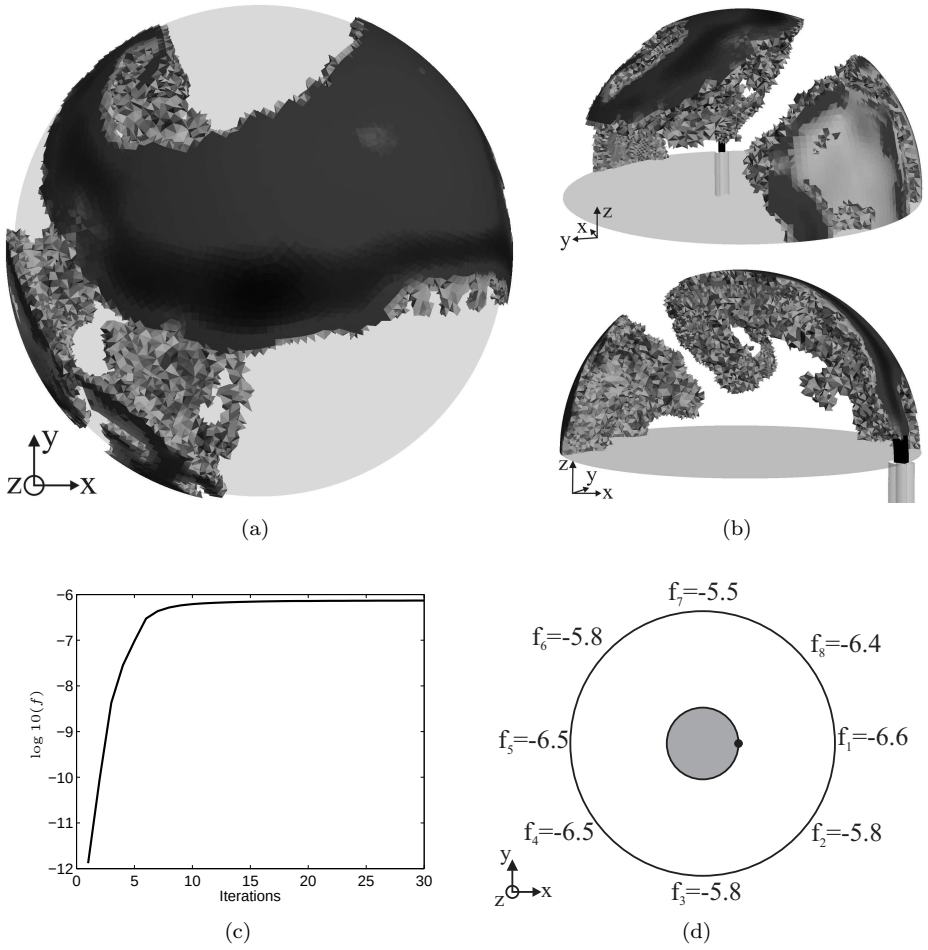

Figure 12: (a) and (b) phase I optimized design for the full antenna design problem. The optimized design is plotted using a threshold such that only elements with $\rho > 0.5$ are shown. (c) convergence history and (d) objective function values, equation (13), corresponding to each of the eight incident waves.

conducting regions are stretched from inner to outer surface of the shell domain, which results in a clearly defined interface between conductor and air. This is opposite to the design in figure 12(a-b), where only the outer surface provides a sharp interface. Thus, the energy absorption is much greater for the volumetric design problem, which explains why this design problem cannot outperform the shell problem. Analyzing the phase I design with respect to its antenna performance shows that the device only radiates 0.17 W.

The result of the phase II optimization is shown in figure 13. Inspection of the optimized design in figure 13(a) and (b), shows that the large disconnected region present in the phase I design has been completely removed by the optimizer. The amount of material in the interior of the design domain has also been significantly reduced. There

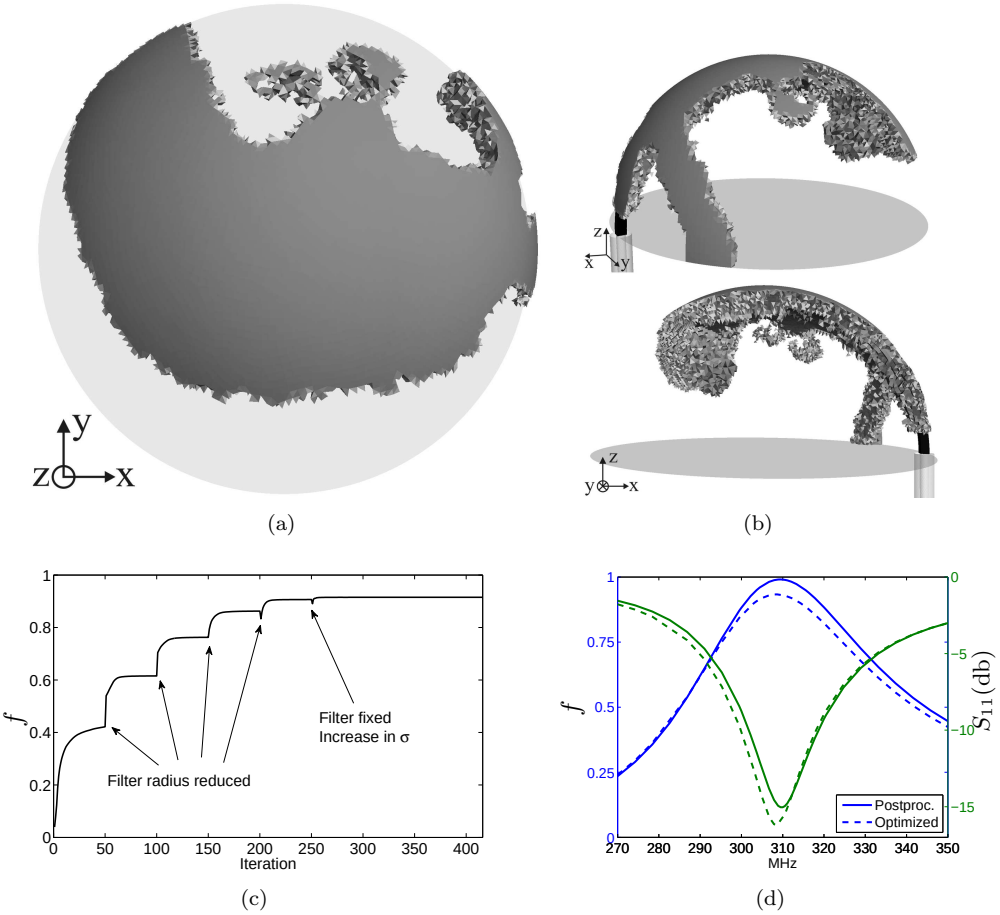

Figure 13: (a) and (b) phase II optimized design for the volumetric antenna design problem. The optimized design is visualized using a threshold such that all elements with $\rho > 0.5$ are shown. (c) convergence history and (d) frequency sweep of the antenna performance. For the optimized design the maximum radiated power is 0.93 W at 308 MHz, and for the post processed design the maximum power is approximately 0.99 W at 309 MHz.

is, however, still a large material concentration at the tip of the antenna, i.e. furthest away from the feed. The radiated power at the target frequency is found to be 0.84 W and the convergence history in figure 13(c) is seen to be similar to that of the shell problem, i.e. it contains jumps and dips in the objective function. The frequency sweep of the optimized design and a post processed design, for which all elements with $\rho > 0.5$ are set to 1 and all other to zero, can be seen in figure 13(d) From this plot it is seen that the optimized design yields a radiated power of 0.93 W at 308 MHz and 0.99 W at 309 MHz for the post processed design. This corresponds to a shift in resonant frequency of 2.7 % and 3 %, respectively. Just as expected, it is seen that the post processed design has the highest radiated power efficiency, which is due to larger amount of damping present in the optimized design. The fractional bandwidth of the post processed design is computed

to be $FBW_{-10dB} = (318\text{MHz} - 300\text{MHz})/309\text{MHz} = 5.83$ % and thus slightly better than for the shell problem.

It was expected that the extra freedom given to the optimizer, by including the entire hemisphere as design domain, would make it possible to reach an optimized design with a resonance closer to the target frequency. As seen this was not the case, and at the moment only two explanations seems possible. Firstly, it could be due to the optimized design having reached a local minimum. This is often the case in topology optimization and could be tested by rerunning the optimization using several different initial configurations (for the phase I problem). Secondly, it could be a result of the difference in surface representation for the two investigated problems. To investigate if this is the case, a new mesh should be generated for which neither of the two design domains have smooth surfaces.

6. Conclusion

In conclusion, we have shown a topology optimization procedure applicable for the design of 3D microwave and RF conductor-based electromagnetic structures. The design procedure was demonstrated on the design of a energy focusing device and a subwavelength antenna. To alleviate the initial design dependence for the antenna design problem, a two phase optimization scheme was proposed. The design of efficient subwavelength antennas was shown to be complicated by the small size of the design domain, which lead to an upward shift in resonant frequency. This was partially remedied by the application of continuation strategy for the filter and conductivity. The optimized antenna design was demonstrated to radiate in excess of 0.99 % of the supplied input power. The deviation with respect to target frequency was less than 3 % for both the considered test problems.

Future work should be directed towards expanding the optimization framework to include Pade approximations, such that the devices can be optimized for a range of frequencies at low numerical cost. The application of an eigenvalue solver could perhaps be used to further minimize the discrepancy between target and actual resonant frequency, i.e. min $|\omega - \omega^*|$. It could also be relevant to apply shape optimization to the topology optimized design, in order to investigate if further improvements are possible when the material interface are clearly defined. Finally, the optimization framework should be applied to new antenna and energy focusing design problems.

6.1. Acknowledgements

The authors acknowledge the support of the Danish Center for Scientific Computing, the Danish National Advanced Technology Foundation and the Elite Research Prize from the Danish Minister of Research

References

N. Aage and B. S. Lazarov. Parallel multiphyscics topology optimization using the method of moving asymptotes. *Submitted*, 2011.

N. Aage, N. A. Mortensen, and O. Sigmund. Topology optimization of metallic devices for microwave applications. *International Journal for Numerical Methods in Engineering*, 83:228–248, 2010.

E.E. Altshuler. Electrically small self-resonant wire antennas optimized using a genetic algorithm. *IEEE Transactions on Antennas and Propagation*, 50(3):297–300, 2002.

P. R. Amestoy, I. S. Duff, and J. Y. L'Excellent. Multifrontal parallel distributed symmetric and unsymmetric solvers. *Computer Methods in Applied Mechanics and Engineering*, 184(2-4):501–520, April 2000. ISSN 0045-7825.

C.A. Balanis. *Advanced Engineering Electromagnetics*. John Wiley & Sons Inc., 1st edition, 1989.

C.A. Balanis. *Antenna Theory: Analysis and Design*. Wiley-Interscience, 3rd edition, 2005.

Z. Bayraktar, P.L. Werner, and D.H. Werner. The design of miniature three-element stochastic yagi-uda arrays using particle swarm optimization. *IEEE Antennas and Wireless Propagation Letters*, 5(1): 22–26, 2006.

M. Bendse. Optimal shape design as a material distribution problem. *Structural Optimization*, 1: 193–202, 1989.

M.P. Bendsøe and O. Sigmund. *Topology Optimization; Theory, Methods and Applications*. Springer Verlag Berlin Heidelberg New York, 2nd edition, 2004.

S.R. Best. The radiation properties of electrically small folded spherical helix antennas. *IEEE Transactions on Antennas and Propagation*, 52(4):953 – 960, 2004.

Alejandro Diaz and Ole Sigmund. A topology optimization method for design of negative permeability metamaterials. *Structural and Multidisciplinary Optimization*, 41:163–177, 2010.

A. Erentok and O. Sigmund. Topology optimization of sub-wavelength antennas. *IEEE Transactions on Antennas and Propagation*, 59(1):58–69, 2011.

L. H. Frandsen, A. Harpoth, P. I. Borel, M. Kristensen, J. S. Jensen, and O. Sigmund. Broadband photonic crystal waveguide 60 degrees bend obtained utilizing topology optimization. *Optics Express*, 12(24):5916–5921, 2004.

W. Gropp, E. Lusk, and A. Skjellum. *Using MPI: Portable Parallel Programming with the Message-Passing Interface*. MIT Press, 1999.

A. Hoorfar. Evolutionary programming in electromagnetic optimization: A review. *IEEE Transactions on Antennas and Propagation*, 55(3):523–537, 2007. ISSN 0018-926X.

J. S. Jensen and O. Sigmund. Topology optimization of photonic crystal structures: a high-bandwidth low-loss t-junction waveguide. *Journal Of The Optical Society Of America B-Optical Physics*, 22(6): 1191–1198, June 2005.

J.S. Jensen and O. Sigmund. Topology optimization for nano-photonics. *Laser & Photon. Rev.*, 5(2): 308–321, 2011. ISSN 1863-8899.

J. Jin. *The Finite Element Method in Electromagnetics*. John Wiley & Sons, second edition, 2002.

George Karypis and Vipin Kumar. A fast and high quality multilevel scheme for partitioning irregular graphs. *SIAM Journal on Scientific Computing*, 20(1):359 – 392, 1999.

G. Kiziltas. *Dielectric material optimization of filters and antennas using SIMP*. PhD thesis, Dept. Mech. Eng. Univ. Michigan Ann Arbor, 2003.

G. Kiziltas, D. Psychoudakis, J. L. Volakis, and N. Kikuchi. Topology design optimization of dielectric substrates for bandwidth improvement of a patch antenna. *IEEE Transactions On Antennas And Propagation*, 51(10):2732–2743, 2003.

G. Kiziltas, N. Kikuchi, J. L. Volakis, and J. Halloran. Topology optimization of dielectric substrates for filters and antennas using simp. *Archives Of Computational Methods In Engineering*, 11(4):355–388, 2004.

B. S. Lazarov and O. Sigmund. Filters in topology optimization based on helmholtz-type differential equations. *Int. J. Numer. Meth. Engng.*, 2010. ISSN 1097-0207.

B. Luenberger and Y. Ye. *Linear and nonlinear programming*. Springer, 3rd edition, 2008.

Rene Matzen, Jakob S. Jensen, and Ole Sigmund. Topology optimization for transient response of photonic crystal structures. *J. Opt. Soc. Am. B*, 27:2040–2050, 2010.

R. Mittra. Challenges in antenna designs and some novel techniques for meeting them. In *Antennas and Propagation Conference, 2007. LAPC 2007. Loughborough*, pages 1–4, 2007.

Tsuyoshi Nomura, Kazuo Sato, Kenji Taguchi, Tatsuya Kashiwa, and Shinji Nishiwaki. Structural topology optimization for the design of broadband dielectric resonator antennas using the finite difference time domain technique. *Int. J. Numer. Meth. Engng.*, 71(11):1261–1296, 2007. ISSN 1097-0207.

J. Robinson and Y. Rahmat-Samii. Particle swarm optimization in electromagnetics. *IEEE Transactions on Antennas and Propagation*, 52(2):397–407, 2004. ISSN 0018-926X.

O. Sigmund and K. Hougaard. Geometric properties of optimal photonic crystals. *Physical Review Letters*, 100(15):1–4, 2008.

K. Svanberg. The method of moving asymptotes - a new method for structural optimization. *International Journal for Numerical Methods in Engineering*, 25, 1987.

Zaharias D. Zaharis. Boolean particle swarm optimization of 3-branch gsm/dcs/umts current dividers by using artificial immune system. *IEICE Electron. Express*, 5:41–47, 2008.

Shiwei Zhou, Wei Li, and Qing Li. Level-set based topology optimization for electromagnetic dipole antenna design. *Journal of Computational Physics*, 229(19):6915–6930, September 2010a. ISSN 0021-9991. URL `http://www.sciencedirect.com/science/article/B6WHY-506W6XD-2/2/ccd275a91c9c04a088a99b0807dfc4a5`.

Shiwei Zhou, Wei Li, Guangyong Sun, and Qing Li. A level-set procedure for the design of electromagnetic metamaterials. *Opt. Express*, 18:6693–6702, 2010b.

Y. Zhu and A. Cangellaris. *Multigrid Finite Element Methods for Electromagnetic Field Modeling*. John Wiley & Sons, first edition, 2006.

Publication [P4]

Topology optimization of devices for wireless energy transfer: The design parameterization

8th World Congress on Structural and Multidisciplinary Optimization
June 1-5, 2009, Lisbon, Portugal

Topology optimization of devices for wireless energy transfer The design parametrization

N. Aage, N.A. Mortensen, O. Sigmund

Technical University of Denmark, Solid Mechanics, Kgs. Lyngby, Denmark. Email: naa@mek.dtu.dk
Technical University of Denmark, Photonics Engineering, Kgs. Lyngby, Denmark. Email: namo@fotonik.dtu.dk
Technical University of Denmark, Solid Mechanics, Kgs. Lyngby, Denmark. Email: sigmund@mek.dtu.dk

1. Abstract
In electromagnetic optimization problems involving metallic microwave devices, such as resonators for wireless energy transfer, the volumetric distribution of good conductors, e.g. copper, have been known to cause numerical bottlenecks. In finite element analysis the limiting factor is the so-called skin depth, which calls for highly refined meshing to capture the physics. This has until now prohibited the application of topology optimization to such problems. In this paper we present a design parametrization that remedies this numerical bottleneck by interpolating between Maxwell's equations and an element impedance condition. The proposed design parametrization is confirmed by numerical examples.
2. Keywords: topology optimization, conductor design, finite elements, Maxwell's equations.

3. Introduction

The motivation for this work originates from the ever increasing usage of small handheld, or autonomous, electrical devices. Such devices, apart from their distinct functionality, share some general design issues. The devices used for communication relies heavily on an efficient antenna, confined within the geometric specifications of the device. A typical antenna is a metallic device connected to a transmission line [1]. However, common for all small electrical devices is that they consume energy. This ultimately means that the devices are no better than their power supplies allow them to be. The solution to the power problem took a new turn in 2007, where a MIT group lead by Prof. M.Soljacic demonstrated that one could obtain efficient mid-range wireless energy transfer (WiTricity) using magnetically resonant coupled copper coils [2]. The design of antennas and the design of transmitters/receivers for WiTricity, are therefore obvious candidates for the topology optimization method.

Topology optimization has proven to be a very successful design tool for general mechanical problems [3, 4]. Also in electromagnetic (EM) problems involving distribution of dielectric materials, e.g. dielectric antennas [7] and photonic crystals [5], the method has been applied with success. This work contributes with knowledge on how to obtain a numerically efficient topology optimization method for EM problems involving the distribution of a good conductor, such as copper, in the radio frequency (RF) range, i.e. 3 Hz to 300 GHz.

Previous work conducted on the subject is sparse due to the aforementioned numerical bottleneck, and the fact that until very recently, standard antenna designs and power supplies were adequate for almost all applications. However, in [8] the authors demonstrates the possibilities of applying gradient based topology optimization to the design of conformal electrically small antennas [1]. Though successful, the authors addresses the skin depth problem as a limiting factor, which should be remedied. Others, such as [9], have used generic algorithms (GA) for the volumetric distribution of copper in antenna design problems. Also here the authors obtain good designs, but are limited by the combinatoric approach used in GA.

3.1. Paper Outline

The remainder of this paper is organized as follows. First the governing equations and conductor modeling relevant for the development of the design parametrization is introduced. Next the finite element equations are discussed. The design parametrization is then introduced based on ideas from EM modeling in relation with the weak form. The proposed design parametrization is then confirmed by numerical examples. Finally the findings are summarized.

4. Physical & Numerical Model

In this section the governing equations necessary for the development of the design parametrization will

be introduced. This includes Maxwell's vector wave equation, the associated weak form along with the impedance condition.

4.1. Maxwell's Equations

Maxwell's equations for a linear, isotropic medium with no free charges, can be cast in the frequency domain assuming time-harmonic waves using the time convention $\boldsymbol{u}(\boldsymbol{x},t) = \mathbb{R}\left[\boldsymbol{u}(\boldsymbol{x})e^{j\omega t}\right]$, where ω is the frequency, j represents the imaginary unit and $\mathbb{R}(\cdot)$ is the real part [10]. By trivial manipulations, the set of first order partial differential equations (PDEs), can be recast as a single second order PDE in either the electric field, $\boldsymbol{E}$, or the magnetic field, $\boldsymbol{H}$. For the electric field it can be stated as

$$\nabla \times \left[\mu_r(\boldsymbol{r})^{-1}\nabla \times \boldsymbol{E}\right] - k_0^2\epsilon_c(\boldsymbol{r})\boldsymbol{E} \ = \boldsymbol{0} \tag{1}$$

where $\boldsymbol{r}$ is the position, $k_0 = \omega\sqrt{\epsilon_0\mu_0}$ is the free space wave number, ϵ_0 is the free space permittivity and μ_0 the free space permeability. The material specific parameters $\mu_r(\boldsymbol{r})$ and $\epsilon_c(\boldsymbol{r})$ are the relative permeability and relative complex permittivity respectively. The complex permittivity is given by

$$\epsilon_c(\boldsymbol{r}) = \epsilon_r(\boldsymbol{r}) - j\frac{\sigma(\boldsymbol{r})}{\omega\epsilon_0} \tag{2}$$

where $\epsilon_r(\boldsymbol{r})$ is the dielectric function and $\sigma(\boldsymbol{r})$ is the electric conductivity. With respect to the topology optimization problem, the position dependent material parameters, $\mu_r(\boldsymbol{r})$, $\epsilon_r(\boldsymbol{r})$ and $\sigma(\boldsymbol{r})$ are the unknown functions to be determined.

4.2. Impedance Condition

Before presenting the weak form, or finite element form, of the vector wave equation the notion of skin depth is introduced. In EM wave propagation the skin depth, δ, is a measure for the distance through which the amplitude of a traveling plane wave decreases by a factor e^{-1} in a conductor [1]. An approximation can be obtained through the following formula

$$\delta = \frac{1}{\sqrt{\pi\sigma\mu\omega}} \tag{3}$$

The skin depth is important since most microwave devices have sizes in the order of mm, while the skin depth typically is in the μm range, i.e. three orders of magnitude smaller. To put skin depth into the context of finite elements and topology optimization, let us consider an example in which we wish to use a small cube of $2 \times 2 \times 2$cm for design domain. The target frequency is set to 300 MHz and the conductor is chosen to be copper with $\sigma = 5.998 \cdot 10^7$S/m. In that case the skin depth becomes $\delta = 3.8 \cdot 10^{-6}$m. For topology optimization each element in the mesh is possibly metallic, and thus the whole domain must be meshed such that the skin depth can be resolved. Using simple first order finite elements one should have at least two elements per skin depth to capture the rapid decay. This leads to approximately 10.000 elements in each spatial direction, i.e. a total of 10^{12} elements in 3D. Such numbers of elements implies that direct interpolation, as done in most other topology optimization problems [4], is insufficient for the microwave problem.

Due to the skin depth issue most numerical modeling of metallic devices utilizes boundary conditions to represent the conducting regions. For perfect electric conductors (PEC), i.e. $\sigma = \infty$, the skin depth is zero, and the metal can be modeled by a homogenous Dirichlet condition for the electric field and a homogenous Neumann condition for the magnetic field. For finite conductivity an approximate relation between the electric and magnetic fields can be used, which can be stated as a mixed boundary condition on the same form for both fields [11]. Below the approximate condition is stated for the electric field

$$\boldsymbol{n} \times \left([\mu_r^d]^{-1}\nabla \times \boldsymbol{E}\right) + jk_0\sqrt{\frac{\epsilon_c^m}{\mu_r^m}}\boldsymbol{n} \times (\boldsymbol{n} \times \boldsymbol{E}) = \boldsymbol{0} \tag{4}$$

where $\boldsymbol{n}$ is normal vector pointing into the conductive region, $(\cdot)^d$ and $(\cdot)^m$ refer to the dielectric and the metal respectively. Note that an equivalent formulation can be derived for the magnetic field form of Maxwell's equations. The condition in Eq.(4) is called an impedance conditions, and it forms the backbone for the material interpolation scheme to be presented in the upcoming chapter.

4.3. Weak Formulation

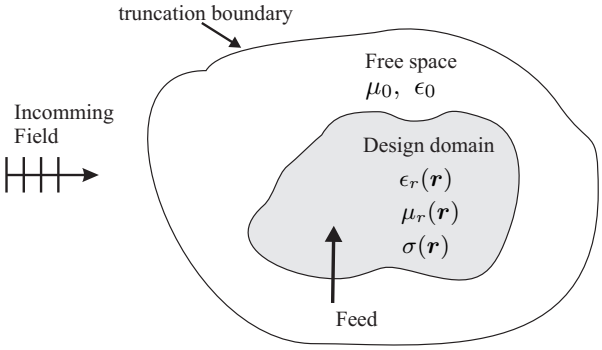

Figure 1: Illustration of a general EM topology optimization problem which can be used for the design of microwave antennas, magnetic resonators, etc.

In this section the numerical solution to Maxwell's vector wave equation is addressed. Numerical methods, such as integral methods, finite elements and finite differences, could all be used for the Maxwell problem, but due to geometric freedom and sparsity of system matrices the finite element method is preferred and used in the work presented here.

The finite element formulation, or weak form, can for obvious reasons not determine the solution to Maxwell's equations in infinite space. Therefore the domain of interest is truncated and some approximation to the Sommerfeld radiation condition [10] is applied at this boundary. The most frequently used numerical techniques for truncation includes absorbing boundary conditions (ABC), perfectly matched layers (PML) and finite element boundary integral (FE-BI) methods [11]. A general sketch of an analysis problem including optimization can be seen in figure 1. Let Ω be the total computational domain, and Γ the truncation boundary. For e.g. the electric field the problem becomes to find $\boldsymbol{W} \in H_0(\text{curl}, \Omega)$

$$\begin{aligned} \int_\Omega \left[(\nabla \times \boldsymbol{W}) \cdot \mu_r^{-1} \cdot (\nabla \times \boldsymbol{E}) - k_0^2 \boldsymbol{W} \cdot \epsilon_c \cdot \boldsymbol{E} \right] \mathrm{d}\Omega \\ - \int_\Gamma \boldsymbol{W} \cdot \left[\boldsymbol{n} \times \left(\mu_r^{-1} \cdot \nabla \times \boldsymbol{E} \right) \right] \mathrm{d}\Gamma = 0 \\ \forall \boldsymbol{E} \in H(\text{curl}, \Omega) \end{aligned} \tag{5}$$

where $\boldsymbol{W}$ is a vector test function. For more details on the vector, or edge, based finite elements associated with the function space $H(\text{curl}, \Omega)$ the reader is referred to e.g. [11, 12]. The surface integral in Eq. (5) means that the discrete form, or FE equations, depends on the specific boundary condition applied on Γ. Therefore, and not to loose generality, the discrete form will not be specified until the presentation of a numerical example.

5. Design Parametrization

The design parametrization presented next follows the standard topology optimization approach in which each element in the finite element mesh is associated with a continuous design variable, or density, $0 \leq \rho^e \leq 1$. The design variable is used to interpolate between candidate materials which in this setting is a conductor, $(\cdot)^m$, and a dielectric $(\cdot)^d$. Intermediate values of the design variables are unwanted since these are difficult to interpret physically and thus makes the optimized designs hard to fabricate. Therefore the interpolation functions must be chosen such that regions of intermediate densities are minimized.

5.1. Design Dependence in Maxwell's Equations

In order to circumvent the limitations induced by the skin depth problem, the design parametrization is based on a mixture of Maxwell's equations and an element impedance condition. This is to be understood as if each element of conducting material is replaced by an impedance condition. For a single design element this can be stated generally without specifying the interpolation functions as

$$\begin{aligned} &\nabla \times (\tilde{A} \nabla \times \boldsymbol{u}) - k_0^2 \tilde{B} \boldsymbol{u} = 0, && \text{in } \Omega^e \\ &\boldsymbol{n} \times (A \nabla \times \boldsymbol{u}) - f(\rho^e) j k_0 \sqrt{AB} \boldsymbol{n} \times (\boldsymbol{n} \times \boldsymbol{u}) = 0, && \text{on } \Gamma^e \end{aligned} \tag{6}$$

Table 1: Field dependent parameters for the design parametrization used for conductor/dielectric based topology optimization, Eqs.(6). The superscripts $(\cdot)^d$ refer to the dielectric and $(\cdot)^m$ to the metal. The functions $\mu_r(\rho^e)$, $\epsilon_r(\rho^e)$ and $\sigma(\rho^e)$ is given in Eq. (7).

$\boldsymbol{u}$	A	B	$\tilde{A}$	$\tilde{B}$
$\boldsymbol{E}$	$(\mu_r^m)^{-1}$	$\epsilon_r^m - j\frac{\sigma^m}{\omega\epsilon_0}$	$\mu_r(\rho^e)^{-1}$	$\epsilon_r(\rho^e) - j\frac{\sigma(\rho^e)}{\omega\epsilon_0}$
$\boldsymbol{H}$	$\left(\epsilon_r^m - j\frac{\sigma^m}{\omega\epsilon_0}\right)^{-1}$	μ_r^m	$\left(\epsilon_r(\rho^e) - j\frac{\sigma(\rho^e)}{\omega\epsilon_0}\right)^{-1}$	$\mu_r(\rho^e)$

where Ω^e and Γ^e refer to the element volume and boundary respectively, and $\boldsymbol{n}$ is an outward normal for element e. The dependent field $\boldsymbol{u}$ and its associated parameters A, B, $\tilde{A}$, $\tilde{B}$ are given in table 1. Note that the sign in the impedance condition has changed, since the normal now points into the element. The function $f(\rho^e)$ is included to control the presence of the element impedance condition. When $f(\rho^e) = 0$ only the first term of the element boundary condition in Eq. (6) remains and is equated to zero. With respect to the weak form this means that the boundary integral in Eq. (5) disappears and therefore that the standard wave equation is obtained. For $f(\rho^e) = 1$ the impedance condition is present and the wave equation is suppressed, hence the skin depth is resolved.

Note that this approach does not allow for direct interpolation of the conductivity in the element impedance condition, since for $\sigma = 0$ we have that $\epsilon_c = \epsilon_r$ which means that the element boundary condition does not vanish for $\rho^e = 0$. Also the physical interpretation of intermediate densities is uncertain, though one might be able to link them to materials with varying conductivities. However, if the final design has $\rho = 0$ or $\rho = 1$ in all design elements, the physical performance of the optimized design has been analyzed with a correct physical model. Thus, if the design parametrization is devised such that the final design is black and white, there is no problem in allowing the optimizer to pass through intermediate densities during the iterative optimization process. This is a commonly used trick in topology optimization [4] and will also be used in the work presented here.

5.1. Interpolation Functions

The last step is to determine the interpolation functions identified in Eq.(6) and Table 1. The functions should be chosen such that the following requirements are met best possibly. The interpolation functions must be valid for both the electric and magnetic field formulation of Maxwell's equations. Furthermore, the functions have to be monotonically varying and have the property that a small change in ρ^e should lead to a small change in system response. Finally the interpolation functions should, if possible, result in designs free from intermediate values of ρ^e. In some topology optimization problems a penalization parameter is required to obtain black and white designs, as done in e.g. in the Solid Isotropic Material with Penalization (SIMP) scheme, where the stiffness is penalized to make intermediate densities uneconomical [13, 4] for the optimizer. However, as will be explained in the following section the EM optimization problem does not require any type of penalization to ensure black and white designs.

The functions presented below are determined based on numerical studies.

$$\begin{aligned} &\mu_r(\rho^e) = \mu_r^d + \rho^e(\mu_r^m - \mu_r^d) && \sigma(\rho) = 10^{\left(\log_{10}(\sigma^d) + \rho^e[\log_{10}(\sigma^m) - \log_{10}(\sigma^d)]\right)} \\ &\epsilon_r(\rho^e) = \epsilon_r^d + \rho^e(\epsilon_r^m - \epsilon_r^d) && f(\rho^e) = \rho_e^{p_{BC}} \\ &p_{BC} \approx 13 \text{ for } \boldsymbol{E} && p_{BC} \approx 1 \text{ for } \boldsymbol{H} \end{aligned} \tag{7}$$

The linear interpolation of the permittivity and permeability is successfully adopted from e.g. [5], while the interpolation function $f(\rho^e)$ and $\sigma(\rho^e)$ needs special attention. Interpolation of the conductivity is made difficult due to the following two reasons. Firstly, the numerical range is huge, i.e. $\sigma = 0$ for free space and $\sigma = 10^7 S/m$ for a typical good conductor [10]. Secondly, the conductivity is a damping parameter for the EM fields. This means that even numerically small conductivities can lead to large changes in field response, and furthermore that conductivities above a certain threshold limit will only have a small influence on the response. Due to these issues it was found that the interpolation of σ was best performed in the logarithmic scale, and then converted back to the physical scale using a power function [14]. Finally note that σ^d must always be larger than zero, even for lossless dielectrics due to the logarithmic interpolation. For lossless dielectrics we suggest to use $\sigma^d = 10^{-4}$ based on the numerical experiments.

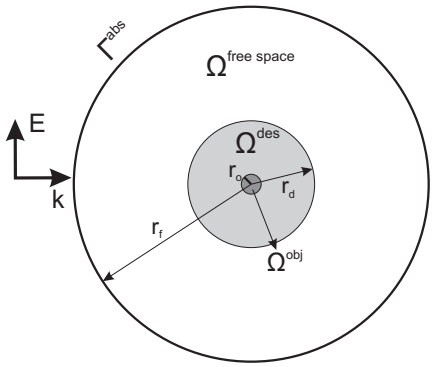

Figure 2: Sketch of the design problem for TE polarized waves. The measures are $r_d = 1.0m$, $r_o = 0.15m$ and $r_f = 2.5m$. The target frequency is 300MHz and the materials are a good conductor e.g. copper and air.

The interpolation function $f(\rho)$ for the element impedance condition must take the difference in field formulation into account. For the electric field the impedance condition is proportional to ϵ_c, while it is proportional to the inverse, i.e. ϵ_c^{-1}, for the magnetic field. From numerical experiments it was found that $f(\rho)$ for the electric field should be similar to a logarithmic function, while $f(\rho)$ should be close to linear for the magnetic field. Since we wish to use the same function for both field formulations, a polynomial with varying exponent is a simple choice, i.e. $f(\rho) = \rho^{p_{BC}}$. The exponent p_{BC}, which should not be seen as a penalization parameter c.f. the SIMP scheme [13], yields good results when using $p_{BC} \approx 1$ for the magnetic field and $p_{BC} \approx 13$ for the electric field. The reason why a penalization parameter is not needed for the EM problem is due to damping nature of the conducting material. By this is meant that regions of intermediate conductivities slowly damps, or absorbs, the energy from the EM fields, while a high conductivity means fast damping and thus that less energy is dissipated.

As already stated one can think of the design of electrically conducting devices as the distribution of highly damping material. Due to numerical precision this means that σ^m larger than some value, σ^m_{cutoff}, does not change the system response much. With respect to the optimization a numerically large σ^m will then lead to designs with intermediate design variables, since the optimizer won't benefit from letting $\sigma(\rho) \to \sigma^m$. Therefore a study to determine the threshold values of σ^m has been conducted. For the electric field the limit was found to coincide with the conductivity of copper, i.e. $\sigma^m_{E_{cuttoff}} \approx 10^7 S/m$, while for the magnetic field it was lower, i.e. $\sigma^m_{H_{cuttoff}} \approx 10^6 S/m$. Hence, the design parametrization should not be used to distinguish between good conductors such as copper and silver, but should merely be used to model a good conductor.

6. Optimization Problem

In this chapter the optimization problem is to be introduced along with its numerical solution. The problem to be considered is the design of a 2D magnetic resonator. This can be seen as a highly simplified model for designing a device for energy harvesting from an incoming EM field. The objective is to maximize the magnetic energy, $\Phi(\rho, \boldsymbol{H}) = \int_{\Omega^{obj}} \mu |\boldsymbol{H}|^2 \mathrm{d}\Omega$, in an a priori specified part of the modeling domain, Ω^{obj}, for a target frequency of 300MHz. The design problem is illustrated in figure 2. The model problem assumes transverse electric (TE) polarization, that is

$$\begin{aligned} \boldsymbol{H} &= H_z(x,y)\boldsymbol{e}_z \\ \boldsymbol{E} &= E_x(x,y)\boldsymbol{e}_x + E_y(x,y)\boldsymbol{e}_y \end{aligned} \tag{8}$$

which leads to either the scalar Helmholtz equation for the H_z field, or a vector curl-curl equation for the electric field in the plane. To demonstrate that the design parametrization works equally well for both the electric and magnetic formulation, the design problem is solved using both formulations, i.e. nodal elements for H_z and edge elements for E_x and E_y [11]. The modeling domain is truncated with a first order absorbing boundary condition (ABC) located 1.5λ from the design domain. The complete discrete formulation can now be stated as

$$(\boldsymbol{S}(\rho) + \boldsymbol{A})\,\boldsymbol{u} = \boldsymbol{f} \tag{9}$$

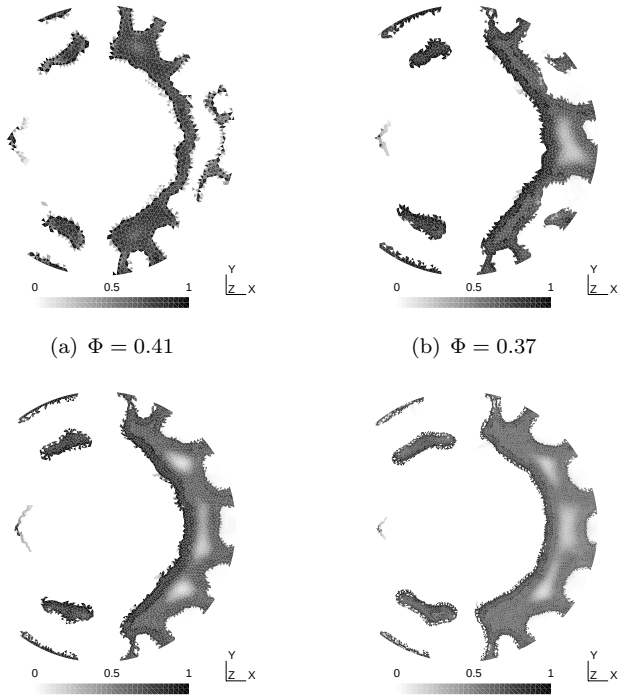

(a) $\Phi = 0.41$ (b) $\Phi = 0.37$

(c) $\Phi = 0.45$ (d) $\Phi = 0.63$

Figure 3: Optimized designs for the problem in figure 2 for three different mesh resolutions with fixed density filter. The number of design elements are (a) 15950 edge elements, (b) 15950 nodal elements, (c) 25292 nodal elements and (d) 41560 nodal elements. Convergence was reached in 120 to 350 iterations.

where $\boldsymbol{S}(\rho)$ refers to the design element contributions, $\boldsymbol{A}$ contains free space, fixed domains and domain truncation contributions and $\boldsymbol{f}$ contains the system load. The system matrix for the design elements can be computed for the electric field formulation as

$$\begin{aligned}
\boldsymbol{S}(\rho) &= \sum_{e=1}^{N} \Big(\boldsymbol{K}^e(\tilde{A}) - \boldsymbol{M}^e(\tilde{B}) - \boldsymbol{B}^e(f(\rho), A, B) \Big) \\
\boldsymbol{K}^e(\tilde{B}) &= \textstyle\int_{\Omega^e} (\nabla \times \boldsymbol{N}) \cdot \tilde{A} \cdot (\nabla \times \boldsymbol{N}) \mathrm{d}\Omega \\
\boldsymbol{M}^e(\tilde{A}) &= \textstyle\int_{\Omega^e} k_0^2 \boldsymbol{N} \cdot \tilde{B} \cdot \boldsymbol{N} \mathrm{d}\Omega \\
\boldsymbol{B}^e(f(\rho), A, B) &= f(\rho^e) j k_0 \textstyle\int_{\Gamma^e} (\boldsymbol{n} \times \boldsymbol{N}) \cdot \sqrt{AB} \cdot (\boldsymbol{n} \times \boldsymbol{N}) \mathrm{d}\Gamma
\end{aligned} \tag{10}$$

where $\boldsymbol{N}$ denotes the shape function. The contributions due to the ABC, free space and incident wave can be computed as described in e.g. [15]. Using the shape functions the objective function can be evaluated by

$$\Phi(\boldsymbol{H}, \rho) = \bar{\boldsymbol{H}}^T \boldsymbol{Q} \boldsymbol{H}, \quad \text{with } \boldsymbol{Q} = \sum_{e=1}^{N_{obj}} \mu_e \boldsymbol{N}_e^T \boldsymbol{N}_e \tag{11}$$

where the overbar denotes complex conjugate and N_{obj} are the number of elements in Ω^{obj}. The optimization problem can be stated on standard form as

$$\begin{aligned}
\max_{\rho \in \mathbb{R}^N} \quad & \log_{10}(\bar{\boldsymbol{H}}^T \boldsymbol{Q} \boldsymbol{H}) \\
\text{s.t.,} \quad & (\boldsymbol{S}(\rho) + \boldsymbol{A})\, \boldsymbol{u} = \boldsymbol{f} \\
& \tfrac{\sum_e^N \rho_e V_e}{V f^*} - 1 < 0 \\
& 0 \leq \rho^e \leq 1, \quad e = 1, N
\end{aligned} \tag{12}$$

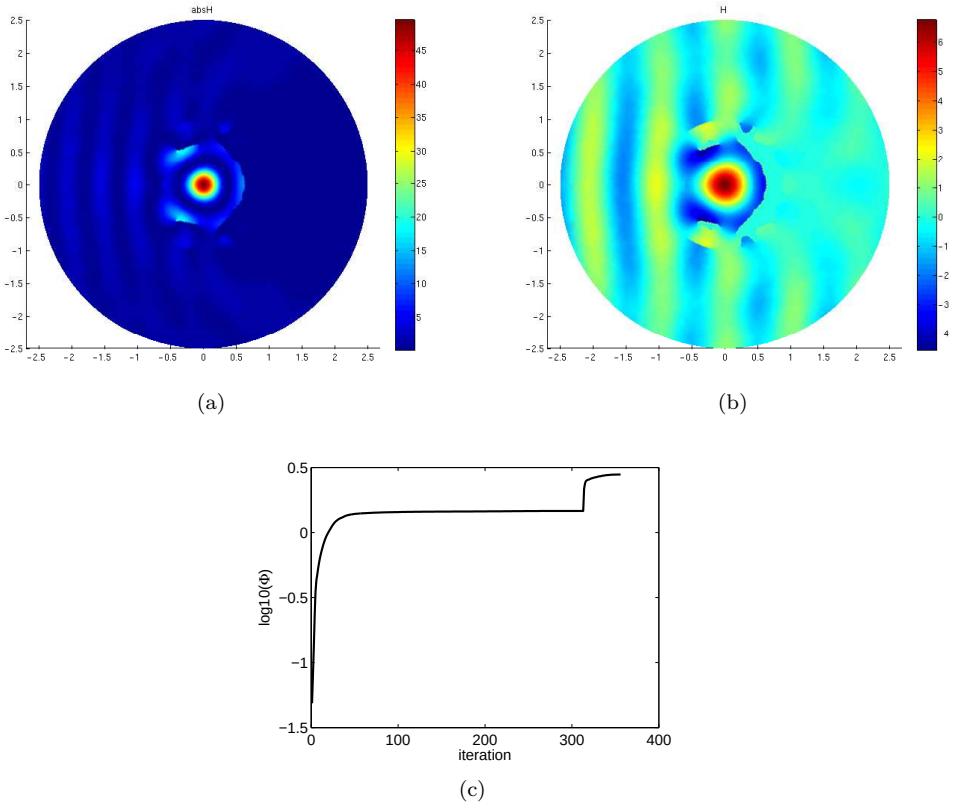

(a) (b) (c)

Figure 4: Plot of the magnetic energy (a), the magnetic field (b) and convergence history (c) associated with the optimized design in figure 3 (c).

where the second constraint is a restriction on the available material used to limit the amount of conductor used for the design problem. The logarithm for the objective is included for proper numerical scaling and the density filter, see [16, 17, 18], is applied to introduce a minimum length scale to the design problem. Since the density filter introduces a region of undesirable intermediate design variables, it is applied in conjunction with a continuation scheme such that the filter radius, $R_{\min}$, gradually approaches zero as the optimization process progresses. The optimization problem is implemented in Matlab using triangular nodal and edge based finite elements. The optimization problem is solved using gradient based optimization algorithm the method of moving asymptotes (MMA) courtesy of K.Svanberg [19]. The sensitivities are obtained using the adjoint method, see [5] for details.

6.1. Optimized Designs

The optimization problem is solved using $\sigma^m = 10^6 S/m$ and $\sigma^d = 10^{-4} S/m$ as candidate materials, i.e. a good conductor in free space. The allowed volume fraction is set to 50% of the design domain and the move limit for MMA is set to 0.3. The initial design is a uniform distribution of material in the design domain with $\rho_{init} = 0.1$ unless else is stated. The optimized designs shown in figure 3 are obtained using a two step continuation approach for the density filer. First the radius is set to $0.08m$ and upon convergence it is changed to zero and the optimization is continued. The optimized designs in figure 3(a) and (b) are obtained using the same discretization but different formulations of the Maxwell problem. In figure 3(a) the problem is solved for the electric field using edge finite elements, while the problem in figure 3(b) is solved with nodal elements for the scalar magnetic field. The designs are seen to be quantitatively the same with equivalent objectives, though the area to the right of the parabola have different layouts. For the refined meshes the designs are still qualitatively equivalent to the ones determined on the coarse mesh, but with improved objectives. The difference in objective is most likely due to extra freedom associated with the higher number of design variables for the refined meshes. It should be noted that since the incident field propagates from left to right, the influence of the structure behind the parabola is minimal to the performance of the design. A plot of the magnetic field and energy associated with the optimized design in figure 3(c) is shown in figure 4 along with the iteration history.

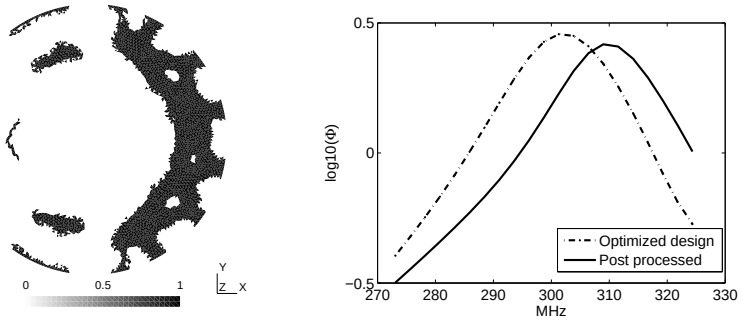

(a) (b)

Figure 5: Post processing results based on the optimized design of figure 3 (b). The cut off is chosen as $\rho^e > 0.3 \rightarrow 1$ and zero for all other elements. The frequency sweep of the post processed design displays a maximum at 308 MHz with $\Phi = 0.42$, while the optimized design has maximum at 301 MHZ with $\Phi = 0.45$.

From the plot of the magnetic energy, c.f. figure 4(a), it is clear that the energy on the left side of the parabola is close to zero due to shielding effect of the conductor. From the convergence plot in figure 4(c) it is noticed that the convergence is monotone and smooth.

To validate the optimized designs and their performance, the optimized design in figure 3(c) is rendered fully 0-1 by setting all $\rho^e > 0.3$ to one and all others to zero. The now well defined interface between conductor and free space is then modeled by a PEC condition and analyzed by a frequency sweep. The post processed design and plot of the frequency sweep can be seen in figure 5. Here it is noticed that the magnetic energy has a maximum of $\Phi = 0.42$ at 308MHz, while the optimized design shows a maximum at 301MHz of $\Phi = 0.45$. Both objectives are slightly better than the one predicted at 300MHz by the optimized design, but it is especially interesting to see that the target frequency is shifted by 2.7% for the post processed design. This shift in frequency is most likely due to the intermediate design variables in the optimized design. By this is meant that the optimizer can utilize the grey elements to tune the performance of the optimized design to the specified target frequency. When the intermediate design variables are removed during post processing, it then leads to a shift in target frequency and to a small change in objective value. Thus, to circumvent this issue a better filter and/or a combined approach in which the topology optimization is followed by shape optimization should be applied.

7. Conclusion

In this paper we have developed a novel design parametrization, based on the interpolation between Maxwell's wave equation and an element impedance condition, which allows for numerically efficient topology optimization of EM metallic microwave devices.

The design parametrization is shown to yield field independent designs meaning that equivalent designs are obtained with the electric and magnetic field formulations of Maxwell's equations. However, due to the numerically large values of a good conductor it was found that the method cannot be used for distributing specific conductors, e.g. silver or copper, but should merely to be used for modeling conductor and no conductor. good conductor designs. The validity of the optimized design was confirmed by the post evaluation in which the optimized design is rendered completely black and white. The now well-defined interface between conductor and dielectric was then modeled by a PEC condition. This analysis showed good agreement with the optimization results, though a shift in peak frequency was observed. The shift is contributed to presence of intermediate design elements in the optimized design. This means that either a better filtering technique should be applied, or the topology optimization should be followed by a few iterations of a shape optimization scheme.

A more elaborate paper on this work, including several other examples, has been submitted as a journal article.

7.1 Acknowledgements

This work is supported by the Danish National Advanced Technology Foundation through the grant *Wireless Coupling in Small Autonomous Apparatus* (`www.hoejteknologifonden.dk`), by the Eurohorcs/ESF European Young Investigator Award (EURYI, `www.esf.org/euryi`) through the grant *Synthesis and*

topology optimization of optomechanical systems, and by the Danish Center for Scientific Computing (`www.dcsc.dk`). The authors would finally like to extend their gratitude to the partners at the Danish Institute of Technology and the research groups TopOpt and TopAnt at the Technical University of Denmark for many useful and enlightening discussions.

8. References

[**1**] Balanis C.A. *Antenna Theory: Analysis and Design* (3rd edn) John Wiley & Sons., 2005

[**2**] Kurs A., Karalis A., Moffatt R., Joannopoulos J.D., Fisher P. and Soljacic M. Wireless power transfer via strongly coupled magnetic resonators. *Science* 2007; **317**

[**3**] Bendsøe M. P. and Kikuchi N., Generating optimal topologies in structural design using a homogenization method, *Comput. Methods Appl. Mech. Eng.* 1988, **71**:197-224

[**4**] M.P. Bendsøe and O. Sigmund, *Topology Optimization: Theory, Methods and Applications*, Springer-Verlag, Berlin, 2003.

[**5**] J. Jensen and O. Sigmund, Topology optimization of photonic crystal structures: a high-bandwidth low-loss T-junction waveguide, *Journal of the Optical Society of America* 2005, **22**(6)

[**6**] Borel P. I., Harpth A., Frandsen L. H., Kristensen M., Shi P., Jensen J. S., and Sigmund O., Topology optimization and fabrication of photonic crystal structures, *Optical Express* 2004, **12**:1996-2001.

[**7**] Kiziltas G., Kikuchi N., Volakis J.L. and Halloran J., Topology optimization of dielectric substrates for filters and antennas using SIMP, *Archives Of Computational Methods In Engineering* 2004, **11**(4):355–388

[**8**] Erentok A. and Sigmund O., Topology optimized efficient sub-wavelength antennas with large bandwidth, SUBMITTED

[**9**] Koulouridis S., Psychoudakis D. and Volakis J.L., Multiobjective Optimal Antenna Design Based on Volumetric Material Optimization, *IEEE Transactions on antennas and propagation* 2003, **55**(3):594–603

[**10**] Balanis C.A. *Advanced Engineering Electromagnetics* (1st edn) John Wiley & Sons Inc., 1989

[**11**] Jin J. *The Finite Element Method in Electromagnetics* (2nd edn) John Wiley & Sons., 2002

[**12**] Zhu Y. and Cangellaris A. *Multigrid Finite Element Methods for Electromagnetic Field Modeling* (1st edn) John Wiley & Sons., 2006

[**13**] Bendsøe, M. P., Optimal shape design as a material distribution problem, *Structural Optimization* 1989, **1**:193–202.

[**14**] Diaz A. R. and Sigmund O., Negative permeability metamaterial design by topology optimization, SUBMITTED

[**15**] Jin J. and Riley D.J. *The Finite Element Analysis of Antennas and Arrays* (1st edn) John Wiley & Sons., 2008

[**16**] Bourdin B., Filters in topology optimization. *International Journal for Numerical Methods in Engineering* 2001, **50**(9):2143-2158

[**17**] Bruns T.E. and Tortorelli D.A., Topology optimization of nonlinear elastic structures and compliant mechanisms. *Computater Methods in Applied Mechanics and Engineering* 2001, *190*(26-27):34433459

[**18**] Sigmund O., Morphology-based black and white filters for topology optimization, *Structural and Multidisciplinary Optimization* 2007, **33**:401–424

[**19**] Svanberg K., The method of moving asymptotes - a new method for structural optimization, *International Journal for Numerical Methods in Engineering* 1987, **25**

DTU Mechanical Engineering
Section of Solid Mechanics
Technical University of Denmark

Nils Koppels Allé, Bld. 404
DK- 2800 Kgs. Lyngby
Denmark
Phone (+45) 45 25 42 50
Fax (+45) 45 93 14 75
www.mek.dtu.dk
ISBN: 978-87-90416-56-0

DCAMM
Danish Center for Applied Mathematics and Mechanics

Nils Koppels Allé, Bld. 404
DK-2800 Kgs. Lyngby
Denmark
Phone (+45) 4525 4250
Fax (+45) 4593 1475
www.dcamm.dk
ISSN: 0903-1685